WATER TRANSPORT IN PROTON EXCHANGE MEMBRANES

by

Tatiana Romero Castañón

Ing. Química, Universidad Popular Autónoma del Edo. de Puebla, 1996

M. Energía Solar (Hons), Universidad Nacional Autónoma de México, 1999

A THESIS SUBMITTED IN PARTIAL FULFILLMENT OF THE REQUIREMENTS FOR THE DEGREE OF

DOCTOR OF PHILOSOPHY

in

THE FACULTY OF GRADUATE STUDIES

(Mechanical Engineering)

THE UNIVERSITY OF BRITISH COLUMBIA

(Vancouver)

October 2008

Abstract

Water transport across Nafion membranes was investigated under activity gradients at atmospheric pressure. The activity gradients across the membrane were controlled by exposing one side of the membrane to dry gas under laminar flow, while maintaining liquid or vapour equilibrium with water on the other side of the membrane. The measurements were made under steady state and transient conditions.

The main objective was to identify the rate limiting mechanism among the three major water transport processes in Nafion: diffusion in the bulk, and sorption across both interfaces. The proposed hypothesis was to represent the overall water transport across the membrane as the sum of resistances across the membrane bulk and interfaces.

The experimental implementation required new hardware and techniques. A dual chamber cell with temperature, humidity, and pressure control was designed with a gated valve to control the initial starting time for transient measurements. Unlike previously reported work, this design enabled the individual control of membrane thickness, temperature, pressure, relative humidity, and dry gas flow rate in each chamber.

The ability to control these variables made the experimental results amenable to theoretical simulations. Two phenomenological models were proposed to separate the contributions of bulk transport and sorption processes. The Varying Diffusion Coefficient model (VDC) was a preliminary effort to generate mass transport coefficients. The Vaporization-Exchange Model (VEM) provided an approximation for the steady state and transient water transport data through the definition of a novel boundary condition that describes the kinetics at the interface, while diffusion is described by Fick's law.

The VEM yielded interfacial water transport rates: k_v= 0.75 cms^{-1} for liquid-, and k_v= 0.63 cms^{-1} for vapour-equilibrated membranes. Such results contribute to fill the gap for the membrane interfacial kinetics in the fuel cell literature. The analysis with the VEM revealed that interfacial water transport became rate limiting at membrane thickness below ca. 100 μm.

Analysis of transient data with VEM generated bulk diffusivity coefficients: D=2-7x 10^{-10} m^2s^{-1}, for liquid equilibrated membranes at 30-70°C, which agreed with literature data.

A case study is presented for Nafion-SiO_2 composite membranes to study the effect of the membrane water content, by addition of silicon dioxide to Nafion membranes. The status of water in the membrane was characterized with long-established techniques, such as vapour sorption, scanning calorimetry, and water uptake measurements. Information from these measurements was coupled with measurements from the dual chamber cell. Experimental results indicated a threshold at 16 wt% of silicon dioxide above which the water transport properties of the composite differed significantly from additive-free Nafion. Analysis with the VEM suggested that the addition of the composite produced structural changes to the polymer matrix.

Table of Contents

Abstract ii

Table of Contents iv

List of Tables vi

List of Figures vii

Acknowledgements xvi

1. Introduction 1

1.1 Proton Exchange Membrane Fuel Cells 1

1.1.2 Water Management in PEMFCs 3

1.2. Proton Exchange Membranes 5

1.2.1 Perfluoro sulfonic acid membranes 6

1.2.2 Alternative Membranes 10

1.2.2.1 Composite Membranes 13

1.3 Research Outline 14

2. Literature Review 17

2.1 Structure of Nafion membranes 17

2.2 Water Transport Properties in PFSA membranes 20

2.3 Theoretical Studies of Water Transport in Nafion Membranes 23

2.3.1 Water diffusion 24

2.3.2 Transport in porous media 25

2.3.4 Vapour sorption and desorption 27

2.3.5 Transport through the membrane's bulk and interfaces: diffusion, and sorption 28

2.4 Experimental determination of Mass Transfer coefficients 29

2.4.1. Diffusion coefficient 29

2.4.2 Interfacial mass transport coefficients 33

2.4.3 Aims of this research 39

3. Experimental Methods 41

3.1 Membrane Preparation 41

3.1.1 Membrane activation 41

3.1.2 Nafion 115- silicon dioxide composite membranes 42

3.2 Water Transport Experimental Concept 43

3.3 Permeability Cell 45

3.3.1. Experimental set up, instruments and sensors 49

3.3.3 Activity gradient 54

3.4 Water Transport Experimental Protocols 56

[Original document was missing page v]

List of Tables

Table 1.1 Physicochemical characteristics of perfluorinated sulfonic acid (pfsa) membranes. [25-28] 7
Table 1.2. Properties of alternative proton exchange membranes in comparison to nafion . Modified from [25,44,45]. 12
Table 1.3 Thesis overview 16
Table 2.1. Diffusion coefficients, experimental techniques 32
Table 2.2. Summary of relevant interfacial mass transfer coefficient reported values..... 36
Table 2.3. Summary of the most relevant experimental approaches related to this thesis 38
Table 3.1. Properties of Nafion 115/SiO_2 composite membranes [45]..... 43
Table 3.2. Illustrative example of the effect of varying the gas flow rate on the water activity..... 55
Table 3.3. Coefficient values [89] for apour pressure Equation (3.7): 57
Table 3.4. Water uptake, water content and weight of wet membrane data for Nafion 115 and Nafion 115/ SiO_2 membranes under fully saturation at 25°C. 66
Table 3.5. Enthalpy of fusion measured by DSC for Nafion 115 and Nafion 115/ SiO_2 membranes 69
Table 4.1. Activation energy for Nafion 115 membranes equilibrated with liquid and vapour water..... 77
Table 5.1. Summary of diffusion and surface transfer coefficients from model for liquid equilibrated Nafion 112 and 117 at different temperatures. The best θ fit is shown for each experiment..... 99
Table 5.2 . Steady state response from analysis with VEM..... 103
Table 5.3. Bulk permeability Dc_{max} and interfacial k_v of nafion in LE and VE Nafion at 50°C..... 105
Table 5.4. Summary of Diffusivity coefficient (D), water concentration in the membrane (c^L_{max}) and the corresponding dimensionless vaporization rate (γ). 110
Table 6.1 Properties of Nafion 115/SiO_2 composite membranes. 113
Table 6.2 Descriptors of Equation 6.1 components..... 127

List of Figures

Figure 1. 1 Proton Exchange Membrane Fuel Cell 1
Figure 1.2 Water dynamics in proton exchange membrane fuel cell 5
Figure 1.3 Polymeric chemical structure of Nafion (m=1; x=5-13.5; n=2; y=1) 7
Figure 1.4. Schematic illustration of Nafion microstructure from Li [15]. 8
Figure 2.1. Model by Gierke of spherical ionic clusters. Adopted from Gierke [53] 18
Figure 2.2. Model by Weber and Newman. Modified from [55]. 19
Figure 2.4. Diffusion coefficient as a function of membrane water content. Adapted from Motupally et al. [19] 31
Figure 3.1. Setup for water transport experiments 44
Figure 3.2. The gate valve is pneumatically controlled to connect/disconnect the membrane with the wet chamber. 45
Figure 3.3. The wet and dry chambers were separated by a membrane holder. 46
Figure 3.5. Top isometric view of the permeability cell 48
Figure 3.6. Membrane assembly process 49
Figure 3.7 Complete experimental setup for water transport measurements 51
Figure 3.8. The vapour pressure was measured at different helium flows and temperatures. 57
Figure 3.9. For each experiment, the steady state vapour pressure was obtained from the plateau and plotted as a function of helium flow rate. 58
Figure 3.10. (a) Flux from steady state water transport for LE Nafion 117 at 30, 50 and 70°C 60
Figure 3.11 Measured time response to relative humidity step change from vaisala® dew point sensor. 62
Figure 3.12. Typical transient water transport signal. 64
Figure 3.13. DSC thermograms 68
Figure 3.14. Vapour sorption and desorption kinetics resulting from varying the atmospheric relative humidity 70
Figure 3.15. Membrane water content vs. Water activity for Nafion 115 and Nafion 117 71

Figure 4.1. Measured steady-state water flux was measured..... 74
Figure 4.2. The measured flux across Nafion 115 is shown at atmospheric pressure for varying the temperature. 76
Figure 4.3. Measured steady state flux of water across Nafion 115 membranes comparing isothermal (solid) and non- isothermal (hollow) conditionss. 79
Figure 4.4. Calculated resistance to water transport for Nafion 115 80
Figure 4.5. The water concentration corresponding to fully saturated gas mixtures at different temperatures. 82
Figure 4.6. Comparison of water flux across membranes with different thicknesses. 84
Figure 4.7. Comparison of water fluxes at 50°C from three different thicknesses: 51:127:183 μm in their expanded form. 86
Figure 4.8. Comparison of physical state of water in contact with the membrane during transient water transport..... 88
Figure 4.9. The flux derivative is compared for a Nafion 117 membrane in LE and VE conditions..... 89
Figure 4.10. The acceleration of the flux across the membrane as a function of time. 91
Figure 4.11. Measured times in LE Nafion 112 and 117 membranes 93
Figure 5.1. Experimental *vs.* simulated transient data for initially dry membranes.. 97
Figure 5.2. Experiment vs. simulation transport flux across Nafion 112 (left), and Nafion 117 (right) 98
Figure 5.3. Measurements of (1-RH)/RH as a function of the gas velocity 104
Figure 5.4. Linear fits of the slopes from Figure 5.3 *vs.* Nafion 11*x* thickness in liquid and vapour equilibrated membranes..... 104
Figure 5.5. Representative linear fit of long-time response. LE Nafion 117..... 108
Figure 5.6. Simulation (lines) and experimental (dots) data in the short-time for LE Nafion 117 at 30, 50, and 70°C..... 109
Figure 6.1. Vapour water isotherms for Nafion 115/SiO_2 composite membranes at 25°C 117
Figure 6.2. Rate of change for sorption. 118
Figure 6.3. The state of water as a function of SiO_2 content in Nafion 115 membranes. 119

Figure 6.4. Steady state water transport fluxes in unmodified Nafion 115 (0 wt% SiO_2), and Nafion/SiO_2. 122
Figure 6.5. Thickness dependency for steady state water transport across Nafion/SiO_2 composite membranes 124
Figure 6.6. Fitting lines for measured (1-RH)/RH data *vs.* gas velocity 125
Figure 6.7. The slopes from Figure 6.6 are plotted against the content of SiO_2 wt% for LE and VE composite Nafion membranes. 126
Figure 6.8. A one-dimensional, steady state approximation with continuous water concentration profiles 129
Figure A.1: Control volume in the dry chamber of the permeability cell 145
Figure C.1:Setup for dew point temperature sensor cross-reference. A saturated atmosphere was kept during measurements. 159
Figure D.1. Membrane water content *vs.* Water activity for Nafion 115 and Nafion 117 at different temperatures, from different sources 163
Figure D.2 The effective water diffusivity for le (left) and vapor-gas equilibrated membranes (right) from permeation measurements. 165

[Original document was missing pages x-xi]

Nomenclature

a	Dimensionless water activity in chamber	
a	Concentration of SO_3 in the membrane (Only in section 5.1)	mol SO_3 m^{-3}
A	Membrane superficial area	m^2
c_{max}	Max. membrane water concentration	mol / cm^3
c_w	Concentration of water	mol / cm^3
D_w	Diffusion coefficient of water	m^2/ s
D_{eff}	Effective diffusivity	m^2/ s
e^-	Electrons	
F	Faraday constant	coulomb / mol
H_2	Hydrogen	
$H+$	Protons	
H_2O	Water	
i	Current density	A / m^2
$O2$	Oxygen	
J_w	Flux of water across the membrane	mol / m^2 s
k_a	Absorption mass transfer coefficient	m / s
k_d	Desorption mass transfer coefficient	m / s
k_p	Effective hydraulic permeability coefficient	cm^2
k_v	Interfacial mass transport rate for liquid and vapour equilibrated membranes	m / s
L	Membrane thickness	m
M_{dry}	Molecular weight of dry Nafion	gr / mol
$\dot{n}_{He}$	True gas flow	mol / s
n_{SO}^{-3}	Moles of SO^{-3} species	mol
P_{atm}	Atmospheric pressure	bar
P_L	Partial pressure of water	kPa
P	Pressure in chamber	bar

P_w	Vapor pressure	bar
P^{sat}	Saturation pressure	bar
r	Pore radius	cm
Q	Equivalent weight	gr dry Nafion / mol SO_3
R	Ideal gas constant	J / K mol
RH	Relative humidity	
T	Chamber temperature	°C
x	Membrane thickness	μm
X	Water mole fraction	
V	Chamber volume	cm^3
$\bar{V}$	(Partial) molar volume of water	cm^3 / mol
$\dot{V}$	Gas flow rate	$cm^3 min^{-1}$
W_b	Bound water weight in the membrane	g
Wn_b	Non-bound water weight in the membrane	g
W_t	Total water weight in the membrane	g

Greek

α	Mass transport coefficient	$mol^2 J \cdot cm \cdot s$
Δ	Difference	
∇	Gradient	1/length
η	Viscosity of water	Pa·s
λ	Membrane water content	mol H_2O/mol SO_3^-
γ	Surface tension of water (Only in Eq. 2.7)	N / cm
γ	Dimensionless vaporization rate	
μ	Chemical potential	J / mol
θ	Internal contact angle (Only in Eq. 2.7)	deg

θ	Dimensionless concentration	
θ^{∞}	dimensionless steady-state concentration	
ρ_{dry}	Density of dry Nafion	gr / m^3
ω	Dimensionless electro-osmotic drag coefficient	
τ	Time domain	

Subscript and Superscript

1,2	Chamber side (1=wet chamber , 2=dry chamber)
A	absorption
D	desorption
C	Capillary
G	Gas phase
He	Helium
H^+	Protons
int	Interfacial
L	Liquid phase
max	Maximum
$N115/SiO_2$	Composite membrane (Nafion 115 doped with SiO_2)
sat	Saturation
SO_3	Sulfonic ion groups
ss	Steady state
t	Time
V	Vapour phase
v	Vaporization
w	Water

Abbreviations

AFM	Atomic Force Microscopy
BT	Back Transport
EOD	Electro-osmotic Drag
EW	Equivalent Weight
FTIR	Fourier Transform Infrared Spectroscopy
IFCI	Institute for Fuel Cell Innovation
LE	Liquid Equilibrated
MRI	Magnetic Resonance Imaging
NMR	Nuclear Magnetic Resonance
NRC	National Research Council
ODE	Ordinary Differential Equation
PEM	Proton Exchange Membrane
PEMFC	Proton Exchange Membrane Fuel Cell
PFSGE	Pulsed Field Gradient Spin-Echo
SANS	Small Angle Neutron Scattering
VDC	Varying Diffusion Coefficient
VE	Vapour Equilibrated
VEM	Vaporization-Exchange Model
WT	Water Transport

Acknowledgements

I would like to start thanking my supervisor, Dr. Walter Mérida for his support and outstanding mentorship during this project.

I want to thank the members of my committee Dr. David Wilkinson, Dr. Michael Eikerling and Dr. Bryan Wetton for the insightful discussions throughout these years and for reviewing this thesis in spite of their busy agendas.

I thank Dr. Charles Monroe for many insightful discussions, which helped to enlarge my vision of science.

Thanks to Dr. Titichai Navessin, Dr. Steven Holdcroft ant the MEA group at NRC-IFCI for their help in sample preparation, support, and advice regarding this research.

I would like to thank the previous and present members of Dr. Mérida's group: Robbie, Ignacio, Chris, Saúl, Peter, Amir, Galvin, Omar, David, Ed, Shensheng, and Michael, for their friendship and motivational discussions throughout these years. I was very lucky to be part of this group.

I thank my proof readers, Edward McCarthy, Mario Delgado, and David Kadylak,. My special gratitude is to my friend Edgard Neudorf, who not only did an exhaustive work proofreading this thesis but was also a constant source of encouragement during the writing process.

I was fortunate to share these academic years with people who enriched this experience with inspirational discussions and warm friendship. My sincere thanks to Dr. Olivera Kesler, and fellows Ignacio Valenzuela, Peter Cave, and Makoto Adachi for these years of priceless memories.

I could have not been able to finish this thesis without balancing it with good times and good friends. Thanks to Monica Danon-Schaffer and Scwist members for being good mentors and friends. Thank you to my friend José Alberto Félix for his moral support in the last years. Thanks to all members of my *futbol* team for their support and encouragement in the good and hard times.

I would like to express my deepest gratitude to my parents: Rosa Luz and Salvador, for their unconditional love and the sacrifices they have made for me throughout my study life. I thank my siblings Gabriela, Salvador, and Estela for their encouragement and understanding during my unavailable times in the last years. My gratitude is also for my beloved godparents, Pablo (rip) and Eva Castañón who encouraged me to pursue my dreams. (Gracias familia por apoyarme una vez más)

Finally, I want to profoundly thank to Rubén, my husband, who has been my pillar throughout these years. This journey is much his as it is mine. Without his patient love and care I would not have been able to accomplish it. (Gracias Rubén por tus cuidados cariño, y paciencia).

1. Introduction

1.1 Proton Exchange Membrane Fuel Cells

Proton Exchange Membrane Fuel Cells (PEMFCs) are electrochemical reactors that generate electrical energy from a continuous supply of fuel and oxidant gases, being these in the most general case, hydrogen and air, respectively. PEMFCs comprise two electrodes; a cathode, and an anode, and a solid membrane, which acts as ionic conductor (see Figure 1.1). Current PEMFC technology, using hydrogen as fuel, offers power generation ranging from 10^{-1} to 10^{5} W with lower CO_2 emissions and higher efficiencies than combustion engines. These advantages have motivated its broad application for powering from portable to transportation systems.

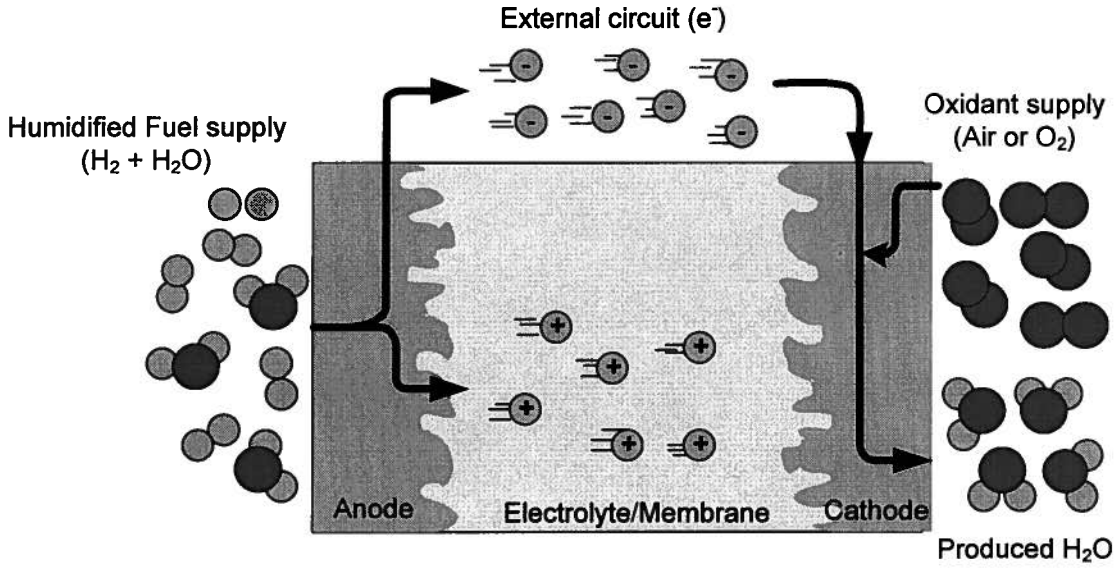

$$H_2\,(g) + \tfrac{1}{2}\,O_2\,(g) \longrightarrow H_2O\,(l) \qquad < 100\,^{\circ}C$$

Figure 1. 1 Proton Exchange Membrane Fuel Cell

Despite their advantages, the commercialization of PEMFCs is still limited mainly due to the limited hydrogen supply infrastructure. Also, the availability of pure hydrogen, required to maintain a free of emissions- life cycle, is restricted to expensive technology that is not widely spread in the industrial world, such as elecotrolysis. Instead, industrial hydrogen production relies on extraction from fossil fuels which disrupts the zero-emission-technology concept.

Other limitations to the massive commercialization of PEMFCs are high manufacturing cost, limited components lifetime, reliability, and the need to simplify the support sub-systems [1]. Gas compression, power conditioning, cooling, and water management are examples of the required subsystems of a fuel cell. The work presented here addresses the fundamental processes related to the water management approaches.

Proper water management is indispensable for optimal PEMFC operation. The membrane must be hydrated to enable protonic conduction, but water in other regions (most notably the electrode layers) can hinder the access of reactants to the active sites at the membrane-catalyst interface. As a result, modern membrane electrode assemblies (MEAs) incorporate advanced water management schemes including reactant humidification [2,3], hydrophobic treatment of the electrode substrates [4] and multi-layer MEA structures incorporating micro-porous materials [5,6].

Faulty water management is the main cause for flooding and dryness in the cell, two of the most common failure modes of PEMFCs. During such failures, fundamental reaction pathways are affected, leading to decreased performance and lifetime.

1.1.2 Water Management in PEMFCs

Failure can be prevented by suitable water management strategies[2,3,7-10] which in many situations have relied on trial and error practices for optimisation. A more rational optimization process requires a clear understanding of the water transport mechanisms in PEMFCs.

Two main transport mechanisms move the water across the membrane: Back Transport (BT), and Electro-osmotic drag (EOD) towards the cathode[11-14]. The balance of these two processes determines the activity gradient of water across the membrane.

During operation, cathodic reactions produce water at the membrane-electrode interface. Evaporation takes place and the water is partly convected out with the reactant gas; the rest is transported trough the membrane towards the anode.

As protons cross the membrane, a shell of solvating water molecules surrounding the positive ion travels with it to the cathode, creating the so called EOD effect, which is a function of the current load as shown in Equation (1.1) [15]:

$$N_{eo} = \omega N_{H^+} = \omega \frac{i}{F} \qquad \textbf{(1.1)}$$

where, N_{eo} is the flux of water due to EOD; ω, is the EOD coefficient, i.e. the number of water molecules accompanying the proton, and N_{H^+}, is the flux of protons as a function of current density [16-18]. This EOD coefficient is not constant; it has been proven that this value is a function of the number of ionic sites in the membrane, the porosity of the

membrane, the operation temperature, the water activity, and of the current density. As shown in Equation (1.1), an increase in current produces an increase in the flux of water to the cathode side of the membrane.

On the opposite direction, BT of water to the anode, results from the concentration gradient formed across the membrane when water is produced at the cathode. BT can also be induced through application of a pressure gradient across the membrane-electrode assembly. A common approach to study this phenomenon is through Fick´s first law of diffusion, which describes the proportional flux of water due to the water concentration gradient in the membrane [19]:

$$J_{BT} = -D_{eff} \nabla c_w(\lambda) \tag{1.2}$$

where D_{eff} is the diffusion coefficient of water, and c_w is the water concentration.. D_{eff} has also been reported to be a function of the membrane hydration level (λ).

As the current load increases, the EOD flux overcomes BT, resulting in a net transport of water from anode to cathode. This excess water content can cause flooding on the cathode side. As a consequence of the flooding, the gas diffusion layer (GDL) pores are blocked [20], impeding the passage of reactants to the triple-phase zone in the catalyst layer [6,9,21], contributing to mass transport limitations. Flooding also reduces the availability of electroactive surface, increasing the activation overpotential of the cathodic half-reaction. Additionally, due to the effect of EOD, the anode side may be dehydrated, increasing the resistivity of the membrane and leading to steep ohmic drops in current-voltage plots.

In practical PEMFC applications, it is common to use humidified reactant gases to prevent membrane dehydration [22,23]. Usually, humid hydrogen is fed to the anode to keep it hydrated. Meanwhile, at the cathode side, a temperature increaseof the fuel cell can vaporise the water produced by the cathodic reaction. As a result, the membrane is in contact on one side, with liquid water and vapour on the other, and the water uptake rate consequently differs on each side of the membrane. This also impacts, BT and EOD[24]. Figure 1.2 illustrates the water dynamics in the membrane-electrode assembly.

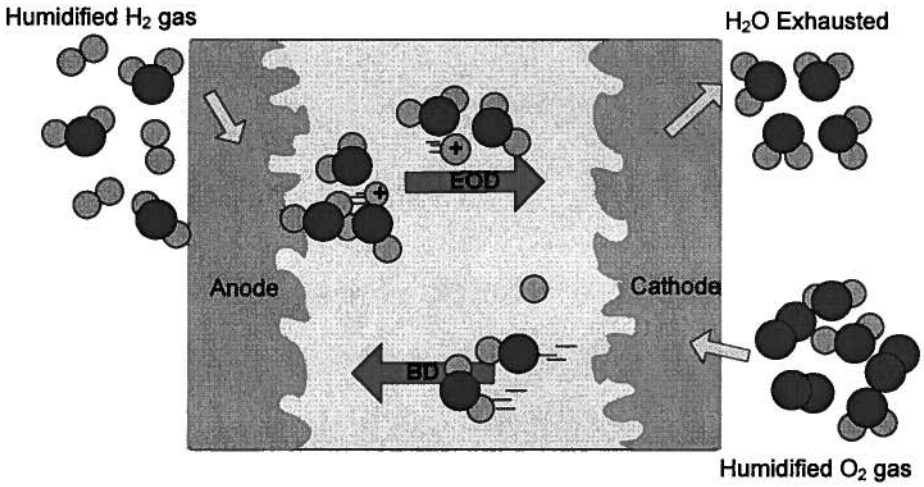

Figure 1.2 Water dynamics in Proton Exchange Membrane Fuel Cell

1.2. Proton Exchange Membranes

Proton exchange membranes (PEMs) play an essential role as ion conductors and gas separators in PEMFCs. In order to be used as electrolytes in fuel cells they must comply with main requirements[15]:

- chemical stability
- mechanical stability
- impermeable to gas

- resistance to dehydration
- high proton conductivity (~ 0.1 Scm^{-1})
- low production cost

Usually, PEMs are thin films (<100 μm) of solid polymer electrolytes with ionic functional groups (i.e., sulfonic acid groups) acting as protons.

1.2.1 Perfluoro sulfonic acid membranes

The chemical structure of PEMs consists typically of fluoroethylene backbone with sulphonated-terminated, perfluorinated vinyl-ether branches which allow proton exchange between the polymer networks created.

Gore and Nafion have been considered the standard membranes for commercial fuel cell (PEMFC) technology. Other commercial brands are Flemion™, and Aciplex™ (See Table 1.1). Nafion membranes are the focus of the present study.

Even though Gore is currently considered the standard membrane for commercial fuel cells (more than Nafion), its availability is limited for industrial applications only. Its use for research projects is not easily granted and very little information is publically available. Nafion is the commercial name from Dupont; its introduction to the market started with the space programs in the 1960's

The Nafion structure is formed by the copolymerization of poly tetrafluoroethylene (PTFE) and polysulfonyl fluoride vinyl ether. The incorporation of these two polymers provides Nafion with two phases: a hydrophobic Teflon-type backbone, and a hydrophilic phase associated to the vinyl ether side chains with sulfonic acid groups terminations.

Table 1.1 Physicochemical characteristics of perfluorinated sulfonic acid (PFSA) membranes. [25-28]

Trademark	Type Membrane	Structure parameters	Thickness (μm)	Equivalent Weight (g molSO_3^{-1})	Water Uptake (wt %)	Proton Conductivity (S cm^{-1})
Dupont	Nafion 112	m=1;x=5-13.5;n=2; y=1 (shown in Figure 1.3)	51	1100	36	0.1[a] 0.071[b]
	Nafion 115		127	1100	25	0.0043 0.0066[b]
	Nafion 117		183	1100	34	0.0133[c] 0.09[d]
Asashi Chemicals	Aciplex	m=0; n=2-5; x=1.5-14	25-100	1000-1200	43	0.108
Dow Chemical[1]	Dow	m=0; n=2; x=3.6-10	50:125:250	800-900	54	0.114
Asashi Glass	Flemion	m=0; n=1-5	50:80:120	1000		

[1] Not commercially available. Conditioned in [a] water at 100°C , [b] water at 25°C, [c] 100%RH at 30°C, [d] 100%RH at 25°C

A representation of the chemical structure of Nafion monomer is shown in Figure 1.3.

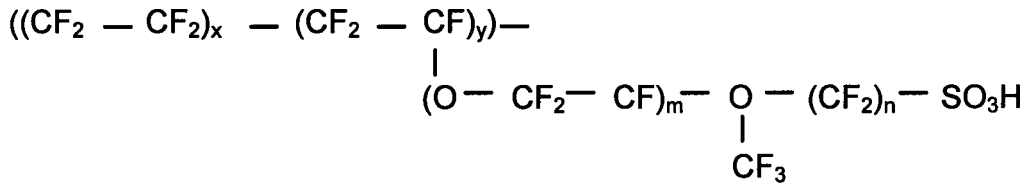

Figure 1.3 Polymeric chemical structure of Nafion (m=1; x=5-13.5; n=2; y=1)

Nafion chemical stability and mechanical strength is provided by the strong Teflon-type backbone (See Figure 1.4). The hydrophilic phase is flexible enough to swell and absorb water to increase the weight of the dry membrane as much as 50% (or up to 100% when it is contact with liquid water)[15]. The association of water will then depend largely on the number of acid groups associated per gram of dry polymer, i.e., Ion-exchange capacity.

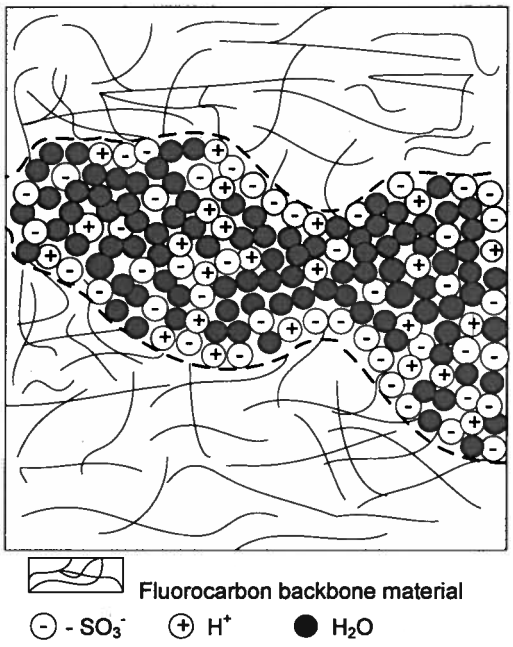

Figure 1.4. Schematic illustration of Nafion microstructure with the hydrophilic side chains and hydrophobic backbone structure. Modified from Li [15].

The measure of ionic content in the polymeric membrane can also be represented by the Equivalent Weight (EW= 1000/ IEC):

$$\text{Equivalent Weight (EW)} = \frac{g \quad dry \quad Nafion}{mol \quad SO_3^-} \tag{1.3}$$

It has been reported that water content influences proton and water transport properties of Nafion[17,29-31]. The water content (λ) is reported as the number of water molecules present in the polymer in terms of the number of ionic sites:

$$\lambda = \frac{mol\ H_2O}{mol\ SO_3^-} \tag{1.4}$$

In practical applications for PEMFC, the membrane equivalent weight ranges between 800-1500 EW [32]. For Nafion, the most common EW is of 1100. Thus, the number of water molecules associated to each ionic site would depend on the relative amount of water absorbed by the membrane in terms of its dry weight (i.e., water content, λ. See Equation 2.1 in Section 2.2). Section 2.2 includes an overview of the current discussion in the literature of fuel cells regarding the quantification of water content in Nafion membranes.

The membrane undergoes recurring shrinking and swelling cycles due to water content fluctuations [33-35]. The swelling pressure is counterbalanced by elastic pressure exerted by the polymer matrix which prevents dissolution of the membrane in polar solvents. Because the chemical stability of Nafion is compromised above its glass transition temperature (~110°C), PEMFCs systems operate at approximately 80°C to prevent irreversible damage to the chemical structure by keeping water in its liquid phase. Even though this temperature lies below the boiling point, the temperature is high enough to maintain a two phase water system. The need for constant humidification and low temperatures for water management restrict operating regimes of fuel cells significantly.

Research efforts towards the use of high temperature [36-38] and low humidity [3,8,39,40] operation in PEMFCs could render humidification obsolete or unnecessary, but current designs still rely on humidified reactants. Despite significant advances in polymer design and manufacturing techniques [25,41-43] Nafion continues to provide a useful standard for commercial PEMFC applications.

Nafion membranes have been studied from different perspectives to understand their dual performance as proton conductors and water transport media. The membrane requires humidity to conduct ions and poor water management therefore decreases the accessibility of the reactants to the ionic sites, decreasing the system performance and lifetime.

1.2.2 Alternative Membranes

The mechanical and chemical stability of PEMs become compromised at high temperature and low humidity. Another challenge for the PEMs is their frequent volume change due to swelling and shrinking. A membrane that does not swell would represent a solution for stable and long lasting seals in PEMFCs, a common source of mechanical failure. These disadvantages of Nafion have increased research interest to produce alternative materials that operate in environments above 120°C and below 50%RH, and are less prone to swelling.

Table 1.2 shows the current classification of alternative membranes. The table shows some of their physical properties and performance in comparison to perfluorosulfonic acid (PFSA) membranes. The scarcity of factual information is due to the variability of material combinations found in the literature which makes it difficult to present a consistent comparison between material properties.

With temperatures above 100°C, water transport would occur in a single vapour phase domain. However, high temperature opens up another challenge: the need for more robust ionic conductors than Nafion, such as composite membranes.

Table 1.2. Properties of alternative proton exchange membranes in comparison to Nafion . Modified from [25,44,45].

Category	Structure	Thickness (μm)	Proton Conductivity ($S\ cm^{-1}$)	Physico- chemical Characteristics
Partially Fluorinated	Fluorocarbon base with hydrocarbon aromatic side chain	25-200	10^{-1}	• Mechanically stronger • Less durable and less chemically stable
Non Fluorinated Hydrocarbon	Hydrocarbon base with polar groups		10^{-1} –10^{-3} [a]	• Mechanically stronger • Lower chemical and thermal stability
Non Fluorinated Aromatic	Aromatic base with • Polar • Sulfonic acid group		~ 10^{-2}	• Mechanically stronger • Chemical and thermal stability at temps. up to 300°C • Improved water uptake
Acid-Base polymer	Acid into alkaline polymer base		10^{-1}	• Thermally and chemically stable • Improved dimensional stability. Durability to be proven.
Modified PFSA: Reinforced membranes:	Nafion impregnation into PTFE	50-76 [45]	~ 10^{-2}	• 300-2000 MPa (Young's modulus) • Dimensionally stable • ~ 50% less water uptake
Modified PFSA: Composite doping	• Nafion doped with SiO_2 • Nafion doped with Zirconium phosphate • Nafion doped with phosphoric acid		10^{-3} [b] 10^{-4} [c] 10^{-2} [d]	•~ 20% higher water uptake

[a] at 20-140°C

[b] at 120°C & 40%RH

[c] at 60°C (vs 10^{-3} for Nafion same conditions)

[d] at 175°C

1.2.2.1 Composite Membranes

Hygroscopic inorganic composite membranes are reported to offer improved thermal and chemical stability at temperatures above 100°C. By sol-gel reactions, Nafion membranes can be modified with addition of inorganic nanoparticles. TiO_2 and SiO_2 are examples of additive materials that sustain chemical stability at high temperatures and maintain good proton conductivity under such conditions.

SiO_2-Nafion membranes have shown improved water content and proton conductivity due to the hygroscopic properties of the silica [42,46-48]. The addition of the composite provides higher water retention for the membrane and conductivity at high temperatures. Proton conductivity in composite Nafion has been reported in the order of 10^{-7} to 10^{-5} Scm^{-1} at 100°C.In Nafion, sol-gel reactions occur in the polar clusters inside the membrane, generating SiO_2 nanoparticles which fill in clusters associated with the ionic SO_3^- sites [49].

Researchers have targeted SiO_2-Nafion membranes to produce self-humidifying membranes in order to eliminate PEMFCs' current dependence on humidification systems. In spite of the interest, a clear explanation of how the membrane performs in relation to its water transport has not been presented. Changes of mechanical properties such as coefficients of volume expansion, pore-size distributions, and shear or bulk moduli, after the addition of SiO_2, may be associated with the improved performance of the composite membranes in the fuel cell.

Alternative membranes, is a topic of increasing research interest. In the search for optimization of water management and reduction of support subsystems in PEMFCs, alternative membranes offer a viable solution. Improved proton conductivity at higher

temperatures, longer lifetime, and manufacturing cost reduction are the current research interests.

1.3 Research Outline

Chapter 1 centers on the motivation for the study of water transport mechanisms in proton exchange membranes based on the demand for proper water management in PEMFCs.

Chapter 2 describes the evolution of water transport in Nafion membranes in the last 20 years from the more qualitative studies to the more fundamental by incorporation of the surrounding effects to the material water transport properties. The use of spectroscopic techniques (i.e., NMR, FTIR) have allowed isolated membrane studies to outline the morphology and main characteristics of the polymer in the presence of water. It also explains how the research interest of this thesis lies on correlating environmental, membrane structure and water transport mechanisms. The experimental approach used on this thesis focused on overall empirical environmental variables, such as temperature, humidity, pressure, composition, and gas flow rate, rather than on physical changes in the membrane.

Chapter 3 describes the experimental work: membrane preparation, the permeability cell designed to measure water crossover across PEMs, and the protocols to measure and analyze water transport under steady state and transient conditions (Sections 3.1 to 3.2). Other complementary and existing techniques used for characterization of water transport properties are described in Sections 3.3 to 3.5. The focus of this work is on the investigation of Nafion water transport within the range of operational conditions and parameters common to fuel cell systems. The effect of the activity gradient acting as a

mass transport driving force, and the water phase in contact with the membrane were explored under experimental conditions.

Chapter 4 presents experimental results from the measurements with the permeability cell under steady and transient state. Isothermal and non-isothermal experiments generated results that provided insight on the importance of the interfaces for the mechanisms of water transport. Thickness and temperature measurements under steady state and transient regimes guided the development of two phenomenological models to describe the role of the interfaces during water transport.

Chapter 5 describes both models based on a resistance in series configuration to accounting for the bulk and interfacial mass transport. The firs model, the Varying Diffusion Coefficient (VDC) model analyzed transient water transport data as a preliminary exercise to deconvolute interfacial sorption from bulk diffusion. The second model, the Vaporization-Exchange Model (VEM) analyzed the steady state and transient water transport and considered a dynamic boundary condition to describe a bidirectional flux resulting from the reaction kinetics of water vaporization at the membrane surface. The VEM allowed deconvolution of individual contributions to the overall water transport; it provided simultaneous information about the mass transport rates for the membrane-gas interface and diffusivity coefficients for the bulk.

In Chapter 6, a study of water transport is presented for Nafion-composite membranes and the effect of increasing the membrane water content on the structural and water transport properties of the membrane is discussed. The analysis included permeability measurements and various membrane characterization techniques. Table 1.3 shows the thesis content overview.

Table 1.3 Thesis overview

Objective: Investigate the mass transport mechanisms of water in Nafion membranes by including boundary effects under typical operating conditions of PEM Fuel Cells

Justification: Current models fail to represent precisely the differing water transport mechanisms in the bulk and across boundaries under the effect of external driving forces

	Tasks accomplished:
Ch. 1 Introduction	• Motivation for this research
Ch. 2 Literature Review	• Evolution of water transport research in Nafion

Ch. 3 Experimental	• Developed analysis tool to characterize water transport in PEM:
	  • Designed permeability cell with individual temperature control and time zero control
	  • Measured water transport across Nafion membranes under steady state and transient conditions
	  • Investigated effect of membrane water content in water transport: SiO_2-Nafion membranes
	  • Compared water transport performance in Nafion and SiO_2-Nafion membranes
	  • Characterized composite-membranes for water uptake, vapour sorption and desorption, and differential scanning calorimetry

Ch. 4 Results and Discussions	• Found evidence of the importance of interfacial mass transport in steady state and transient water transport.
Ch. 5 Mathematical Models	• Identified interfacial and bulk mass transfer rate constants from steady state permeability. • Confirmed diffusivity coefficients from transient water permeability
Ch. 6 A case study : water transport dependency on water content in Nafion/composite membranes	• Determined effect of increased water content in mechanisms of water transport
Ch. 7. Conclusions	

2. Literature Review

The structure and water transport properties of Nafion have been studied under different schemas. Experimental and mathematical modeling have widely described the polymeric membrane. In the same way, the water transport phenomena across Nafion have been analyzed under the effects of diverse gradients acting as driving forces. Each approach has partially described the complexity of Nafion, its water uptake, and transport capacity for better understanding and application in PEMFCs.

In Section 2.1 a review of the most significant transport mechanisms of water inside Nafion membranes is provided. Transport is described in terms of diffusion, permeability, and interfacial mass transfer mechanisms. In section 2.2, the experimental techniques to calculate diffusion and mass transfer coefficients are summarized. In section 2.3, a review of the physical models that have described the membrane structure is presented.

2.1 Structure of Nafion membranes

The morphology of Nafion has been modeled with the help of a wide variety of scattering methods: small angle x-ray scattering, and small angle neutron scattering.[50-52]. Through these measurements, Nafion has been identified as a two-phase material with certain cristalinity that disappears with increasing water content. The low crystalinity of the material makes the characterization of Nafion a challenge even for state-of-the-art techniques.

A model proposed by Gierke et al. [53] was the first to describe the complex morphology of Nafion as a cluster network. Based on X-Ray Scattering studies, it was proposed that Nafion is formed by random network of spherical clusters of ~40 Å, organized as inverted micelles. These clusters are connected by channels of ~10 Å diameter, as shown in Figure 2.1.

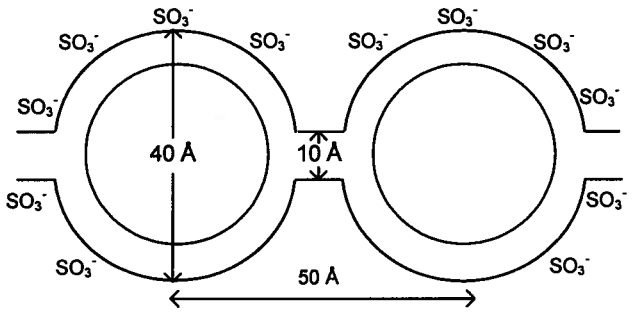

Figure 2.1. Model by Gierke of spherical ionic clusters. Adopted from Gierke [53]

Several other models presented proposals to explain the microstrucutre of Nafion. Yeager and Steck, and Gebel and collaborators [34,54], proposed hydrophilic pores of cylindrical shape surrounded by hydrophobic domains. Gebel used small angle scattering data to explain the shape shift from isolated spherical to cylindrical interconnected ionic clusters due to the swelling and dissolution processes during water uptake. Above 50 wt% water content, Gebel found a structural inversion resulting in acid groups outside the rod-like micellar structures, which created a hydrophilic surface.

The model from Weber and Newman [55], represented in Figure 2.2, describes the structural changes of the membrane as a function of the water content. The dry membrane absorbs water and solvate the acid groups. The further the addition of water, it causes the water to form clusters around the ions, so that inverted micelles are formed

and connect within each other. In the last stages, interconnections of water channels form the hydrophilic paths; this situation is expected for membranes saturated with water vapour (λ=14) , and fully saturated membranes (i.e., λ=22), as shown on the right of Figure 2.2.

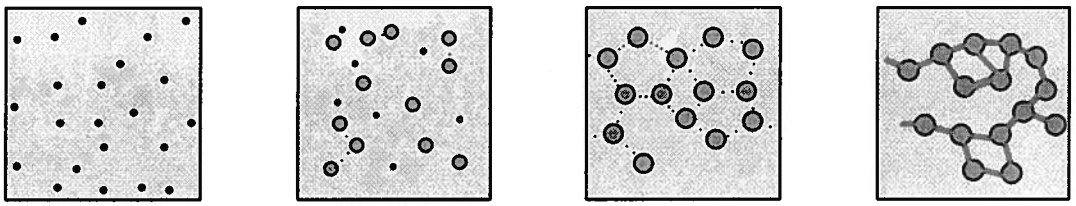

Figure 2.2. Model by Weber and Newman . Modified from [55]. The evolution of the membrane structure as a function of the water content (λ). The background represents the fluorocarbon matrix, the black is the polymer side chain, the gray is the liquid water, and the dotted line is a collapsed channel.

Schmidt-Rohr and Chen [52] simulated small angle X-ray scattering data and fitted it to different contemporary models. The authors found the best data fit with an array of parallel cylindrical channels of inverted micelles with polymer backbone on the outside, as represented in Figure 2.3. The model describes channels with diameters of ca. 2.4 nm. (spherical models calculate diameters < 1.2 nm). According to the authors, this ionic continuity explains the bulk-like water diffusivity under freezing temperatures across the membrane as the narrower channels will remain full.

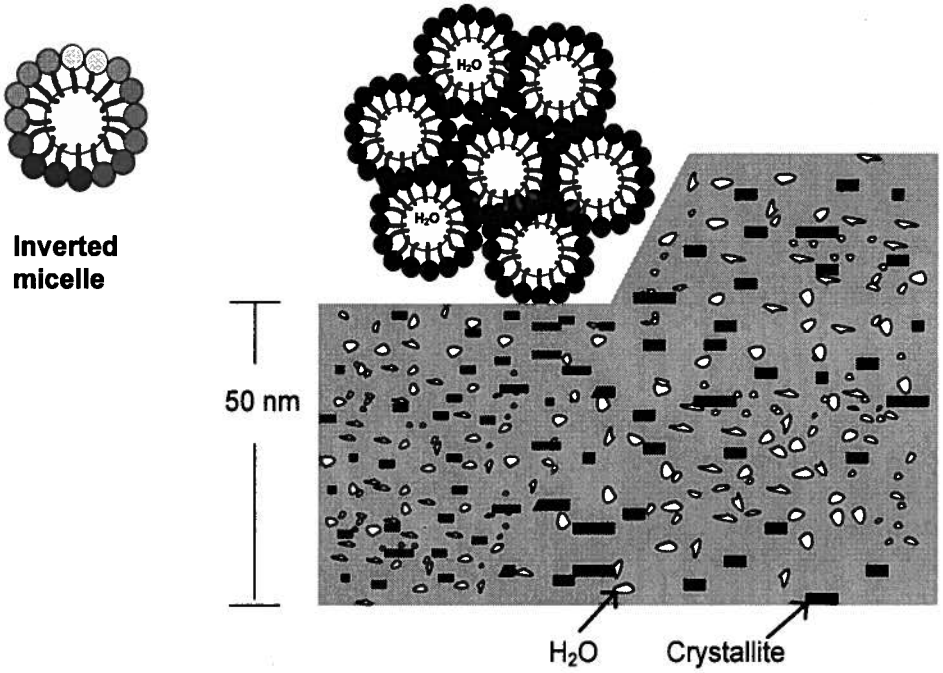

Figure 2.3. Model of parallel cylindrical nanochannels in Nafion. The inverted micelle cylinder with Teflon backbone on the outside and the ionic side groups in the channel (left). On the right, hexagonal packing of several cylinders. Modified from [52].

2.2 Water Transport Properties in PFSA membranes

Proton and water transport in Nafion are the most documented properties in the literature of fuel cells. This review, however, focuses on water transport properties only, such as diffusivity, mass transport coefficients, water content, etc.

Water sorption measurements have been used to characterize Nafion water uptake in liquid and vapour environments. Several authors [11,56] reported on the difference in equilibrium water content under liquid- and vapour-saturated environments, with λ=22 for the former and λ=14 for the latter. In the fuel cell literature, the term "Schroeder's paradox" is frequently used to describe this discrepancy. It is paradox, because in both

cases, the thermodynamic water activity is unity ($a=1$), but the equilibrium water uptake is higher for the membranes in contact with liquid..

The majority of the investigations agree that this difference is related to the physical structure of the membrane. Zawodzinski et al. [57] reported contact angle measurements and demonstrated that the membrane's top layer behaves hydrophobic when the surrounding environment is water vapour and it behaves as a vapour-equilibrated membrane even though it has been only recently removed from immersion in liquid water. Yet, it is believed its interior water content will remain high. The authors explained the phenomena as a reorganization of the surface to balance out the dielectric properties of the membrane with the environment.

The phase inversion has also been observed by FTIR surface spectroscopy measurements [58]. Gottesfeld et al. and Futerko and Hsing [59,60] agreed that the membrane remains in a stable thermodynamic state when it its equilibrated with vapour. When the membrane is in contact with liquid, the thermodynamic equilibrium is interrupted by the membrane swelling in order to accept more molecules.

All the reports based on gravimetric measurements found a difference between liquid and vapour water uptake. Varied physical explanations have contributed to the debate on whether the membrane changes its structural properties due to the chemical potential of the environment. Futerko and Hsing [60] proposed an explanation for the paradox based on the Flory-Huggins model based on the heat of mixing and entropy during the water kinetics. The model explains that at higher entropies and exothermic heat of mixing, the water uptake decreases, which explains the lower water content for saturated vapour equilibrated membranes. For the liquid case, the model found that the

polymer matrix surrounding the sulphonic acid groups has a strong interaction with the water molecules which generates an endothermic heat of mixing. As a result, the membrane increases its water uptake. The model agreed well with experimental observations of surface changes in the polymer matrix, which became hydrophilic when the membrane was in contact with liquid water [57,59].

Similarly, McLean et al. [61] studied the ionic domains on or near the surface of K^+ type Nafion membranes at room temperature and humidity using atomic force microscopy (AFM). They discovered that the membrane showed a thin hydrophobic layer of ca. 5 Å on the surface. The formation of a hydrophobic layer has been proposed by Majsztrik et al. [62] as an explanation for the lower water uptake in vapour sorption and permeation experiments.

Choi and Datta [63] explained the water uptake difference from vapour and liquid using the force equilibrium between the swelling pressure and the elastic deformation of the polymer. The model included details on the solvent polarity, the hydrophobic ratio in the polymer and the chemistry of the ionic groups. Accordingly, the liquid equilibrated membrane generates a chemical potential which accounts for the difference in water uptake.

The thermal history of the membrane has been related to the difference between vapour and liquid water uptake in perfluorsulphonic membranes. Hinatsu et al. [56] observed that the thermal history defines the polymer structure and hence the water uptake capacity. More recently, Onishi and collaborators [64] completed long term measurements on water sorption where the membrane-vapour system was left to reach equilibrium for up to two months. The data compared liquid and vapour water uptake

[Original document was missing pages 23-25]

This analysis assumes the membrane to be homogeneously saturated, neglecting concentration gradients. In sorption experiments concentration gradients tend to be large, so Equation 2.4 is a better approximation than 2.5.

According to Eikerling and collaborators [12], considering the Nafion membrane as a nanoporous material can drive to an alternative two-phase analysis in porous media, where contact angle (θ), surface tension (γ) and pore radius (r) define a capillary pressure by:

$$p_c = p_G - p_L = \frac{2\gamma \cos\theta}{r} \tag{2.6}$$

Since the capillary pressure balances out the advance of water inside the pores, this pressure can be considered the driving force for the liquid transport flux through the porous media by the expression:

$$J = -\frac{k}{\bar{V}\mu}\left(\nabla p_c + \nabla p_G\right) \tag{2.7}$$

When the system is under uniform gas pressure, ∇p_G is neglected. In this way, k is the permeability rate in a saturated medium.

Eikerling et al. and Weber and Newman [66,71] proposed a hybrid model based on the concentrated solution theory and a porous media treatment for the membrane. These models attempted to bridge the gap between one- and two-dimensional models and allowed the analysis within the range of vapour to liquid. The model incorporated a dependency of polymer structural change on water content based on capillary

phenomena. It described the evolution of the formation of channels and interconnections between them with the increase of water uptake.

2.3.4 Vapour sorption and desorption

A frequent approach in the analysis of Nafion water transport is done through the mechanisms of sorption and desorption in transient mode, described by the continuity of water in the membrane:

$$\frac{dc_w}{dt} + \vec{v} \cdot \frac{\partial c_w}{\partial x} = -\frac{\partial J}{\partial x} \tag{2.8}$$

Using boundary conditions that assume Henry's law, the water uptake is calculated in terms of the net change in membrane mass as it equilibrates with the ambient water vapour pressure. Some kinetic studies have calculated mass transfer and diffusion coefficients in Nafion in this way; under steady state conditions water-sorption isotherms have been derived [72-74].

Futerko [60] developed a model to calculate the absorption of water derived from the Flory-Huggins thermodynamic model. His analysis was focused on differentiating the water uptake from liquid and vapour, and found this difference to be correlated with the structure of the polymer. Krtil et al. [75] defined vapour transport from inside to outside the ion clusters as the dominating mechanism for thinner membranes. In membranes thicker than 10 μm, the dominating mechanism of transport was described as conventional Fickian diffusion.

Choi et al. [76] applied the thermodynamic analysis from Flory-Hugins theory and coupled it with Freger's elastic model to account for the swelling effects caused by vapour sorption. They found a correlation between sorption and the elastic deformation and acid concentration variation during swelling.

A recent model claimed a mechanism for water in Nafion [77] that contradicts Fick's law of diffusion. The model fitted to experimental vapour sorption and desorption data assumed two-stage transport mechanism, where polymer swelling and relaxation became the rate limiting process during the water uptake, i.e., when the concentration gradient became negligible.

2.3.5 Transport through the membrane's bulk and interfaces: diffusion, and sorption

Ge and collaborators [78] described a water transport model for a fuel cell that set the basis for a novel analysis of water transport in Nafion within an electrode-membrane assembly. The model comprises the transport of water inside the bulk of the membrane and transport in and out through the membrane-electrode interfaces. The bulk transport was defined as Fickian diffusion; and the surface mechanisms, as absorption and desorption. Results from this analysis demonstrated that absorption of vapour water is slower than desorption across the membrane-electrode interface.

Majztrik et al. [62] reported an analysis based on the three-step-mechanism transport model proposed by Ge. The authors faced the challenge to decouple the individual contributions from surface and bulk mechanisms due to the nature of the steady state permeation experiments. The authors assumed a constant flux within and

across the membrane bulk and interface. The result provided an estimation of effective interfacial mass transport coefficients and a coupled component for diffusion and water concentration in the membrane, $c_{max}D$, which the authors could not deconvolute into individual values for the diffusivity coefficient, D, and the water concentration in the membrane, c_{max}.

2.4 Experimental determination of Mass Transfer coefficients

Several experimental methods have been used to quantify bulk and interfacial properties. The techniques will be discussed below.

2.4.1. Diffusion coefficient

Through gravimetric water uptake measurements, Yeo and Eisenberg [79] defined the temperature dependence for diffusion coefficient based on water sorption measurements. After this effort, advances in the experimental techniques for the calculation of the water diffusivity in Nafion have progressed until the use of state of the art methodologies (NMR, FTIR, etc).

The use of isotopes to determine the diffusion coefficient is common in liquid-equilibrated membranes. Zelsmann et al. [80] proposed a procedure to determine water diffusivity through the use of isotopes in the vapor state with Far IR Spectroscopy. The value of the diffusion coefficient averaged 1.5×10^{-10} $m^2 s^{-1}$ with this technique.

The self-diffusion coefficient of water through partially hydrated membranes has been characterized in detail through Nuclear Magnetic Resonance (NMR). The technique

works by means of correlating the ^{1}H interdiffusion with the intra-(or self-) diffusion coefficient of water [29]. Later, the same research group lead by Gottesfeld [29], reported experiments for a fully hydrated Nafion 117 membrane, combining imaging sequence with pulsed–field-gradient-spin-echo (PFGSE) NMR technique. The value of the self-diffusion coefficient found at 25°C was 5.5 and 7.5 $x10^{-10}$ m^2s^{-1}, for vapour- and liquid-equilibrated Nafion, respectively.

The use of the PFSGE NMR technique has been traditionally used to study diffusion and flow in porous media. The way the self-diffusion coefficient is determined reflects the molecular diffusion of a solute, in this case water, in a solvent media of the same composition, which is not the case of water in Nafion membrane. Thus, the term self-diffusion is not appropriate for water diffusion measured in Nafion.

Independently of the misleading terminology, PFSGE NMR, has characterized the diffusivity of water in the absence of activity gradients. As a consequence, these results are not fully applicable to situations with large gradients such as those found in a working fuel cell under current load. The variability of the diffusion coefficient from different techniques is illustrated in the graph of Figure 2.4, as reported by Motupally and collaborators [19]. The common finding in these results is the dependence on water content for the diffusion coefficient.

From Figure 2.4, Zawodzinski's results [29] from NMR studies showed the diffusion coefficient as function of the water content with a maximum, after which it decreased at higher hydration. In Fuller's experimental analysis [81], a linear correspondence between the diffusion coefficient and the membrane water content was reported. Nguyen reported similar results with a linear dependency on water content [82].

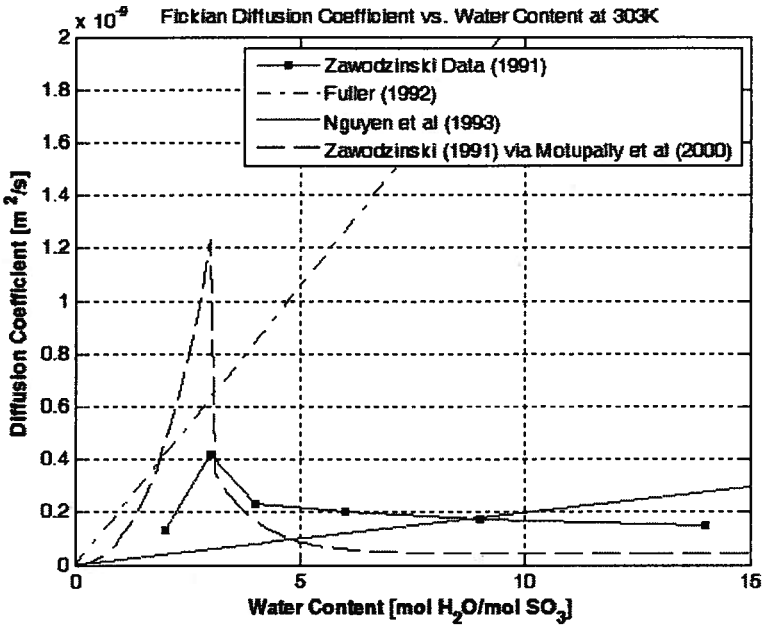

Figure 2.4: Diffusion Coefficient as a function of membrane water content. Adapted from Motupally et al. [19]

In spite of the variability of self diffusion coefficients results, and the questions about their applicability to fuel cell membranes, Motupally and collaborators [19] found self diffusion coefficients from experimental water permeation fluxes in a fuel cell that agreed with the results from Zawodzinski's NMR. The authors used activity gradients controlled by the gas flow rate and pressure in the fuel cell to associate the crossover flux and the driving force.

Ge et al. [78] used activity gradients to gain insight on the interfacial resistance to water transport. Their work incorporated three associated mechanisms in the overall transport process: absorption and desorption at gas/membrane interfaces, and diffusion of water in the polymer. The diffusion coefficient found from the analysis of water permeation was described as water content dependant with a maximum value of 8 $x10^{-10}$ and 11.5 $x10^{-10}$ m^2s^{-1}, at 323 and 353 K, respectively.

Apparent diffusion coefficients have been reported from vapour sorption experiments [74]. Result from desorption data generated a value of 2.6 x 10^{-12} m^2s^{-1} compared to 7.7 x 10^{-13} m^2s^{-1} from sorption data. The difference comes from an observed faster desorption rate through Fickian analysis. The authors concluded that sorption kinetic information could not provide reliable diffusion coefficients due to the coupling of mass transport with boundary layer effects and non-isothermal conditions in the membrane.

To address these limitations, Rivin et al. proposed steady state permeation coupled to solubility measurements to define effective diffusion coefficients, D_{eff}, that increased monotonically with water concentration. Values for D_{eff} ranged from 0.126 to 2.35 x 10^{-10} m^2s^{-1} from 0.2 to 1 activity gradient, correspondingly; and 3.07 x10^{-10} m^2s^{-1} for membranes equilibrated with liquid water.

Table 2.1 summarizes results from diffusion coefficient values obtained from the methodologies described above.

Table 2.1. Diffusion coefficients, experimental techniques

Nafion Type	Technique	Diffusion Coefficient 10^{10} m^2 s^{-1}	Conditions	Reference
1155	Water Uptake	2.1	30°C λ=22	1977, Yeo and Eisenberg [79]
117	NMR	0.6-5.5	30°C λ=2-14	1991, Zawodzinski et al. [29]
117	NMR	7.5	30°C λ=22	1993, Zawodzinski et al. [11]
117	Steady State Permeation	1.4-9.8	25°C λ=2-14	1992, Fuller [81]
117	Tritium Tagged Water	1.8-2.2	27°C	2006, Suresh et al. [83]
	Vapour Sorption	0.026-0.07	Desorption-sorption	2006, Rivin et al. [74]
112,115,117	Steady State Permeation + Solubility	0.13-3.1	λ=2-22	2006, Rivin et al. [74]

Results in Table 2.1, show a wide range of values for the diffusivity coefficient in Nafion membranes at temperatures below 30°C. The dependency on water content is observed for NMR and Steady State Permeation; however, this dependency varies from linear to non-linear, as shown in Figure 2.4.

Because each technique studies the water diffusivity under a different driving force schema, the results are not comparable. NMR applies no activity gradient to the membrane. The water uptake and vapour sorption gravimetric measurements provide a homogenous water environment, where there is no activity gradient. It has been discussed above that in the gravimetric techniques; it is the polymeric elastic force the acting limit mechanism for water transport. Contrarily, permeability measurements apply an activity gradient across the membrane acting as the main driving force for the water transport through the membrane bulk and interfaces.

2.4.2 Interfacial mass transport coefficients

Progress in fuel cell modeling relies on transport parameters to simulate the mass transport mechanisms at the membrane surface. Fuel cell literature shows little sensible physical information on water transport across the interface.

The importance of the mass transfer across the gas-membrane interface has been addressed before [11,74]; ever since, interfacial mass transfer coefficients in Nafion have started to appear in analyses of water transport. However, due to the novelty of this idea, these interfacial coefficients are less well represented in the literature than diffusion coefficients.

From the mechanism-in-series for water transport model, first described by Ge et al. [78], mass transfer coefficients of water were reported for a membrane-electrode assembly. The authors described the transport processes at the interfaces as absorption and desorption. The model described the interfacial transport dependency on the activation energy proposed by Yeo and Swee[79], it assumed a water volume fraction in the membrane. The coefficients showed values in the range of 10^{-3} cms^{-1}. The analysis showed water content dependency for the interfacial mass transfer coefficients for VE and LE membranes.

Most fuel cell models rely on experimental data to fit parameters by trial and error [84-86]. A common approach is to define a boundary condition for the flux based on Henry's law:

$$J_{boundary} = k_{\text{int}} c \tag{2.9}$$

from where an iterative solution is commonly applied to identify the interfacial mass transfer coefficient, k_{int} [62,68,77].

In order to relate the water concentration in the membrane with the water content in the gas, the use of equilibrium isotherms has been proposed.[68]. Following similar procedures, modelers have reported on water transfer coefficients within the range of 0.1 to 10 $x10^{-3}$ cms^{-1}. However, the application of Henry's law to describe equilibrium at the gas-membrane interface is flawed for systems where a kinetic process is present across the membrane surface.

From permeability measurements on Nafion membranes, a recent analysis presented by Majzstrik and collaborators [62] attempted to describe mass transport coefficients for the surface and bulk water transport. The authors reported a water flux,

which they called "effective transport coefficient", that in effect is nothing more than a fudge factor. The analysis is incorrect, as the authors defined the flux at the boundary using Henry's law (Equation 2.10), assuming incorrectly equilibrium across the membrane-gas interface. Futerko and Sing [60] also reported on an effective interfacial transport coefficient that was the result of fitting water flux values into a PEMFC water transport model.

Satterfield et al. [77] reported interfacial mass transport coefficients from vapour uptake measurements. The authors described a boundary flux from a variation of Henry's law where the transport phenomena at the interface and in the bulk were related by:

$$D\frac{\partial c}{\partial x} = k_{\text{int}}\left(c_{\max} - c\right) \tag{2.10}$$

The limitation of their model lies in the neglected interaction between the membrane and the surrounding vapour pressure. The model failed to include the possibility of water accumulation in the gas.

Table 2.2 summarizes the most relevant reports on interfacial mass transfer coefficients.

The wide variability in the reported values for the interfacial mass transfer coefficients is evident in Table 2.2. Comparison between these results is not duable because of the different assumptions each approach made. The results from Berg et al. and Okada et al. correspond to the fit between mathematical models with experimental data from full fuel cell testing. Therefore, the whole membrane-electrode-assembly system adds complexity and contributes with two more boundary resistances to water transport from the membrane-catalyst, catalyst-gas diffusion layer, and gas diffusion layer- gas interfaces. In the case of Satterfield and Benziger, the main flaw of their

mathematical model is the assumed equilibrium between the membrane and the humidity of the adjacent gas. The possible kinetic or convective process across the membrane surface created by the gas was not considered in the analysis.

Table 2.2. Summary of relevant interfacial mass transfer coefficient reported values.

Authors	Interfacial Mass transfer coefficient $x10^3$ cms^{-1}	Technique
Berg et al.	0.57 (80°C)	Fit between experiments and water transport model of a fuel cell
Okada et al.	1 (50-80°C)	
Ge et al.	sorption: 0.1– 0.8 @ λ=1-9 desorption: 0.45-3.25 @ λ=1-9	Permeability measurement in MEAs
Satterfield and Benziger	2.8 (Nafion 112) 10.2 (Nafion 115) 10.6 (Nafion 1110) 7.6 (Nafion 1123)	Gravimetric measurements from vapour uptake

A complete physical and mathematical representation of the membrane boundary conditions typical to fuel cells is not available in the literature. Most experimental methods simulate equilibrium conditions, instead of representing the dynamics across the membrane surface. Even more, when the experimental techniques achieve to reproduce the typical conditions within a PEMFC, the mathematical models were not able to address the boundary process due to the membrane-flowing gas interaction.

Table 2.3 shows the summary of the most relevant experimental techniques that have addressed the study of water transport phenomena in proton exchange membranes. Those analyses show the advance on the phenomenological understanding of the mass

transport across Nafion membranes. As shown, gravimetric techniques for vapour and liquid uptake have dominated the research of water transport across Nafion membranes. Even though these techniques offered a partial solution to the objective of this thesis research; they were not chosen as the primary research tool because the transport mechanisms occurring during water uptake are not representative of the ones driven by activity gradients. Water sorption experiments involve a well-mixed medium that entirely surrounds the membrane.

In the last two years, new approaches have emerged to incorporate imaging techniques in the identification of water content profiles across the MEA in functional fuel cells. The images analysis from Magnetic Resonance Imaging (MRI) [110, 111], for example, have provided information on the localization of water accumulation and dehydration inside the membrane. However, due to the early stages of these techniques, further improvement in the corresponding phenomenological models are required to extend the comprehension of water transport mechanisms across the membrane. Therefore, in this work, water content distribution imaging techniques were not discussed in extent.

Table 2. 3 .Summary of the most relevant experimental approaches related to this thesis

Technique	Liquid	Vapour Driving Force	Transient	Steady State	Model	Remarks
Sorption Gravimetry Yeo and Eisenberg, 1977[45]		•	•			Measured water uptake in Nafion in long time experiments. Obtained Diffusion Coefficient $D=f(T)$, and Activation Energy.
Water immersion Gravimetry Takamatsu et al.. 1979	•		•			Measured water uptake. Obtained Apparent Diffusion Coefficients. Long time experiment
NMR Spectroscopy Zawodzinski et al 1993 [54]	•				•	Obtained Self Diffusion Coefficients as function of water content for Nafion.
Water transport Motupally et al. 2000 [48]	•	•		•	•	Measured Permeability Flux. Found Fickian Diffusivity in MEAs
Quartz-Microbalance Sorption Gravimetry Ktril et al. 2001[40]		•	•	•	•	Measured Sorption, Desorption Rate. Obtained Diffusion Coefficient from transients and Vapour Isotherms from steady state data for Nafion.
Vapour sorption Rivin et al. 2001 [39]		•	•	•		Measured Boundary Layer Resistances. Obtained Effective Diffusivity and Sorption Isotherms in Nafion.
Water transport Rivin et al. 2001 [39]		•	•	•		Measured Permeability Rate. Calculated Nominal Diffusivity in Nafion as nominal concentration was used.
Water transport Ge et al. 2005[43]	•	•	•	•	•	Measured Permeability Flux. Obtained Fickian Diffusivity, Absorption, and Desorption Mass Transfer Coefficients in MEA with microporous layer in an active PEMFC
Hydrogen pumping cell Ye and Wang 2007 [6]		•	•		•	Measured Water Concentration Profile in long time experiments. Calculated Fickian Diffusion Coefficient in a Fuel Cell.
Water transport Majsztrik et al. 2007[27]	•	•	•		•	Measured Permeability Flux. Found Bulk effective diffusivity: $C_w D$, and Effective mass transfer coefficient at gas/membrane interface. C_w and D were not individually calculated.
Vapour Sorption Majsztrik et al. 2007[27], Satterfield et al. 2008[42]		•	•		•	Measured water uptake. Found interfacial mass transfer coefficient in Nafion
Water Transport Romero. 2008 (this work)	•	•	•	•	•	Measured Permeability Flux in short time experiments. Calculated interfacial mass transfer rates, k_i, and individual values for Diffusivity coefficient, D, and water concentration C_w in Nafion. Characterized water transport for composite/Nafion membranes.

2.4.3 Aims of this research

Prior to this research, in-situ (fuel cell) water balance techniques were considered a viable way to identify the effects of the driving forces created by operational conditions, i.e., gas flow, temperature, pressure, and humidity. Nevertheless, the disadvantage of such approach was the added complexity of boundary effects from the membrane-catalyst layer, catalyst-gas diffusion layer, and gas diffusion layer-gas, each one representing a complete independent system. Instead, the interest for this research lies on a more fundamental characterization of water transport in the membrane bulk and membrane-gas interface.

In order to distinguish the mechanisms of water transport across the bulk and the interfaces of Nafion membranes, the interest focused on observing the effects of activity gradients as the main water transport driving force. A total resistance to the main water transport processes in Nafion was proposed by means of a resistance in series analogy, as illustrated in Equation 2.11. This equation describes the sum of the resistances to interfacial sorption and bulk diffusion:

$$\sum \text{resistances} = \frac{1}{k_a} + \frac{1}{k_d} + \frac{d}{D}, \tag{2.11}$$

where the transport rate at the interfaces, for sorption and desorption, and in the bulk (of thickness d) are described by k_a, k_d, and D, correspondingly.

The experimental interest was to isolate the mechanisms that dominate the transport in a passive membrane, where the mechanisms of proton mobility and water generation were negligible. For this purpose, a new experimental design was required to allow the incorporation of operational conditions common to fuel cell systems. A new water

transport testing rig and experimental protocols were proposed to accomplish this objective. The following chapter (Chapter 3) describes the proposed water transport experiment concept used to characterize PEMs.

It includes the experimental protocol for the steady state and transient measurements. It also includes the description of pre-established techniques to complete the analysis of water transport in Nafion and composite-Nafion membranes.

3. Experimental Methods

This chapter describes the methodologies to characterize water transport in Nafion membranes. Section 3.1 addresses sample preparation for Nafion and composite-Nafion membranes. Sections 3.2 and 3.3 are focused on the water transport experimental concept, design of the permeability cell, and experimental protocols for steady state and transient measurements are addressed in section 3.4.

The second part of this chapter centers on the description of pre-established techniques for the investigation of membrane properties related to water transport. The procedures for water content, differential scanning calorimetry, and dynamic vapour sorption techniques are described in sections 3.5.1 to 3.5.3.

3.1 Membrane Preparation

3.1.1 Membrane activation

Nafion membranes fabricated by Dupont® were used for all experiments. The series of Nafion 112, 115 and 117 membrane was chosen in order to keep the same Equivalent Weight (1100 g dry Nafion/mol SO_3^-) and to be able to vary the thickness from: 51 to 127 to 183 μm, correspondingly (measured at 23°C and 50% RH).

Prior to all experiments, the membranes were chemically pretreated by full immersion in 3 wt% H_2O_2 aqueous solution (at 80°C) for 2 hours, followed by repeated rinsing in de-ionized Milli-Q water (Millipore) at room temperature, immersion in 1.0 M

H_2SO_4 (aq) for another 2 hours (at 80°C), and finally repeated rinsing in de-ionized Milli-Q water (Millipore) at room temperature. The membranes were stored in de-ionized water for at least 24 hours to ensure full hydration. Prior to the assembly into the gated cell, the membranes were pat-dried with tissue paper to remove the excess water taking care that the membrane was not pressed to avoid excessive dehydration. For each experiment, the membrane was exchanged to start with a fresh membrane.

3.1.2 Nafion 115- silicon dioxide composite membranes

In order to modify the water content of Nafion membranes, we used Nafion 115 membranes doped with SiO_2 nanoparticles. The membranes were supplied by the MEA group in NRC-IFCI. The membranes were prepared by the sol-gel method as reported in [45]. The weight content of SiO_2 was controlled by immersion time in tetraethylorthosilicate solution to produce samples with 10, 16 and 33 wt% of silicon dioxide (SiO_2) nanoparticles. Reports suggest that the sol-gel reactions in Nafion occur in the polar clusters inside the membrane generating SiO_2 nanoparticles which fill in the clusters associated to the ionic SO_3^- sites [49]. X-ray analysis showed a homogeneous distribution of the silica nanoparticles across and along the membrane samples [45].

After the sol-gel preparation, the membranes were chemically pretreated as described in 3.1.1, and stored with de-ionized water. Prior to the analysis, smaller area samples were cut off from the originally prepared membranes.

The hygroscopic properties of silica increased the water uptake capacity of the membrane [45,87]. The Equivalent Weight of the composite membranes changed due to the incorporation of the SiO_2 as described in Equation (3.1):

$$EW_{N115/SiO_2} = EW_{N115} + \left(EW_{N115} \frac{SiO_2\ wt\%}{100} \right) \quad (3.1)$$

A summary of the membrane properties changes as a function of the SiO_2 wt% content is presented in Table 3.1.

Table 3.1. Properties of Nafion 115/SiO_2 composite membranes [45]

SiO_2 wt %	Dry Membrane Thickness, mm [45]	Liquid equilibrated Membrane[b] Thickness Gain, % [45]	This work	Equivalent Weight [c] g dry membrane/mol SO_3^-
0[a]	0.132	14	16	1100.0
10	0.15	12	11	1222.5
16	0.142	8.9	15	1310.6
33	0.171	8	13	1642.0

[a] Pure Nafion 115, [b] under 25 °C, [c] from Eqn. (3.1)

3.2 Water Transport Experimental Concept

The water transport experiments in Nafion membranes required a cell design that allowed the membrane to be compressed between two environments with independent temperature, pressure and humidity control. The thin membrane (~ 50 to 180μm) required high-quality sealing in order to achieve total separation of the environments. Figure 3.1 illustrates the experimental concept.

The setup comprises a two compartment-cell where either liquid or vapour would provide the water supply on one side of the membrane, and a dry gas to evaporate the water from the membrane surface on the other side. Figures 3.1 show a schematic cross-section of the design setup: a Nafion membrane sample placed in a circular holder to create two cylindrical chambers: wet and dry. Figure 3.1a shows the liquid equilibrated

(LE) experiment setup, the membrane separated liquid water at temperature T_1 from the dry chamber at temperature T_2. For the vapour-equilibrated (VE) membrane experiments (Fig.3.1b), the Nafion sample is kept in contact with a constant volume of fully saturated air on the wet side of the cell (the conditions on the wet and dry sides were identified with the subscripts 1 and 2, respectively).

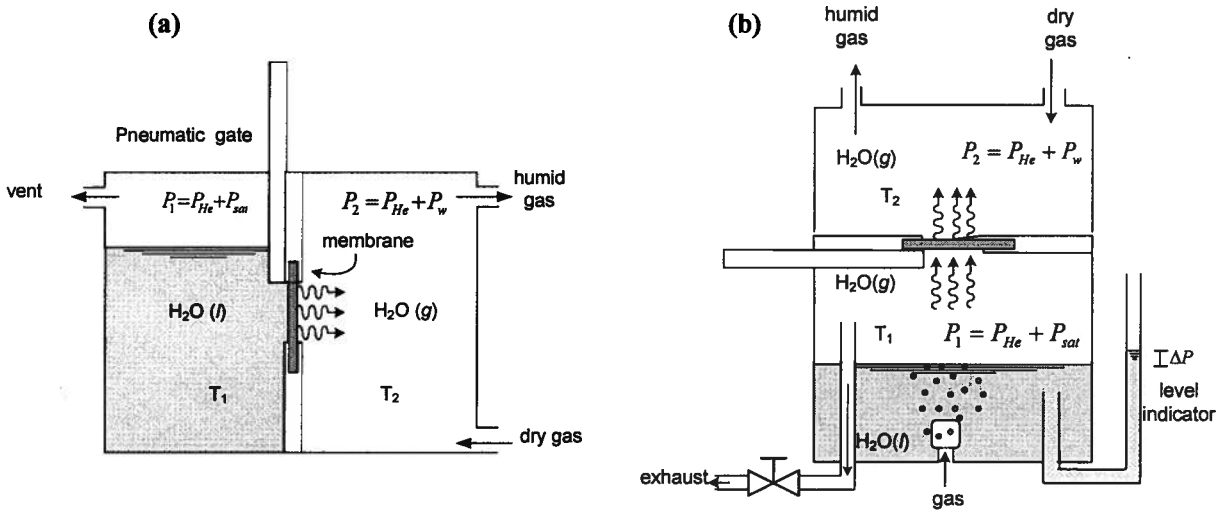

Figure 3.1. Setup for water transport experiments: (a) liquid equilibrated membrane; (b) vapour equilibrated membrane.

The original feature of the permeability cell design is the gate valve that allows isolation of the membrane from the wet environment (Figure 3.2a). This gate valve allowed the reproducibility of transient water transport measurements. During measurements, the gate valve is maintained open (Figure 3.2b), so equilibrium between the stagnant fluid (wet) and the membrane is maintained.

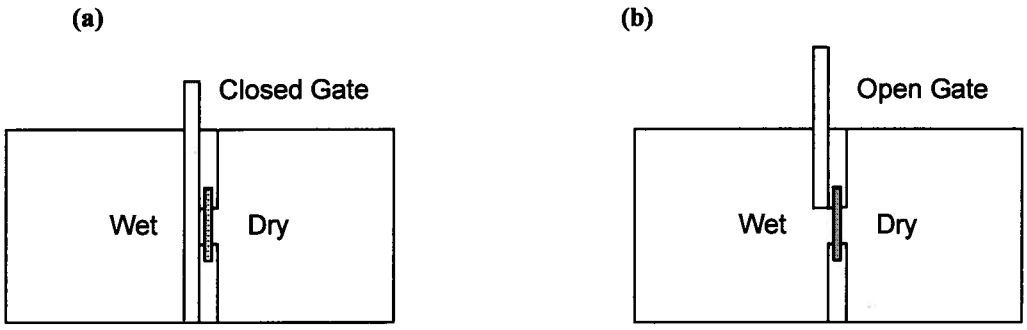

Figure 3.2. The gate valve is pneumatically controlled to connect/disconnect the membrane with the wet chamber. (a) closed-gate configuration, (b) open-gate configuration.

Unlike typical transient gravimetric measurements [74,77,82], our experiments generated known boundary conditions on both sides of the membrane by controlling the gas flow rate on one surface, and keeping a stagnant volume of liquid or vapour water on the other side of the membrane. In this way, the boundary layer resistance can be neglected on the wet side. The mixing between the gas and the water vapour, promoted by the gas stream, also reduces the possibility of a boundary layer resistance on the dry membrane surface.

3.3 Permeability Cell

In order to control temperature, pressure and humidity in both chambers, the permeability cell had to accommodate temperature, and humidity sensors; as well as gas and water supply, and exhaust lines. Finally, a fast and easy assembly was an important design factor in order to improve testing time during sample exchanges.

In several attempts the designed cells' prototypes presented challenges to align and seal the membrane sample within the cell, and the procedure took longer than 30

minutes. The final design achieved all previous requirements, and included a novel feature to control the initial time of the measurement, through a gated-valve.

Figure 3.3 shows the cell including details on the sensor positions and the cell components: dry and wet chambers, water jackets, membrane holder, and gated valve. The figure includes connections to the water baths that controlled the temperatures around the environmental chambers (T_1 and T_2).

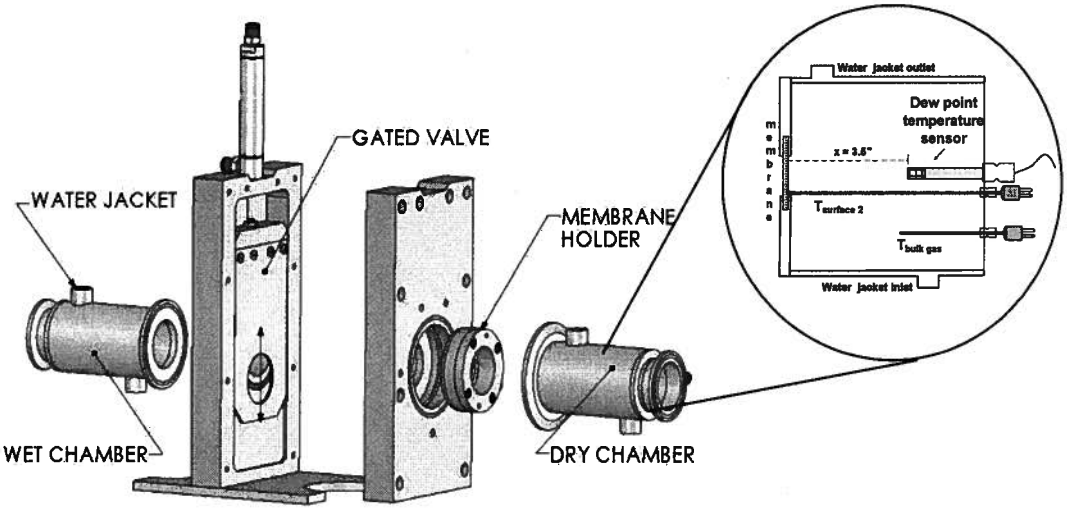

Figure 3.3. The wet and dry chambers were separated by a membrane holder. The inset shows an enlarged schematic of the dry chamber (including sensor locations).

The dry chamber manifold was designed in such a way that the gas flow rate at the inlet is withdrawn at the same velocity from the cell. When the gas enters the cell, it is directed to the wall where it is splits and mixes quickly. The larger the flow rates, the more enhanced is the stirring, and then gas to gas diffusion can be neglected [88]. Figure 3.4 outlines the distribution of the inlet, outlet ports and sensors in the dry chamber.

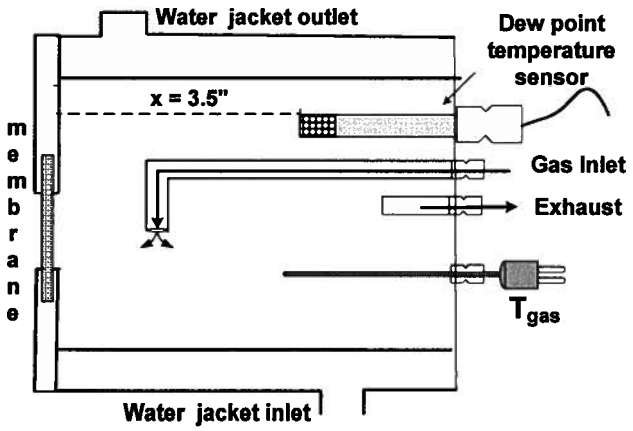

Figure 3.4. Schematic distribution of the gas manifolds and sensors in the dry cell.

The dew point sensor measures an averaged temperature as result of the enhanced mixing in the chamber. Because the nozzles of the inlet and exhaust are small compared to the membrane area and are oriented far away from each other, good mixing is ensured. In order to prevent formation of steady convective flows, the vents are orientated away from the membrane. Reynolds number calculations confirmed the absence of turbulent flows (See Appendix A). The assumption of good mixing is based on the fast gas diffusivity known in vapour water; however, further physical evidence to probe this assumption right is required.

The cylindrical chambers with total volumes of approximately 125 cm^3 were separated by 2 cm^2 of exposed membrane on either side. The stainless steel chambers had a double wall to circulate hot water. The final cell design was manufactured by Tandem Technologies Ltd. Technical specifications are included in Appendix B. The photos in Figure 3.5 show the cell from an isometric view (left), and the cells's main body with the membrane holder in place (right).

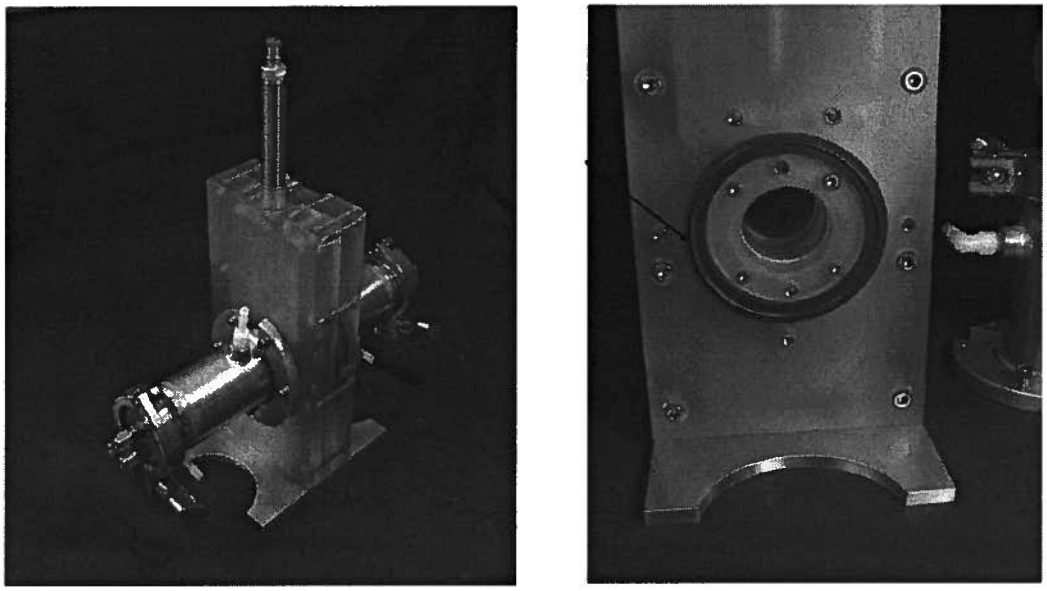

Figure 3.5. Top isometric view of the permeability cell (left); (right) dry chamber disconnected from cell's body to assemble the membrane.

Placement of the membrane into the sample holder first and then into the cell's body is shown in Figures 3.6. A wet membrane (pat-dried) is first assembled between two flat silicon seals (of thickness 1.55 mm) cut to the same size as the internal diameter of the holder. The holder is tightened up with four bolts with equal torque to seal the membrane evenly and to prevent leaks (Figure 3.6a).

In Figure 3.6b, the gated valve is closed during insertion of the sample holder into the cell's body, which prevents contact between the membrane and the wet chamber, previously filled with water. The speed of the sample assembly was reduced to a total of 2-5 minutes.

(a) (b)

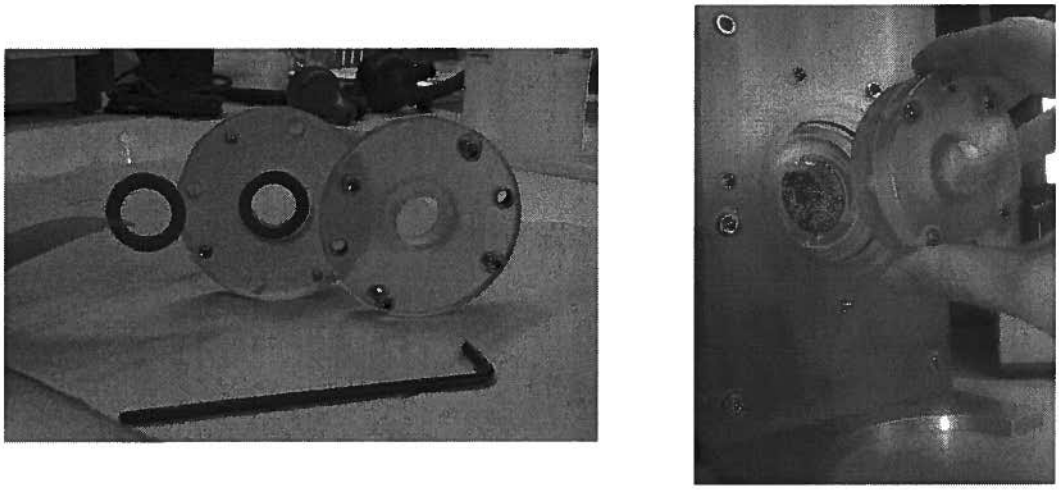

Figure 3.6. Membrane assembly process: (a) the wet membrane and silicon gaskets are placed into the sample holder; (b) the sample holder is placed into the water transport cell. The gate, made of acrylic is closed in the picture to restrict the water to the wet chamber during the assembly.

3.3.1. Experimental set up, instruments and sensors

For all water transport measurements, we used the permeability cell within the experimental setup illustrated in Figure 3.7. Mass Flow Controllers (Alicat®, 0-500 sccm, ±0.4% of reading + 0.2% of full scale) supplied nitrogen, and helium gas to the cell. When higher flow rates were required, the MFCs were connected in parallel arrays to supply up to 1000 STP cm^3min^{-1}. Nitrogen was used for vapour equilibrated experiments to enhance water vaporization by bubbling gas into a water volume inside the wet chamber. In the dry chamber, helium was invariably used as the carrier gas due to its light molecular weight which enhances mixing in the chamber, reducing the flight time to reach the sensor. Two water baths (Haake®, 230VAC, 50Hz, 5L) circulated hot water through the cell's water jackets. For the bath operation, we used the temperature provided by the thermocouple readings inside the cell chambers.

Fine wire K-type thermocouples (Omega® 5TC-TT-K-30-36, ±1 °C or 0.4% of reading value) and pressure transducers (Omega® PX105-015G5V, 0-15 psig) were used to monitor temperature and pressure within the chambers. The relative humidity was monitored via dew point temperature measurements with a composite, thermally-controlled probe that prevented condensation (Vaisala® HMT 330, ±1% RH from 0 to 90% RH, and ±1.7% RH from 90 to 100% RH) [89].

The dew point temperature sensor was cross-referenced with an RGA–Mass Spectrometer (Hiden™ HPR-20) to quantify the vapour pressure of saturated gas. Appendix C shows the experimental set up for calibration of the dew point sensor and results.

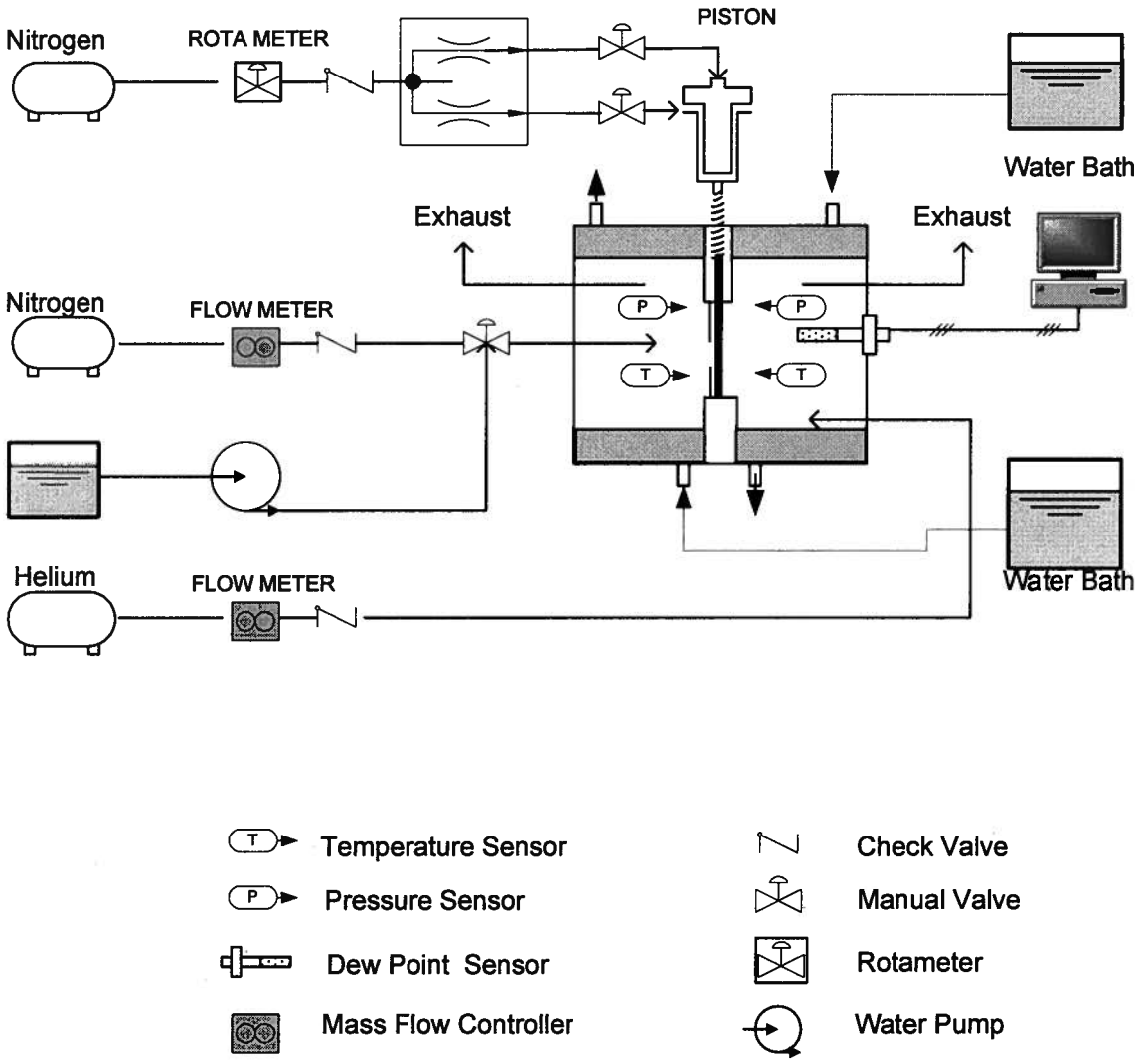

Figure 3.7 Complete experimental setup for water transport measurements. The permeability cell is monitored for temperature in both chambers; and pressure and dew point in the dry side chamber. The gate's activation mechanism and the temperature control systems are included.

3.3.2 Thermal effects

A possible source of error to consider in the data analysis is the heat flux due to the enthalpy of evaporation and condensation from and into the membrane. In order to quantify the error from neglecting the energy balance, the temperature drop across the membrane was calculated from the maximum water flux across the membrane, J (Calculation of the water flux is described in Section 3.4.1), and the vaporization enthalpy of water ($\Delta H^{vap} = 36.78$ kJ/mol [90]):

$$q = J\ \Delta H^{vap} \tag{3.2}$$

Using Fourier's law:

$$q = -k\nabla T = -k\frac{\Delta T}{L}, \tag{3.3}$$

the largest temperature change across the membrane is found by:

$$\Delta T \approx -\frac{L \cdot J \cdot \Delta H^{vap}}{k}, \tag{3.4}$$

where k corresponds to the thermal conductivity of Nafion in the limiting dry condition (0.13 W/mK, for Nafion at 50°C and 0%RH[91]), and L is the maximum membrane thickness tested (183 μm).

The analysis result showed a maximum temperature drop of 5°C for the LE, and 2.6°C for the VE. Thus, neglecting the energy balance can result in an estimated ± 23% error in temperature activated processes, according to an Arrhenius dependency.

In an attempt to corroborate the temperature drop across the membrane, thermocouples were placed on the wet and dry surface of the membrane. For these measurements, the wet chamber was filled up with liquid or vapour, accordingly. For LE, the membrane temperature showed zero gradient across the thickness of the membrane; for VE, the membrane showed a drop of 1 °C in the dry side. Care was taken to ensure the thermocouples' tips were in direct contact with the membrane surface; even so, further temperature measurements are needed to map out the membrane surface temperature with higher control of embedding the sensor tips on the surface without perforating the sample. For the cell's accurate temperature control, a thermocouple placed close to the membrane's surface was used to regulate the temperature of the water baths.

Independent temperature measurements showed that the temperature variation within the dry chamber could be considered negligible; the temperature distribution was measured along the horizontal axis inside the centre of the dry chamber. For these measurements, the gate was kept closed and hot water supply was maintained constant through the jacketed wall of both chambers. Four thermocouples were located along the horizontal axis and results showed a 1°C gradient from end to end of the dry chamber. However, in regular operating conditions, with the open gate and the corresponding flowing gas, the maximum temperature gradient along the horizontal axis was measured to be in ±0.1°C range, this improvement in the temperature homogeneity is due to the mixing effect of the drying gas, which accounts for a negligible temperature gradient inside the chamber. This was reproducible for the temperature range of 30-80°C.

3.3.3 Activity gradient

The drying effect of the varying gas flow rate over the membrane surface created a water concentration profile across its thickness. In this research, we adopted activity difference as the main driving force for water transport due to their natural occurrence in working PEM fuel cells.

Much has been reported on the response on water transport to different driving forces: pressure, chemical potential, and isotopic concentration gradients [65,66,70,92,93]. Under extreme working conditions, the water and heat management designs of fuel cells can not guarantee constant or full hydration for the membrane generating activity gradients that act as the main driving force for water transport across the membrane.

The activity difference across the thin membrane was calculated for water transport experiments according to:

$$\Delta a = a_{wet} - a_{dry} = a_1 - a_2, \tag{3.5}$$

where a conventional definition of water activity was adopted as reported in the context of fuel cells:

$$a = \begin{cases} 1, & \text{for liquid water vapor in fully saturated air} \\ \dfrac{P_{w,i}}{P^{sat}(T_i)}, & i = 1,2 \text{ for unsaturated air at temperature } T_i \end{cases} \tag{3.6}$$

This expression provides a normalized parameter for water activity on either side of the membrane, equivalent to the relative humidity in the gas phase next to the membrane surface[1].

Table 3.2 illustrates the effect of varying gas flow on the water activity calculated with Equation 3.6 for unsaturated air. These data correspond to a VE equilibrated Nafion 115 membrane at 30, 50, and 70°C.

Table 3.2. Illustrative example of the effect of varying the gas flow rate on the water activity

He gas flow $cm^3\ min^{-1}$ (STP)	Water Activity, $\frac{P_{w,i}}{P^{sat}(T_i)}$		
	30°C	50°C	70°C
50	0.50	0.35	0.36
100	0.20	0.22	0.23
300	0.08	0.09	0.09
500	0.05	0.05	0.055
700	0.04	0.03	0.04
1000	0.02	0.02	0.02

[1] In this work, inside the membrane and on its surfaces it is referred to the water concentration as water content, λ [=] mol H_2O /mol SO_3-, instead of water activity

3.4 Water Transport Experimental Protocols

The following sections (3.3.1 and 3.3.2) describe the proposed methodology applied to PFSA membranes for water transport measurements in steady state and transient regimes using the permeability cell.

3.4.1 Steady state water transport

Once the membrane was assembled and the wet chamber reached the desired temperature and humidity with the gate closed, a constant flow rate of dry helium was established in the dry chamber upon reaching a steady state. Our experimental protocol defined steady state as the state for which the cell temperature and the dew point temperature did not vary by more than ±0.01°C under a constant helium flow rate.

A small but detectable positive pressure was required to maintain the flow of helium gas. Typically, the pressure inside the chambers was less than 0.1% higher than the prevailing atmospheric pressure (i.e., ΔP in Figure 3.1 was between 10^{-4} and 10^{-3} atm).

The water vapour pressure was calculated from the dew point measurements via the relationships in Equation (3.7), and the empirical coefficients in Table 3.3 (provided by the sensor's manufacturer for the Vaisala® HMT 330) :

$$\ln P_w = \sum_{i=1}^{3} b_i \Theta^i + b_4 \ln \Theta \qquad (3.7)$$

Table 3.3. Coefficient values [89] for Vapour Pressure Equation (3.7):

$$\Theta = T - \sum_{i=0}^{3} C_i T^i$$

C_0	0.4931358	b_{-1}	-0.58002206x10^4
C_1	-0.46094296x10^{-2}	b_0	0.13914993x10^1
C_2	0.13746454x10^{-4}	b_1	-0.48640239x10^{-1}
C_3	-0.12743214x10^{-7}	b_2	0.41764768x10^{-4}
		b_3	-0.14452093x10^{-7}
		b_4	6.5459673

Figure 3.8 provides a sample data set to illustrate the results and data treatment in the steady state experimental series. The water vapour pressure in the dry chamber, P_2, was recorded at different temperatures and helium flow rates.

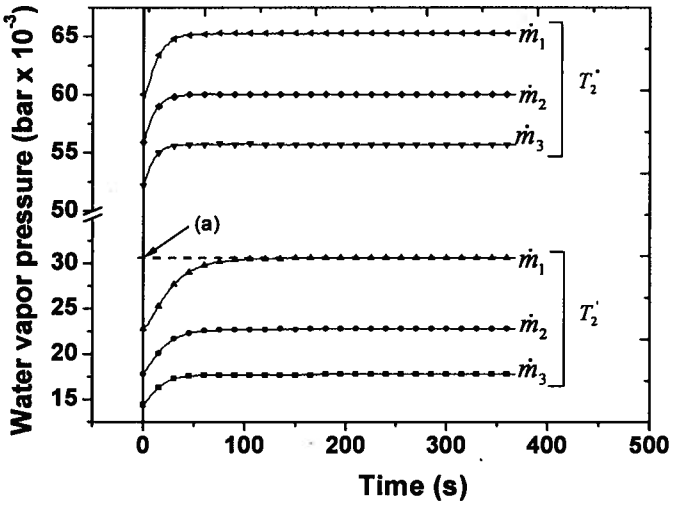

Figure 3.8. The vapour pressure was measured at different helium flows and temperatures. For each experiment, the steady state vapour pressure was extrapolated. For clarity, the symbols were plotted every 15 data points only. At steady state, the final value for P_2 was obtained from each curve as indicated by the arrow (a).

The steady state P_2 values were then plotted as a function of the associated flow rate. See Figure 3.9 for several data sets on vapour pressure under different temperatures. Each point in the graph represents one individual experiment.

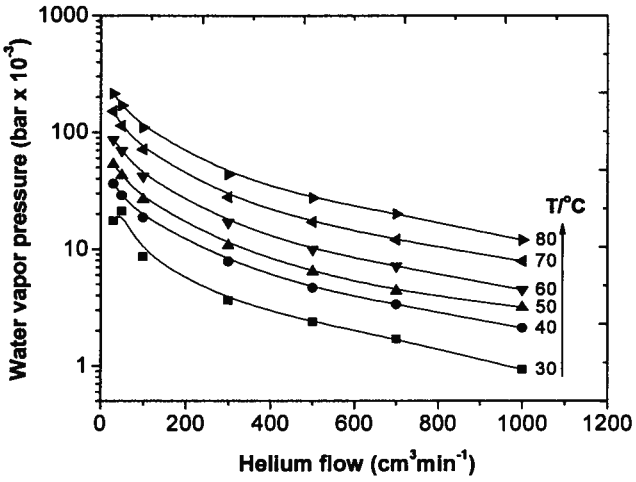

Figure 3.9. For each experiment, the steady state vapour pressure was obtained from the plateau and plotted as a function of helium flow rate.

To calculate the flux of water across the membrane, ideal gas behaviour, conservation of mass, and no water accumulation within the membrane (at steady state) was assumed. Using the corresponding helium flow rate and the molar fraction of water, x_2, which was derived from the vapour pressure data and total pressure ratio, the flux, J, was defined by:

$$J = \frac{1}{A}\left(\frac{X_2}{1-X_2}\right)\dot{n}_{He} \tag{3.8}$$

The details of this calculation are included in Appendix A.

The typical curve from steady state data is shown at different flow rates in Figure 3.10a. The graph shows the asymptotic flux increasing at higher flow rates corresponding

to a liquid equilibrated (LE) Nafion 117 membrane at 30, 50, and 70°C. Figure 3.11b, shows the data reproducibility from 3 experiments at each temperature. The flux data showed good reproducibility with maximum standard deviation of 0.003 and maximum standard error of ±0.001.

One of the findings during the experiments was the importance of keeping the membrane wet during sealing and assembling in the sample holder. In this way, the seal between the membrane and the gaskets is maintained firm while the exposed membrane area shrinks and expands due to humidity changes in the experiment. Yet, a source of data deviation that could not be avoided with the current setup was the humidity variation in the room air. The averaged vapour pressure from experiments carried out during days with environmental conditions within the average (i.e., 39% RH and 20°C), and the vapour pressure from days of extra humidity (63%RH, 20°C) showed up to 8.4 % difference in the data. A further improvement in the setup would be to isolate the experiment from the humidity of the room air.

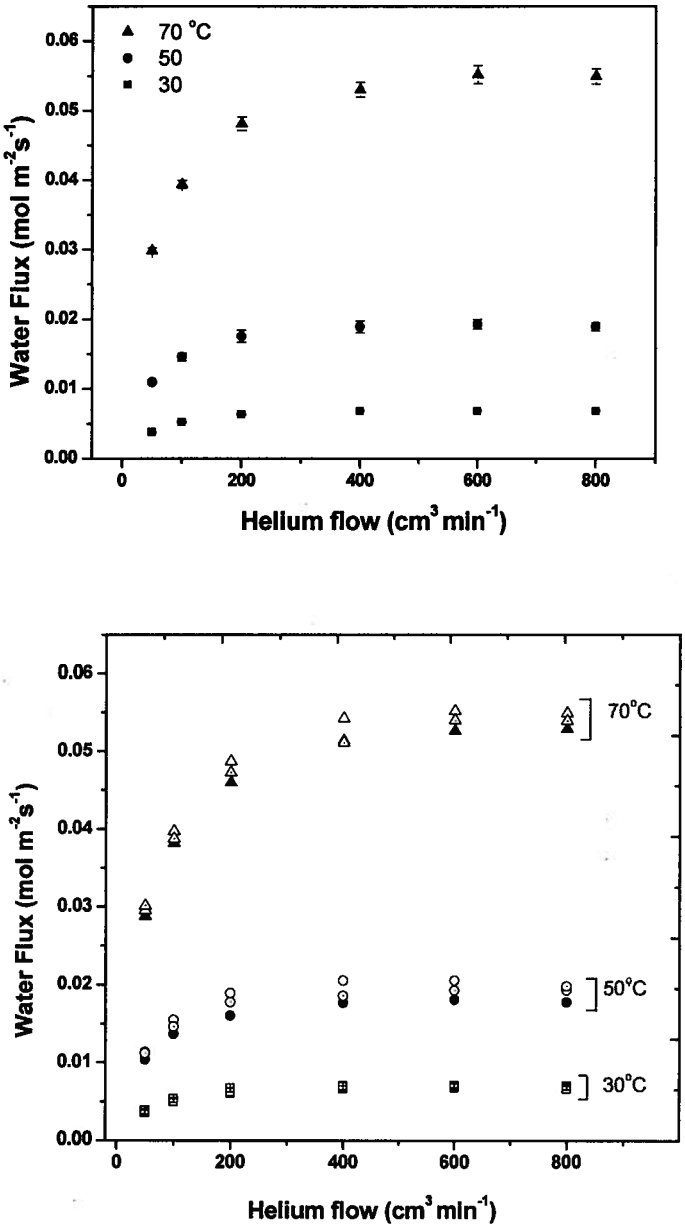

Figure 3.10. (a) Flux from steady state water transport for LE Nafion 117 at 30, 50 and 70°C. Error bars correspond to the standard error from three experiments in each point, as shown in (b).

3.4.2 Transient water transport

Transient measurements for Nafion 112 and 117 membranes were performed with liquid-gas equilibrated membranes at 30, 50, and 70°C and atmospheric pressure (1005 mbar monthly average) with the set up as described in Figure 3.7. A set of measurements for Nafion 112 and Nafion 117 under VE at 50°C were completed at atmospheric pressure for comparison reasons; analysis on VE membranes is required.

For transient measurements, the permeability cell provided high accuracy to control the initial measurement time through the sliding gated valve. The gated-valve, which separated the membrane from the wet chamber, was opened after the dry chamber had reached desired conditions of humidity and temperature.

The response time of current commercial humidity sensors limited our measurements time resolution to 1 second. The time response for our primary sensor: (Vaisala® HMT 330) was measured in the cell, after opening the gated valve to the wet chamber previously saturated with vapour. The measured response time was 1 second under dynamic conditions, i.e., for helium flow range 100-1000 cm^3min^{-1} (STP), and 30°C. Figure 3.11 shows the response time under static air and compares it with the response under dynamic conditions (above described). The sensor responded faster in the latter case due to the enhanced mixing from the flowing gas.

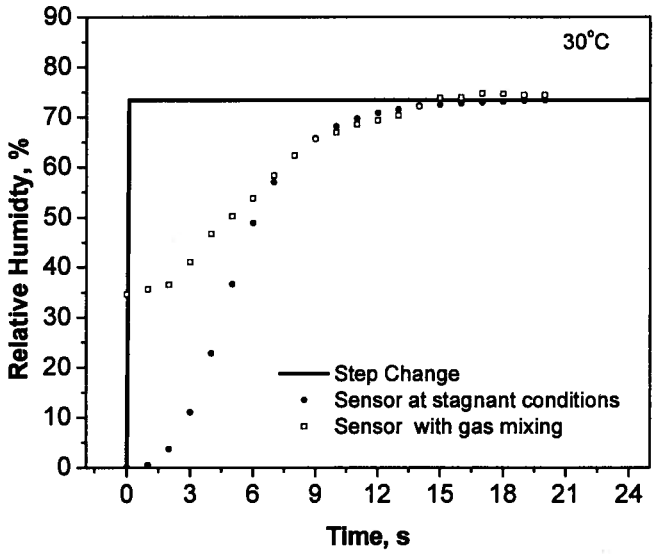

Figure 3.11 Measured time response to relative humidity step change from Vaisala® dew point sensor.

Prior to the experiment, the membrane pre-conditioning procedure followed was:

1) drying out the membrane at room temperature for 20 hours ,
2) assembling the membrane in the dry side of the cell with the gate valve closed (to keep the membrane surface away form the wet chamber),
3) dry helium was fed into the dry chamber at the desired temperature for 5 to 6 hours. The flow was varied each hour alternatively from 100 to 500 cm^3min^{-1} (STP) until the dew point temperature reached a minimum steady state.

In this way, the membrane's surface was driven to a dehydrated condition that was experimentally reproducible within a maximum dew point standard deviation of ±3°C at 30, 50 and 70°C. This deviation can be explained by the relative humidity of the environment. It is probable that the air humidity diffuses through the exhaust stream into the chamber because of a water concentration gradient between the environment and chamber.

For a different initial condition, the same method would apply, i.e.; for a semi-hydrated membrane, a humid gas flow could be fed to condition the membrane to a desired relative humidity value after dehydrating it for 20 hours.

When the dew point signal reached steady state, the pneumatically controlled gate valve was lifted, exposing the membrane to the wet environment and establishing a thermodynamic potential gradient to drive the water across. The time was measured until the dew point temperature reached a maximum and reached the final steady state. The dew point temperature was converted to vapour pressure and from it, the water flux was calculated to proceed with the data analysis.

The dew point temperature data were converted to water flux, in the same way as described by Equation 3.8, to facilitate the data analysis. From all transient experiments, we identified a characteristic transient signal for Nafion membranes with an *s*-shape curve, similar to the curve of sorption experiments [74]. Figure 3.12a shows the flux of water as a function of time. In all graphs, a kinetic response was identified between an initial and a final steady state. The initial steady state, represented by $t_{ss,\ \text{initial}}$, was recorded from the time when the gated valve was lifted (zero time) to the start of the flux rise. After the kinetics, the second steady state, $t_{ss,\ \text{final}}$, was recorded from zero time to the beginning of the second plateau. Both, $t_{ss,\text{initial}}$ and $t_{ss,\text{final}}$ are identified as the curve inflexions in the graph of Figure 3.12a. In Figure 3.12b a comparison of the transients for LE Nafion 117 membranes at 30, 50, and 70°C is shown.

(a)

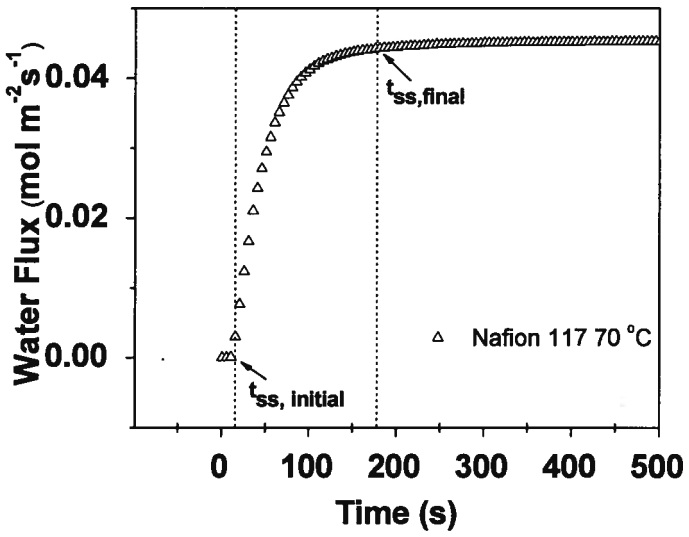

(b)

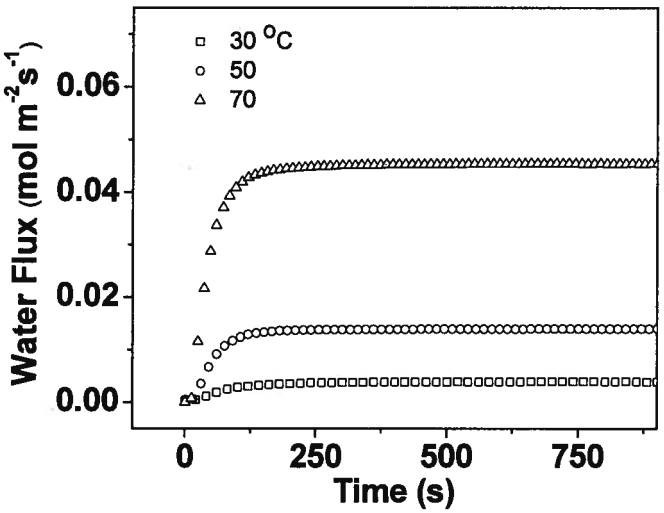

Figure 3.12. Typical transient water transport signal (a); transient curves for liquid equilibrated Nafion membranes at different temperatures (b).

3.5 Pre-established membrane characterization techniques

The following sections describe analytical techniques (i.e., water content, DSC, and DVS) applied to Nafion and SiO_2-Nafion membranes as part of the case study presented in Chapter 6.

3.5.1 Water content measurement

To obtain the mass of the wet membrane, the membrane samples were equilibrated in liquid water at room temperature for 24 hours. Before measurement, the excess water was pat-dried and the membrane was quickly weighted to calculate the sample water content at the beginning of the experiment.

The samples were driven to dehydration at 60°C and vacuumed overnight. The membrane's dry weight was measured to calculate the water uptake according to Equation (3.9):

$$water \quad uptake = \frac{weight\ of\ wet\ membrane - weight\ of\ dry\ membrane}{weight\ of\ dry\ membrane} \tag{3.9}$$

The number of water molecules per sulfonic group, λ, is calculated from the water uptake and the equivalent weight (*EW*) for Nafion 115 or the corresponding, EW, value for the composite membranes (as it is described in Section 3.1.2):

$$water\ content\ (\lambda) = \frac{water\ uptake \cdot EW}{18} \tag{3.10}$$

where the 18 in the denominator is the molecular weight of water. A summary of the membrane water content measurement results as a function of the SiO_2 wt % is presented in Table 3.4:

Table 3.4. Water uptake, water content and weight of wet membrane data for Nafion 115 and Nafion 115/ SiO_2 membranes under liquid equilibrium at 25°C.

SiO_2 Wt %	Water Uptake g H_2O/ g dry Nafion	Water Content (λ) mol H_2O/mol SO_3	Weight of wet membrane g
0	0.25±0.007	19.46	0.008± 1E-3
10	0.20±0.004	15.02	0.004± 1E-4
16	0.24±0.016	18.70	0.0047± 2E-4
33	0.26±0.019	21.03	0.0053± 6E-5

3.5.2 Differential scanning calorimetry (DSC)

Fully saturated membrane samples were characterized with a DSC Q10 instrument (TA instruments®) to identify the ratio of freezable to non-freezable water present within the polymer. Non-freezable water is considered to be strongly bound to the ionic groups; meanwhile, the freezable water corresponds to the water molecules in free state with similar transport properties to bulk water. For the purposes of this work, the non-freezable water is referred to as bound water weight (W_b), and the freezable water as non-bound water weight (W_{nb}). The sum of both is the total water weight in the membrane:

$$W_t = W_{nb} + W_b \tag{3.11}$$

The membrane sample, of usually 4-5 mg was first equilibrated in liquid water and room temperature for 24 h before the measurement. Each sample was pat-dried and weighed in a sealed aluminum pan to avoid water loss and introduced to the temperature-controlled chamber to carry on the freezing and melting temperature scans using liquid nitrogen as coolant. During the test, the sample was subjected to a temperature gradient scan from 2 to -100°C to determine the enthalpy of the freezing water; and from -100 to 10°C for the melting enthalpy.

A heat flow curve was plotted for each experiment as the one shown in Figure 3.13a. The integrated area under the peak of the melting curve provided the heat of fusion for the corresponding sample. Its normalization with the heat of fusion obtained for bulk water (219 J g^{-1}) provided the mass of freezable water in the membrane. The mass of non-bound water is calculated according to Equation. (3.12):

$$W_{nb} = \frac{Enthalpy\ of\ fusion_{sample} \times weight\ wet\ membrane}{Enthalpy\ of\ fusion_{bulk\ water}} \tag{3.12}$$

The assumption that the heat of fusion for bulk water is equivalent to bound water used in this analysis is based on the discussion presented by Siu [31] on the basis of studies by Pintauro et al. [94], and Paddison et al. [95]. The authors found that the freezable water inside the pores of the membrane has the same dielectric constant to that of bulk water (within 10%). The water in the center of the pore, close to the wall, is kept in isolation from the electrostatic charge effect. Their studies estimated that 50% of the total volume of a fully hydrated pore of Nafion corresponds to liquid water, which has a similar value to the fraction of freezable water in the membrane.

Figure 3.13b shows the thermograms for Nafion 115 and composite-Nafion membranes with 10, 16, and 33 wt% SiO_2.

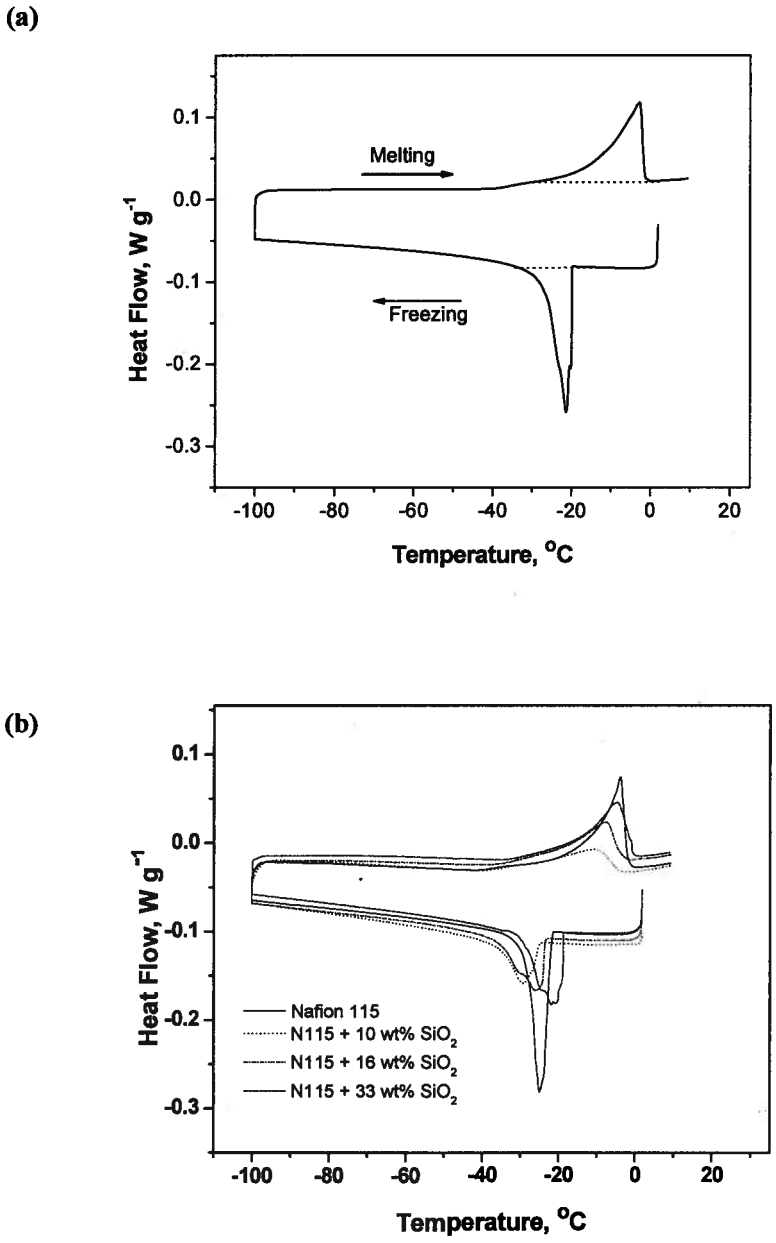

Figure 3.13. DSC thermograms: (a) typical signal for Nafion 115 in its hydrated form. The area under the peaks is integrated to calculate the enthalpy of fusion and freezing, respectively. (b) thermograms for composite Nafion 115/SiO_2

From the measurements, the heat of fusion values are summarized in Table 3.5.

Table 3.5. Enthalpy of fusion measured by DSC for Nafion 115 and Nafion 115/ SiO_2 membranes

SiO_2 Wt %	Enthalpy of fusion J/g
0	23.73±0.74
10	13.10±1.97
16	16.50±2.66
33	17.82±5.83

With the mass of total water content and the non-bound water known, from mass conservation the amount of bound (non-freezable) water is obtained. Results from these calculations will be presented in Section 6.6.

3.5.3 Dynamic vapour sorption (DVS)

In order to compare the mechanisms of sorption and desorption between pure Nafion and membranes containing silicon dioxide (SiO_2), Dynamic Vapour Sorption (DVS) measurements were performed under 25°C within the range 0 to 95% RH, using a DVS-1000 instrument (Surface measurement systems, London, UK). The DVS chamber includes temperature and humidity control, and a mass balance to record the membrane weight gain.

For sorption measurements, the membrane started from a dry state. With 10% RH incremental steps in the chamber, the membrane was driven to a maximum water uptake at 95% RH. In desorption experiments, the membrane started wet, equilibrated with the chamber at 95% RH, and it was driven to a dry condition decreasing the humidity in the

same differential steps until 0% RH was reached. At each relative humidity step, the experiment lasted until the membrane mass variation reached a minimum (dm/dt=0.0001).

Typical transient mass change response is shown in Figure 3.14, for sorption and desorption. The mass change along the plateaus of the sorption curves (Figure 3.14) was averaged to generate the steady state data set. The steady state mass uptake data was then converted into water content (λ) according to Equation. (3.10).

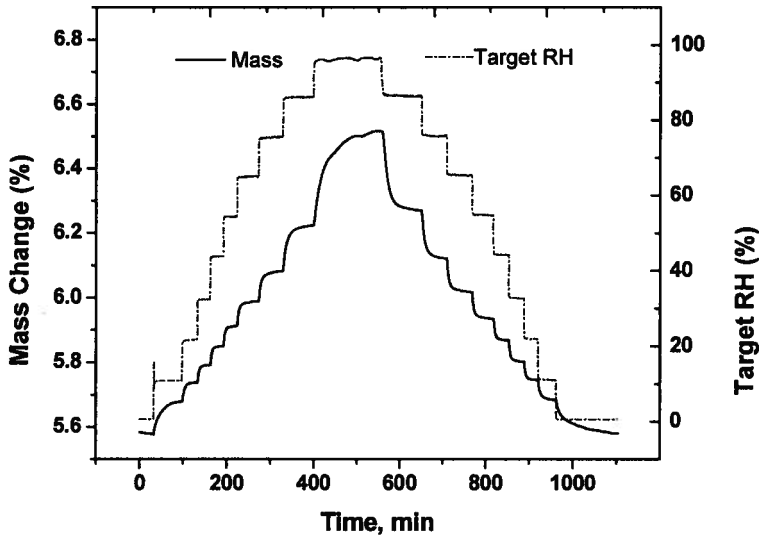

Figure 3.14. Vapour Sorption and Desorption kinetics resulting from varying the atmospheric relative humidity.

Figure 3.15, shows common isotherms for Nafion 115 and 117 from vapour sorption measurements, under steady state, at 25, 30, 50 and 80°C, obtained from the literature [11,56,96] .

The isotherms for vapour sorption obtained in this work, for Nafion 115 and Nafion 115/SiO_2 composite membranes, from the DVS measurements are included in Section 6.5.

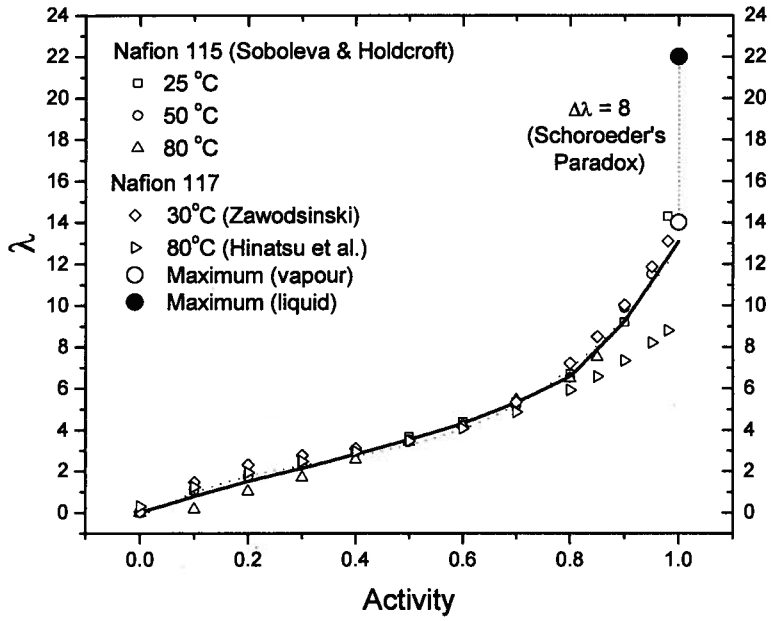

Figure 3.15. Membrane water content vs. water activity for Nafion 115 and Nafion 117 at different temperatures, from different sources.

The following chapter discusses the results of the previously discussed experimental techniques. Results from water transport measurements are presented for Nafion membranes in Sections 4.1 and 4.2. Steady state water transport was also measured for SiO_2-Nafion membranes; results are included in Chapter 6.

In Chapter 6, results from DVS, DSC and water content are presented for Nafion and composite-Nafion membranes.

4. Results from Water Transport in Nafion Membranes

This chapter summarizes the results from water transport measurements across Nafion and composite/Nafion membranes. The first section (4.1) presents results from permeability experiments in Nafion membranes under steady state. The mass transport was studied as function of the temperature, thickness, water content, and physical state of water in contact with the membrane. The contribution of the gas-membrane interfaces to the mass transport resistance became evident from non-isothermal experiments and thickness comparison under steady state. The second section (4.2) presents the analysis of water transport (WT) under transient conditions as a function of thickness, temperature and contact with vapour and liquid water. To my knowledge, transient measurements of the WT across both interfaces of Nafion under the effect of activity gradients are the first to be reported. From the dynamic flux data, the temperature and thickness comparisons suggested that surface limited mechanisms become important at high temperatures.

4.1 Steady state water transport in Nafion membranes

Using the experimental set up described in Section 3.2, transport experiments were carried out with pretreated Nafion 115 membranes. The following sections present results under isothermal and non-isothermal conditions.

4.1.1 Isothermal conditions

The flux across the Nafion membrane was calculated as described in Section 3.3. Figures 4.1a and 4.1b summarize the results for the experimental series: liquid equilibrated (LE) and vapour equilibrated (VE) Nafion 115 membranes, respectively. On the x-axis, the accuracy from the gas mass flow controllers is ±0.6 % cm^3 min^{-1} (STP). The error bars correspond to the accuracy in the dew point manufacturer's calibration with a maximum possible error of ±0.03 $molm^{-2}s^{-1}$. These are absolute errors since our experimental error was negligible: the maximum error found from reproducibility tests was ±0.001 mol m^{-2} s^{-1}. Moreover, based on the cross-reference tests between the dew point sensor and the mass spectrometer (Appendix C), it was assumed that the flux trends observed in Figures 4.1 a and b are independent of the sensor's accuracy, i.e. the flux dependency on the gas flow rate is expected to maintain the same profile even with a different type of humidity sensor.

The calculated water fluxes for LE membranes were larger than the fluxes from VE membranes at similar temperatures and helium flow rates. For these experiments, we assumed a water content profile across the membrane. The increasing flux of water with gas flow rate supports our assumption of high absorption and diffusion rates in the membrane, and slow evaporation to the (dry) gas phase. These assumptions are based on the higher water uptake capacity of Nafion when the membrane is in contact with liquid water, compared to a lower uptake when the membrane is surrounded by saturated gas [56]. Our measured water fluxes from LE membranes agree with published values using dry gas to produce activity gradients [19].

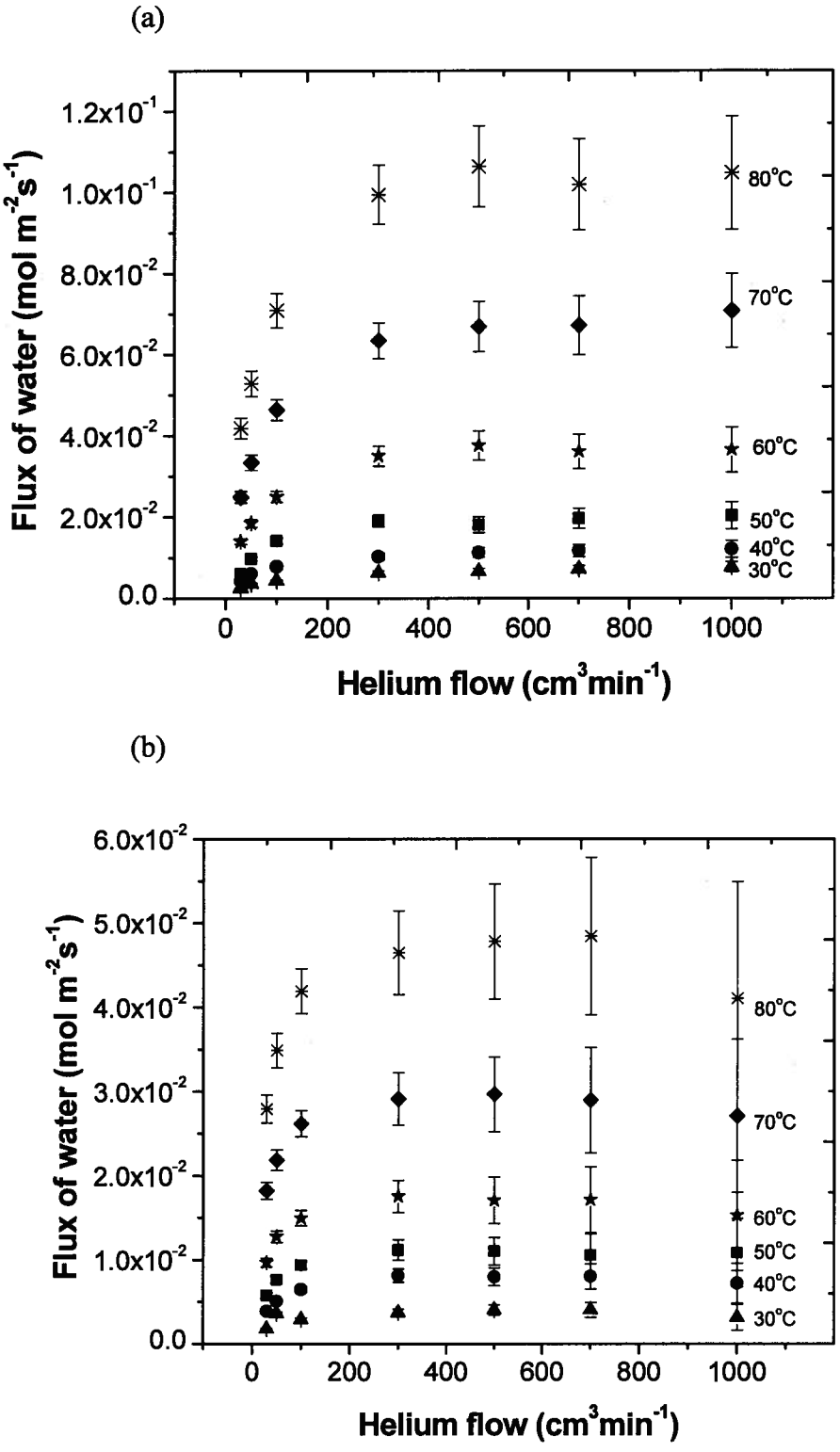

Figure 4.1. Measured steady-state water flux was measured for (a) LE and (b) VE membranes, between 30 to 80°C and atmospheric pressure. Note the difference in the scales.

In Figure 4.1b, for VE membranes, fluxes were lower (~50%) than the values observed with LE membranes (e.g., 0.046 and 0.026 $molm^{-2}$ s^{-1} at 70°C and 100 cm^3min^{-1} for LE and VE membranes, respectively). Several authors have related this difference to Schroeder's paradox. Recently, it was reported that this difference is due to membrane structural changes created by the thermal histories of the membrane prior to the tests. These studies related the change in water uptake with structural modifications produced in the polymer by thermal stresses during preparation of MEAs. Those reports concluded that thermal stresses can affect the water content and water transport in the membrane [56,64].

Contrarily, the samples used in these investigations received the same thermal treatment, and therefore, it can be assumed there was no thermal history difference associated to the higher water transport in LE compared to VE membranes. Instead, a proposed explanation is based on the Nafion surfaces changes, from hydrophobic to hydrophilic, discussed elsewhere [59,60]. The surface switch has been measured by receding and advancing contact angle of water droplets on Nafion, and found that the membrane interface switches from hydrophobic to hydrophilic when it is contacted with liquid water [35,57]. This is consistent with the model of micellar structures that provide a hydrophobic membrane surface in membranes with low water content [34,55].

In VE membranes at high temperatures, (Figure 4.1b), the lower water fluxes suggest that the membrane surface dehydration gets exacerbated with high gas flow rates (Figure 4.1b). This behaviour was observed by Majsztrik and collaborators [62] and explained in terms of a hydrophobic skin layer formation. If local dehydration occurs

close to the membrane surface, it is possible that water dynamics are slow down due to the poor interconnections between pores and the decreased pores size.

Following a temperature dependence analysis, it was found that the water transport flux is well described by Arrhenius temperature dependence. The graphs in Figure 4.2 show the curves: log of flux *vs.* 1/T, for Nafion 115 at different gas flow rates.

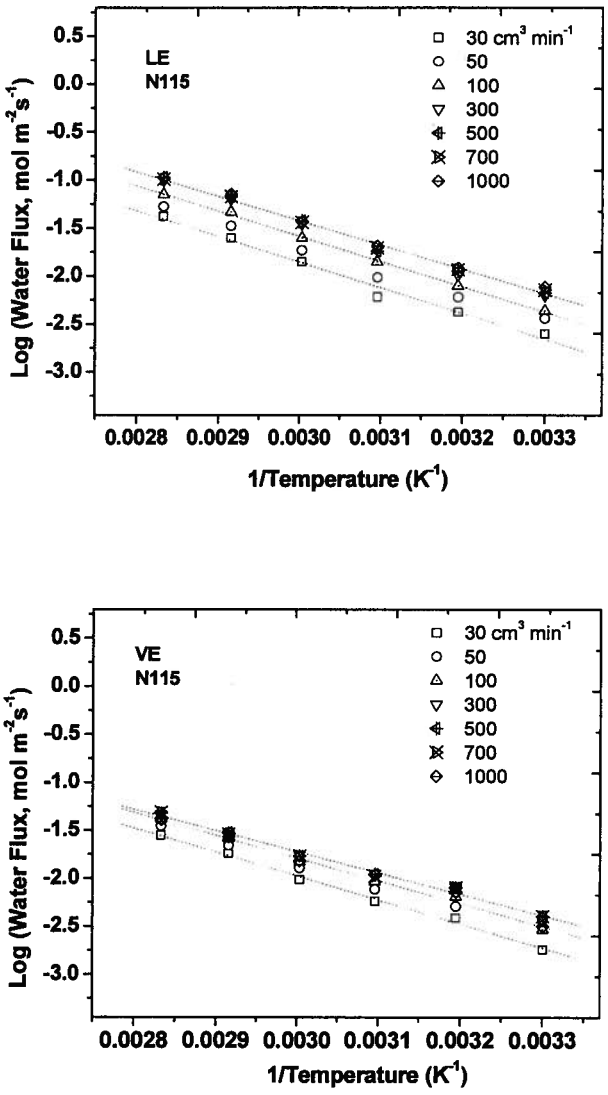

Figure 4.2. The measured flux across Nafion 115 is shown at atmospheric pressure for varying the temperature. Liquid water fluxes (solid symbols) and vapour fluxes (hollow symbols) are shown. The inset shows the Arrhenius dependency of the flux with temperature.

The graph in Figure 4.2a shows the LE case, where the slopes of the linear fit generated activation energy values that decreased with the increasing gas flow rate. In Figure 4.2 b, the VE case shows the slopes of the fitted lines increasing in a slower pace to the flow rate variation than in the LE case. Table 4.1 shows the Activation Energy (E_{act}) results.

Table 4.1. Activation Energy for Nafion 115 membranes equilibrated with liquid and vapour water

Helium Flow cm^3min^{-1}	E_{act} $kJ\ mol^{-1}$	
	LE	VE
30	51.24	47.84
100	50.45	45.57
300	50.48	42.97
500	50.53	42.41
700	48.54	42.44
1000	48.07	43.56

The averaged value of E_{act} for LE showed a value of 50 ±0.58 kJ mol^{-1} ; meanwhile, for VE membranes averaged 44 ±0.88 kJ mol^{-1}. Considering a 25 % error anticipated from neglecting the energy balance (Section 3.3.2), it is possible that the E_{act} of the VE steady state water transport approximates the enthalpy of water vaporization ($\Delta H^{vap} = 36.78$ kJ mol^{-1} [90]). The reason why LE shows a higher value for the E_{act} is not understood. It has been presented before that the interaction between water and the polymer is stronger for LE membranes. Futerko and Sing [60] explained that the structure of the membrane is altered when it is contact with liquid water, as stronger interactions are formed between the water molecules and sulfonic acid groups. The difference with a VE membrane, is that the vapour water molecules interact between each other and

desorption from the membrane is easier as the interaction between solvent and polymer is weak. The observations from Zawodzinski et al. [57] agreed with the concept of an stable and natural hydrophobic surface of the membrane, which suffers alterations when it is equilibrated with liquid water, switching to a hydrophilic type. Thus, it can be inferred than the higher E_{act} for LE may be attributed to the difficulty to detach water from the polymer in order to desorption to occur. Physical parameters of the membrane as porosity, water confinement, and connectivity of pores could be included in a further analysis to explain this observation in a phenomenological way.

4.1.2 Non-isothermal conditions

Non-isothermal conditions were applied across the membrane to enhance evaporation to the dry chamber. The temperature was increased in the dry chamber to increase the amount of water that could be present in the saturated gas mixture. Figure 4.3 compares three isothermal experiments at 30, 40 and 50°C, with their non-isothermal counterparts at a constant temperature gradient, $\Delta T = 30°C$ (i.e., T1 = 30, 40, 50°C, and T2 = 60, 70, 80°C)[3].

The LE series (Fig. 4.3a) yielded monotonic increases in water flux up to moderate flow rates, exhibiting a maximum, after which the flux across the membrane decreased below the corresponding flux for isothermal conditions. The corresponding VE series (Fig. 4.3b) showed a maximum flux at lower flow rates than their counterparts in the LE series. These results are consistent with an evaporation rate threshold above

[3] The case where T1>T2 was not addressed because of the condensation problems associated. In such a case, the enhanced water flux would lead to condensation in the lower temperature chamber where the sensor was located, which would mask the membrane water transport data.

which the surface of the membrane experiences a deeper dehydration (from the dry gas). Conversely, the absorption rates on the humidified vapour side were possible insufficient to keep the bulk of the membrane hydrated. In this manner, the gas–membrane interface became an effective barrier for water transport moderated by the lower availability of water in the wet side, and showing higher resistance at high flow rates. In LE membranes, the gas–membrane interfacial resistance became limiting only at high flow rates.

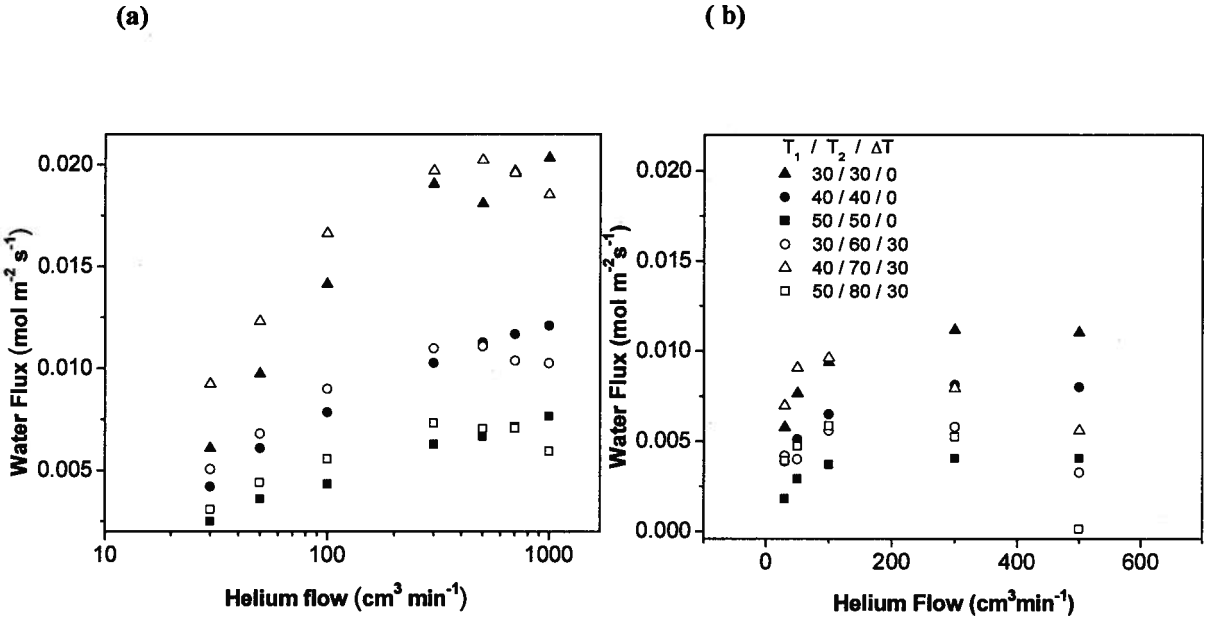

Figure 4.3. Measured steady state flux of water across Nafion 115 membranes comparing isothermal (solid) and non- isothermal (hollow) conditions for (a) LE membranes, and (b) VE membranes.

Many performance indicators for water transport across membranes have been used in the context of humidifier design. These include the water recovery ratio, humidity ratio and the deviation from full saturation [97]. A normalized relative humidity ratio, ((1-RH)/RH), was used to characterize water transport across membrane interfaces [98].

Figure 4.4 shows the measured water transport for the isothermal and non-isothermal experiments. Higher temperatures in the VE membranes showed higher ratios (i.e., higher resistances to water transport) compared with the LE counterparts. These results suggest the existence of resistive interfaces at membrane surfaces under vapour equilibrium conditions.

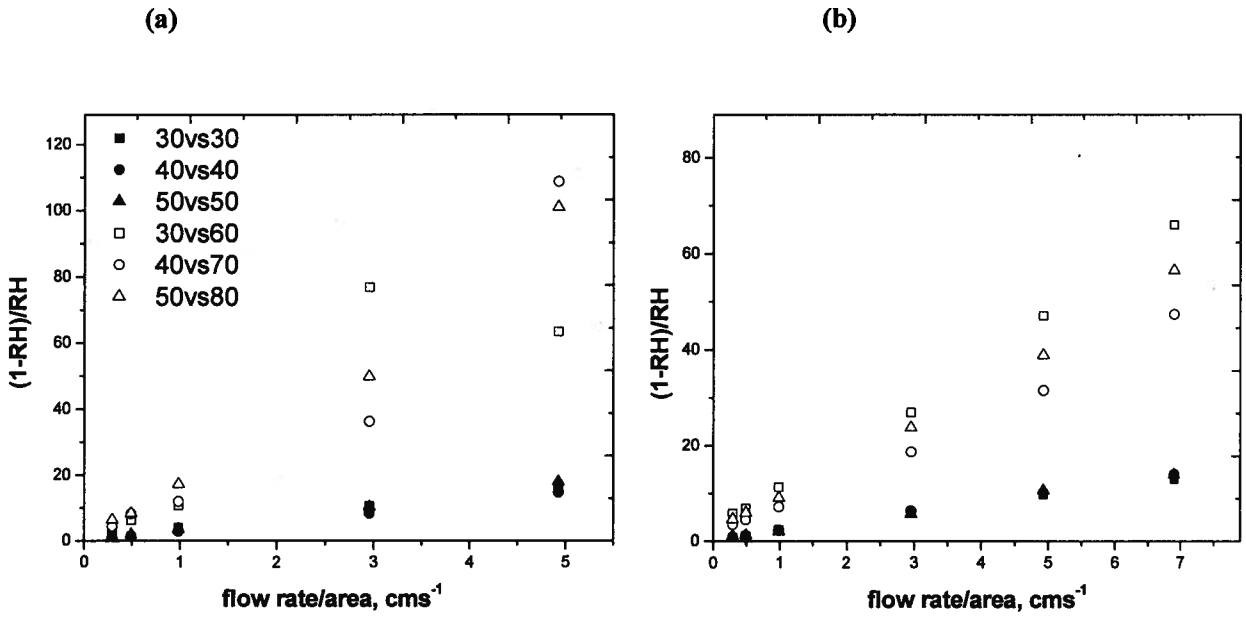

Figure 4.4. Calculated resistance to water transport for Nafion 115 in (a) vapour, and (b) liquid equilibrium as a function of the gas flow rate in isothermal (solid symbols), and non-isothermal conditions (hollow symbols).

4.1.3 Water profile across the membrane interfaces

The abrupt decrease in water flux (Figure 4.3b) provides evidence for the existence of non-linear water concentration profiles within the membrane. F. Buchi and G. Scherer [99] have reported on such water profiles across Nafion membranes under fuel cell operation. Small angle neutron scattering (SANS) data showed that the membrane can have discontinuous variations in its hydration levels. However, across the membrane interfaces, description of the water concentration profile raises different challenges.

In an attempt to define the water concentration profile across the interfaces, an analysis was carried out to determine and compare the water concentration in three different phases: saturated gas, membrane and bulk water. The analysis below shows the implications when using water concentration as the normalized parameter for the water transport driving force.

An approach common to the fuel cell literature was applied[15] to quantify water concentration in the membrane. Empirical material properties were used to calculate an effective water concentration:

$$c_{H_2O} = \frac{\lambda n_{SO_3^-}}{V_d + \Delta V} = \frac{\lambda \rho_d}{EW}\left(\frac{1}{(1+\gamma)}\right) \tag{4.1}$$

where ρ_d= 2 gcm^{-3}, EW=1100 g mol^{-1}. The constant in the denominator ($\gamma = \Delta V/V_d$) was used to quantify the change in volume upon hydration (ΔV) as a fraction of the original volume of dry membrane (V_d=0.025). The water concentration was calculated for

$24>\lambda>0$, and for $1>\gamma>0$. Results from this calculation are shown in Figure 4.5. The expression in Equation (4.1) is an approximation because the water is present in the hydrophilic regions only. Dividing by the total membrane volume provides an average water concentration over both hydrophobic and hydrophilic regions.

Figure 4.5 compares the water concentrations calculated with Equation (4.1) and compares them with the corresponding concentrations in fully saturated air and liquid water (between 15 and 90°C). As illustrated, even for low water contents ($\lambda < 5$) the calculated water concentration inside the membrane is much larger than the corresponding value for fully saturated air. Considering the hydrophilic regions only would make the membrane water concentrations even larger.

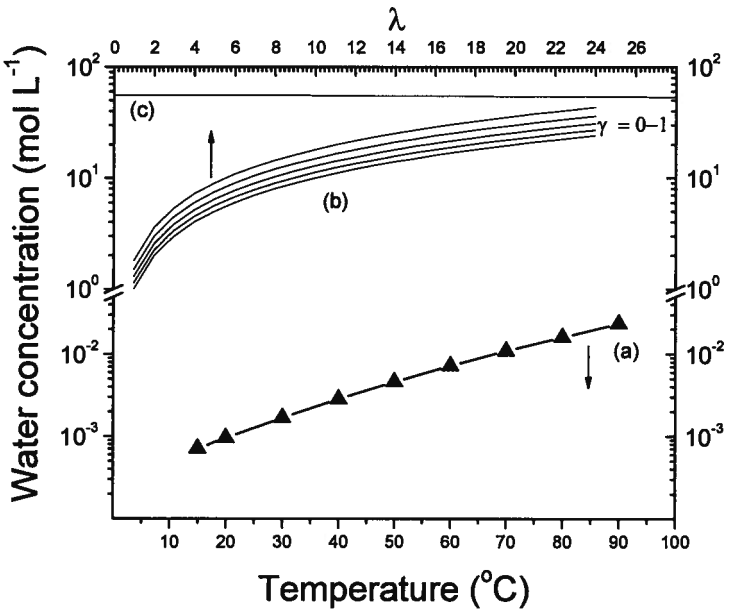

Figure 4.5. The water concentration corresponding to fully saturated gas mixtures at different temperatures (a) is compared to the calculated water concentration at different membrane water contents (b). The family of curves in (b) assumes a range of volume changes upon hydration (i.e., 0-100% of the original dry volume. The concentration in liquid water (c).

These results contradict the prior expectation of a positive water concentration gradient, which is thought to be the main driving force for water transport across the membrane interface when it is equilibrated with saturated air (i.e., VE membrane).

This inconsistency highlights the need for a normalized driving force parameter that considers thermodynamic(*T, P, RH,*) and membrane physical variables (λ, *EW*, ρ, *porosity,* etc.) to characterize water profiles across the interfaces. Due to the lack of a definition for the driving force across the membrane interfaces, an absolute representation of water concentration profiles is not doable. Similarly, using water activity as the normalized parameter raises inconsistencies, as both liquid water and vapour saturated have activity=1, which has lead to the mystification of an existing paradox (Schroeder's) to explain the membrane water uptake difference, instead to promote the need for a solid explanation of the occurrences at the membranes interfaces.

4.1.4 Thickness dependency

The mass transport across Nafion membranes of different thicknesses was measured. Figure 4.6 summarizes the fluxes for Nafion 112, 115, and 117 with wet thicknesses equal to 51, 127, and 183 μm, respectively.

In all cases, the flux decreased with increasing thickness, but the difference disagreed with flux predicted by Fick's law, as explained below.

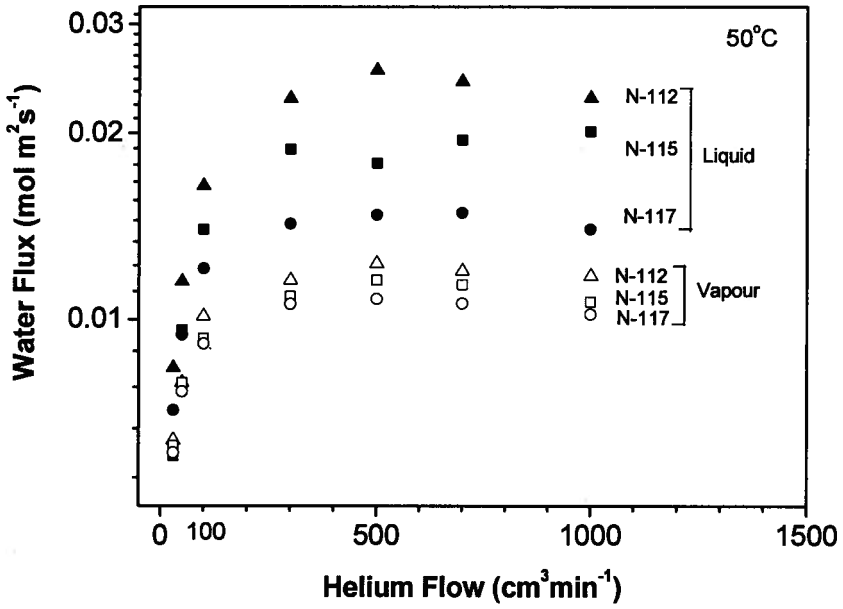

Figure 4.6. Comparison of water flux across membranes with different thicknesses, from 51 to 183 μm, measured at 50°C, in VE (hollow) and LE (solid)membranes.

The same data was plotted as a function of the wet membrane thickness. The graphs in Figure 4.7 show the fluxes for Nafion 112, Nafion 115, and Nafion 117. The tendency of the flux is shown to decrease with higher thickness in both data sets. The

graphs show the predicted flux determined by Fick's law (i.e., inverse thickness dependency) for the flux of Nafion 112. The predicted flux for VE (Figure 4.7a) and LE (Figure 4.7b) were calculated using the flux of Nafion 117 as reference at same activity gradient, based on the thickness decrease from 183 to 51 μm (used data correspond to the fluxes at activity gradient of 0.6 for VE, and 0.5 for LE).

In Figure 4.7a, the predicted flux for VE: 2.4 $x10^{-2}$ $molm^{-2}s^{-1}$ showed one order of magnitude difference with the actual measured flux of 7.9 $x10^{-3}$ $molm^{-2}s^{-1}$. In Figure 4.7b, for the LE case, the estimated flux for Nafion 112 was 3.5 $x10^{-2}$ $molm^{-2}s^{-1}$, and the measured value showed a flux of 1.15 $x10^{-2}$ $molm^{-2}s^{-1}$.

These results suggest that diffusion is not rate dominant in thin membranes (51 μm), and that resistances at the membrane surface play an important role to the mass transport across the Nafion membranes, especially when equilibrated with vapour water.

The mass flux loss is consistent with results from Majsztrik and collaborators [62] in the thickness range of 51 to 254 cm. These authors explain that resistances to mass transport dominate over diffusion resistance, yet they were not able to quantify the surface and bulk resistances.

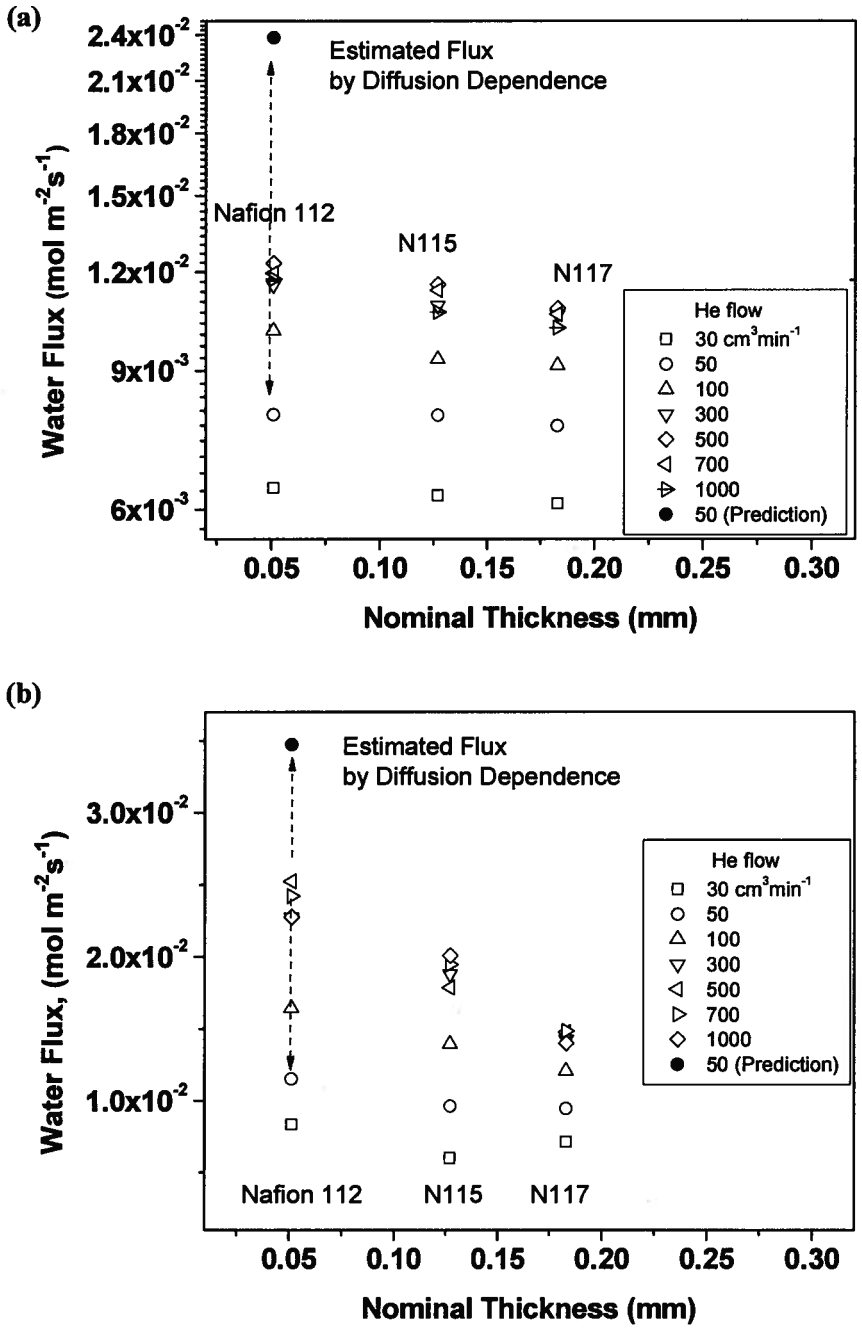

Figure 4.7. Comparison of water fluxes at 50°C from three different thicknesses: 51:127:183 μm in their expanded form. (a) VE membranes; (b) LE membranes.

The Vaporization-Exchange model, included in Section 5.2, had as objective the quantification of these resistances. The analysis, successfully identified the interfacial mass transport rates and bulk diffusivity using the steady state and transient water transport data presented in this chapter. The following section describes the transient data from liquid WT experiments on Nafion.

4.2 Transient water transport

Experiments on Nafion of different thicknesses were carried out between the temperature range of 30 to 70 °C in the time domain and under activity gradients. These experiments are the first report on transient water transport measurements under activity gradients. Transient data reported previously has been obtained from DVS experiments where the membrane is surrounded homogenously with saturated gas at specific relative humidity, and membrane water uptake is recorded [56,62,77].

Contrarily, in the transient water transport experiments presented here, the membrane is subjected to an activity gradient to act as the water transport driving force. Using the setup described in Section 3.5 the water crossover flux was measured as a function of time. The typical response is shown in Figure 4.8, and it shows the dynamic flux from an initially dry condition (the membrane was dried for 20 hrs in room temperature followed by conditioning under the dry chamber temperature and humidity for 5 hrs) until the final steady state.

The flux data from transients were analyzed with the mathematical models included in Chapter 5.

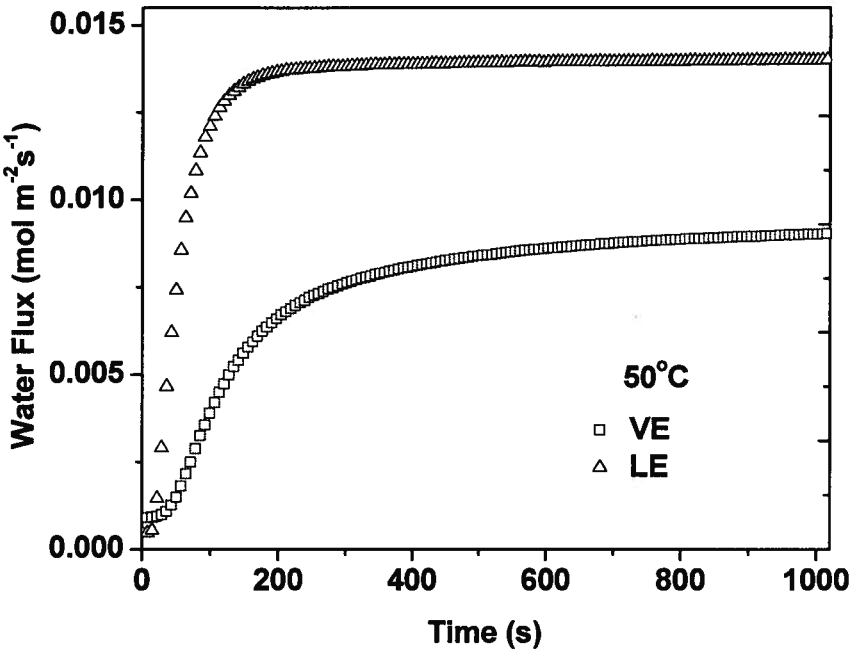

Figure 4.8. Comparison of physical state of water in contact with the membrane during transient water transport. Flux measured experimentally at 50°C for liquid equilibrated (triangles) and vapour equilibrated (squares) Nafion 117

As an exploratory exercise, the flux derivative on time was calculated for the transient water transport flux. The following section (4.2), discuss the observations from the derivatives of the flux, from which a rate of change was obtained and a maximum value was identified. It is not the purpose of this analysis to discern the interfacial from bulk transport phenomena, but to explore the effects from the temperature and membrane thickness variation in the transient response.

Figure 4.9 illustrates the rate of change for fluxes (i.e., 2nd derivative of the moles of water) in vapour and liquid equilibrated membranes. The graph shows that the rate of change was faster for liquid than for vapour. The graph also shows that the maximum rate was reached for vapour faster than for liquid. This suggests a slower water transport rate across the vapour-membrane interface.

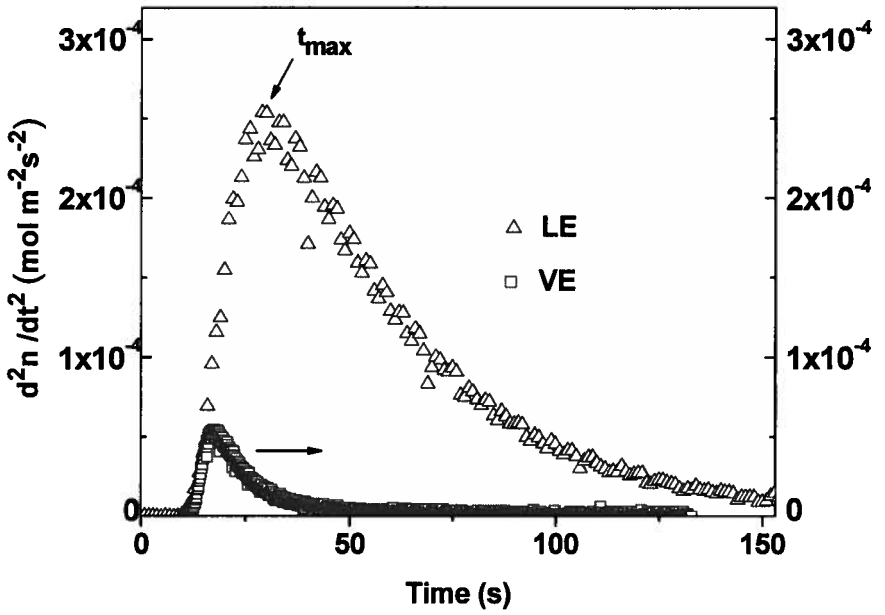

Figure 4.9. The flux derivative is compared for a Nafion 117 membrane in LE and VE conditions.

4.2.1 Temperature and thickness effects

In order to determine the effect from temperature variation, transient measurements were carried on for Nafion 112 and Nafion 117 membranes at 30, 50 and 70°C. The concept of the derivative used here has no direct meaning on the identified mechanisms of water transport.

Figure 4.10a and 4.10b include the derivatives of fluxes in Nafion 112 and Nafion 117, respectively. Original flux data from experiments are included in the inset plots. The major difference is observed at 70°C, with a higher maximum rate for the Nafion 112 membrane.

Figure 4.10c contains the summary of the derivatives of the fluxes for Nafion 112 and Nafion 117, within the thickness range: 51: 183 μm, in LE and VE conditions at

50°C. The maximum peaks confirmed that liquid in Nafion 112 had the highest rate among them. The slopes after the maximum for each membrane overlapped between each other. This suggests a thickness-independent mechanism taking the rate control after reaching the maximum.

The graph in Figure 4.10d compares two experiments with Nafion117 membranes liquid equilibrated at 50°C after receiving a different pretreatment. The highest of the derivative curves corresponds to a membrane dehydrated for 20 hours prior to the testing, and it is compared to a membrane dehydrated for 72 hours. The latter showed a process slower than the former. The time to reach steady state increased 30% for the membrane with the longest drying history. The deviation between the final steady state between both membrane fluxes showed a 16% difference which falls far outside the experimental error (2% difference). Through independent weight measurements it was found that the water content of the membrane showed no change between 20 and 72 hours of drying. Whether the dehydration under atmospheric air produced membrane structural changes after the first 20 hours is not clear. Further experiments are required to explain the source of this difference.

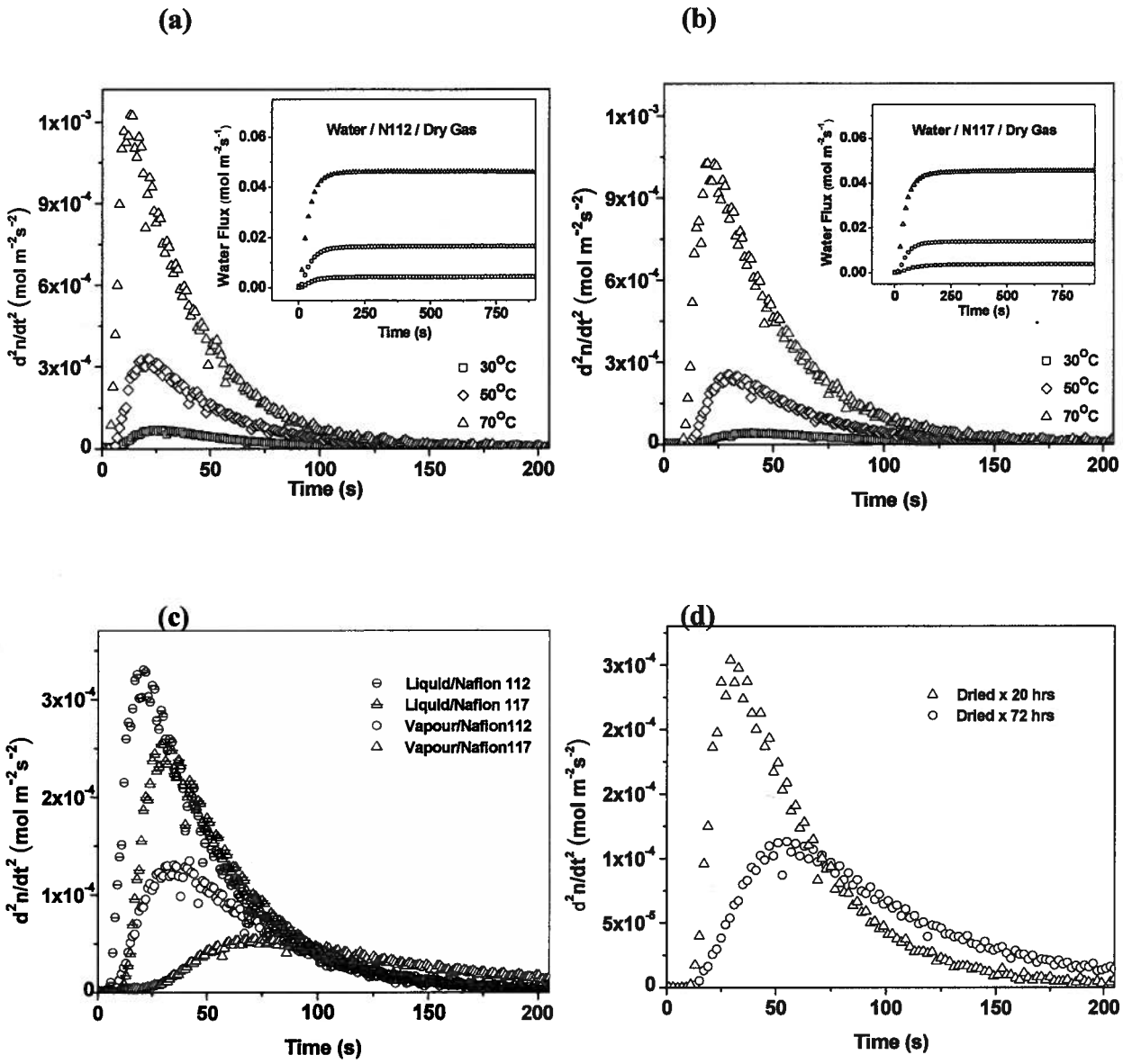

Figure 4.10. The acceleration of the flux across the membrane as a function of time. Temperature effect for (a) Nafion 112, and (b) Nafion 117, at 30, 50, and 70°C in LE samples. (c) Comparison between liquid and vapour rate of transport in Nafion 112 and Nafion 117. (d) LE Nafion 117 membrane for two different water content conditions: after dehydration for 20 and 72 hours.

From the derivatives, the time at which the maximum rate of change occurred, t_{max}, corresponds to the inflection point of the dynamic water transport curve before the final steady state. When $t_{ss,initial}$, $t_{ss,final}$ and t_{max} were compared for Nafion 112 and Nafion 117, at 30, 50, and 70°C two different trends were observed, as depicted in Figures 4.11a, b, and c.

In Figures 4.11a and 4.11b $t_{ss,initial}$ and t_{max} showed linear response to the temperature variation; and it was reproducible for both membrane thicknesses. Both $t_{ss,initial}$ and t_{max} decreased with higher temperature and smaller thickness.

In Figure 4.11c, $t_{ss,final}$ decreased with the temperature raise with higher variation between temperatures for Nafion 117. The difference with respect to thickness became negligible at 70°C. These results suggest that bulk diffusion is overcome by a thickness-independent mechanism at 70°C. Further analysis on this area is part of ongoing investigations in the author's research group.

The previous experimental data confirms that surface resistances are present on the membrane-gas interfaces, especially at temperatures above 50°C. In an attempt to elucidate surface and bulk diffusion processes, two models were developed to assist in the analysis of steady state and transient water transport data.

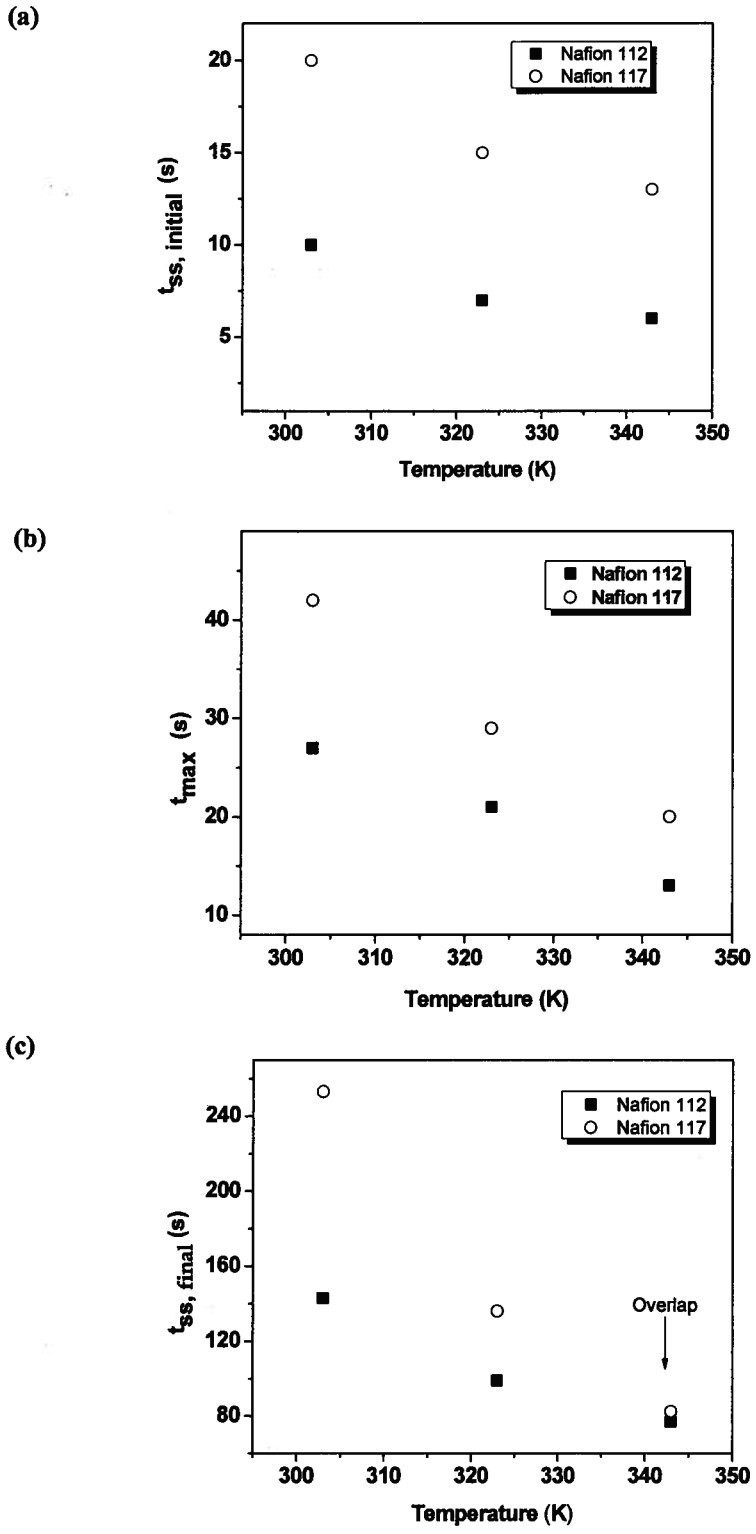

Figure 4.11. Measured times in LE Nafion 112 and 117 membranes: (a) time before the signal started to raise $t_{ss\ initial}$, (b) time to reach maximum acceleration in the flux t_{max}, and (c) time to reach the final steady state $t_{ss\ final}$.

5. Mathematical Models

To elucidate the individual contributions from surface and bulk water transport mechanisms, the Varying Diffusion Coefficient (VDC) model, was developed to provide a first approximation on the incorporation of surface mechanisms of transport to the bulk. From this model, the quantification of the resistances was not achieved, but it gave insight on the need to describe a boundary condition to represent the membrane interface more accurately.

A second phenomenological solution named the Vaporization-Exchange model (VEM) was proposed to separate the contributions to the mass transport from the surface and the bulk. The model described a dynamic membrane-gas boundary and related the gas flow rate with the resulting humidity in the chamber. Application of the model to the transient data generated values for the interfacial water transport rates: k_v; the diffusivity coefficients and the maximum concentration of water (Dc_{max}). These results proved the importance of the membrane boundary s in the analysis of water transport phenomena.

The two models applied to the WT data are contributions from independent groups. The VDC model is an analytical solution proposed for the transient data as requested to Dr. Brian Wetton from the Department of Mathematics-UBC. The adaptation of the model to MATLAB language was performed by Peter Cave, a former Masters student in the Department of Mechanical Engineering. A preliminary data analysis is presented in his Master's thesis [100].

The Vaporization-Exchange Model is an original contribution from Dr. Charles Monroe from Simon Fraser University. The model along with my experimental data have been accepted for publication elsewhere [98].

My contribution to these analyses lies on the proposed resistance in series analogy for water transport across the membrane, the design of the experimental setup and variables to make the data amenable to theoretical simulations, and the participation on the data analysis and phenomenological interpretation.

5.1 Mass Transfer Coefficients from Varying Diffusion Coefficient (VDC) Model

A mathematical solution was applied to transient water transport data to deconvolute bulk diffusion from surface mechanisms. This model was based on the resistance in series array to account for the resistance to water transport in each stage of the overall process. Equation (5.1) includes mass transfer coefficients for the mechanisms across the surfaces and within the membrane bulk giving an overall mass transfer resistance [101,102]:

$$\frac{1}{k_{overall}} = \frac{1}{k_a} + \frac{1}{k_{Diff}} + \frac{1}{k_d}, \tag{5.1}$$

where k_a, k_{Diff} and k_d correspond to mass transfer coefficient for absorption, diffusion and desorption, respectively. The model incorporated the Fick's diffusion theory with a boundary condition based on Henry's law to define the membrane water content in terms of the water sorption isotherms. The model is described in detail in Appendix E.

Based on Equation (5.1), transient experimental data were used to estimate the sorption and diffusion terms in Equation (5.2):

$$J = a\frac{\Delta\lambda}{\frac{1}{k_d}+\frac{L}{D}}\ , \qquad (5.2)$$

$\Delta\lambda$ represents the water content difference across the thickness L of the membrane, and a is the concentration of sulfonate sites in the membrane, k_d and D correspond to the mass transfer coefficients for desorption and diffusion, respectively. Both coefficients lead to a given steady state flux J written in terms of a basis parameter θ in (0,1).

The model simulates fluxes between two boundary conditions that describe either:

a) a diffusion-limited extreme case, with θ =0, and
b) a surface-limited extreme case, with θ = 1

The model considered water transport to obey the diffusion equation and the diffusion coefficient, D, is allowed to depend on water content in general:

$$\frac{d\lambda}{dt} = \frac{d}{dx}\left(D(\lambda)\frac{d\lambda}{dx}\right) \qquad (5.3)$$

The variable diffusion coefficient is described by $D(\lambda) = \delta\lambda$, where δ is a constant.

For every $\theta \in (0,1)$, values of k_d and δ were obtained that together match the steady state flux J. The value of θ that minimized the least square regression error between simulation and experimental data was used to determine final k_d and δ values.

The model compared simulated signals with experimental fluxes across the membrane in different conditions. Figure 5.1 represents an example of the comparison.

Figure 5.1 compares transient flux data for Nafion 117 at 50°C, a θ value of 0.8 was found to minimize the least square regression error. Using a=1789 mol $SO_3^-m^{-3}$ and L=0.183 mm yields values of δ=3.10x10^{-11} m^2s^{-1} ($molSO_3^-$)($molH_2O$)$^{-1}$ and k_d =6.097 x10^{-7} m s^{-1}. The simulated flux showed a good fit in the short and long term of the rising signal.

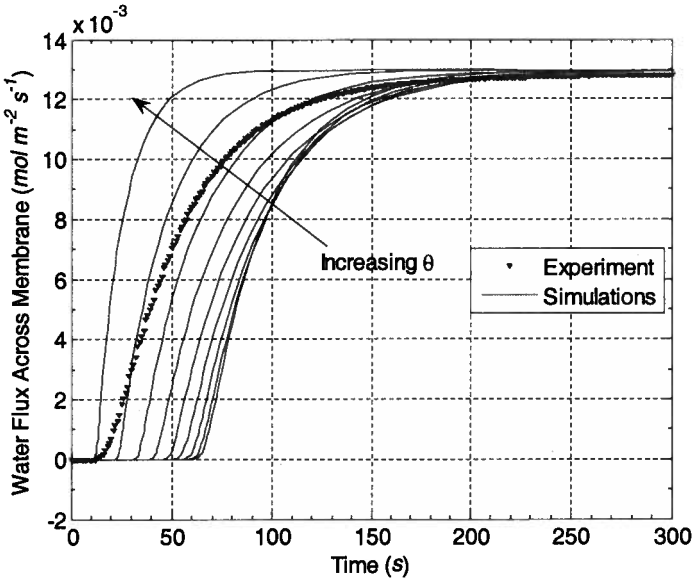

Figure 5.1. Experimental *vs.* simulated transient data for initially dry membranes. Transport flux across Nafion 117 at 50°C. Continuous lines in the background show the model simulation with θ changing from 0.1 to 0.9 in increments of 0.1.

Figure 5.2 shows the transient data fitting for (left) Nafion 112, and (right) Nafion 117 at 30°C. The model predicted longer times for the thicker membrane which agrees with the data. The offset occurred in the long term for the thinnest membrane (left) meanwhile, for the thick membrane (left) the model over predicted the signal raise in the short term.

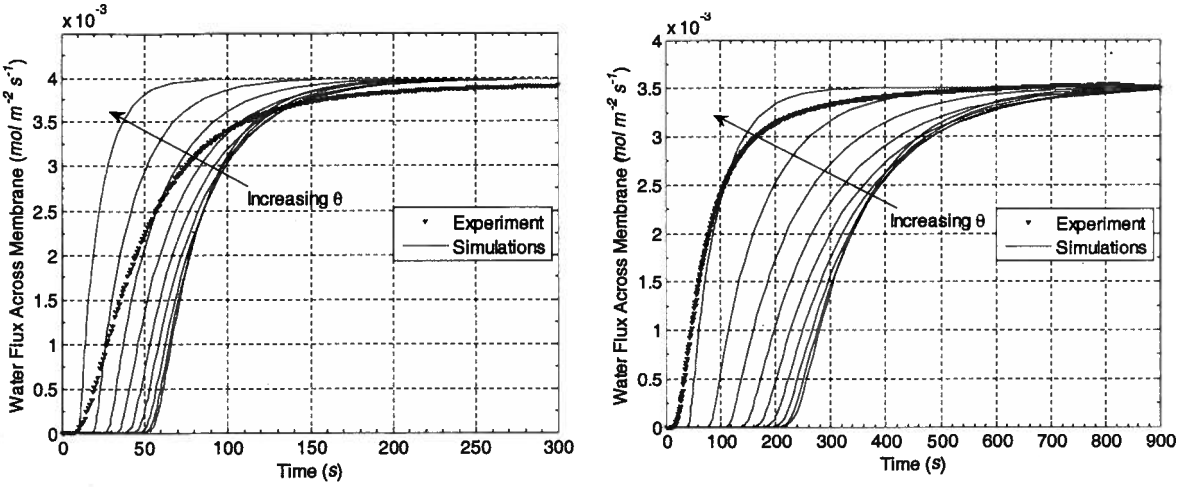

Figure 5.2. Experiment vs. simulation transport flux across Nafion 112 (left), and Nafion 117 (right) at 30°C. with θ increasing from 0.1 to 0.9.

Reproducibility tests revealed that the final steady state of the water signal is highly related to the initial condition in the membrane. If the dew point had a lower initial value, the final steady signal showed variations of ±3°C. This data variability complicated the fitting process, especially in the long time. In the short time domain, the offset was believed to come from the model's neglect of a boundary condition that describes the interaction between the gas flow rate and the evaporation of water from the surface.

Table 5.1 shows the results for k_d and δ in Nafion 112 and Nafion 117 at different temperatures. The value of θ that minimized the least square regression error between simulation and experimental data decreased with the increase of temperature and increased with thickness. The fact that increasing the temperature θ approaches zero, it suggests that diffusion becomes the limiting mechanism at high temperature (because θ=0 means a diffusion-limited scenario). These results agree with observations from the transient experimental measurements.

Table 5.1. Summary of diffusion and surface transfer coefficients from model for liquid equilibrated Nafion 112 and 117 at different temperatures. The best θ fit is shown for each experiment.

Temperature °C	$\delta \times 10^{12}$ $\left(\frac{mol\ SO_3^-}{mol\ H_2O} \cdot \frac{m^2}{s}\right)$	$k_d \times 10^7$ (m s^{-1})	θ best fit
		Nafion 112	
30	1.52	2.1	0.73
50	2.86	19.7	0.29
70	7.31	50.1	0.29
		Nafion 117	
30	13.88	1.49	0.91
50	19.95	6.51	0.76
70	28.79	44.43	0.34
From literature:			
80	Berg et al.	57	
80	Ge et al.	45-325 (λ=1-9)	

The model calculated mass transport coefficients for desorption that agreed with results from Berg et al. and Ge et al. [78, 86].

Where the model failed was in the prediction of a constant δ for both thicknesses. The changing δ disagrees with its expected constant value, so that D would be a function of l only (because $D(\lambda) = \delta\lambda$). The explanation for this inconsistency remains uncertain. But may be solved by incorporating the 3-dimensional nature of the diffusion process trough a porous media: as thickness increases, the assumption of a 1-D linear path for water becomes simplistic.

One of the limitations of the model, as mentioned before, is the assumed fixed boundary condition on the dry membrane surface. The model fixed the water concentration of the dry chamber to the initial water content value during the transition time. The following section describes a phenomenological model that proposes a dynamic boundary condition, which describes more accurately the kinetics of vaporization and condensation processes at the surface.

5.2 Membrane Bulk and Boundaries. Analysis of Water Transport with the Vaporization-Exchange Model

5.2.1 Description of the Vaporization-Exchange Model (VEM)

The experimental water transport data from this work raised interest for solving the contributions from interfacial and bulk resistances in Nafion. A different approach to account for the membrane interfacial phenomena was proposed with the Vaporization-Exchange model [98] using the steady state and transient measurements. The model described the dynamic transport of water across the membrane bulk and interface due to the vapour pressure gradient across the interface. The problem was translated to a dimensionless analysis, and the suggested system of governing differential equations was solved for initial and boundary conditions that represented with accuracy our experimental conditions.

Traditional models for water transport in Nafion considered a fixed boundary condition described, often by the correlation between isothermal vapour pressure and membrane water content from equilibrium gravimetric measurements. The previously described VDC model for transient transport (Section 5.1) used, in this way, isothermal data for describing the gas-membrane boundary. This approach has been used in the past to link the membrane water content in equilibrium with the vapour pressure in the surroundings, where the environment provides a homogeneous activity with no external driving force. Therefore, the use of isothermal data is not appropriate for a non-equilibrated gas-membrane interface.

The main differences with the VDC model lie, first, on the dependency on water content for the bulk diffusivity that the VEM lacks. A second difference lies on the

physical description of the dynamic membrane-gas interface occurring in the experiment, contrarily to the assumed equilibrium the VDC model considered. The VEM, instead, assumed a flux boundary where evaporation and condensation across the gas-membrane interface occurred indistinctly as a function of the gas flow. The vapour accumulation in the chamber was expressed mathematically as a mass balance in time domain leading to a steady state at long times. This flux boundary represents the effect of the gas flow velocity where the flux direction is a function of the flowing gas velocity in the dry chamber. Fitting to this model with steady state water transport data revealed values the interfacial water transport rates, k_v. Using transient water transport data, values for the bulk permeability component were determined: the diffusivity coefficient D, and the maximum water concentration for liquid- and vapour-equilibrated membranes: $c_{\max}^{L}$ and $c_{\max}^{V}$, respectively.

The VEM incorporated a term for bulk diffusion and water evaporation and condensation across the gas-membrane surface represented in the overall water balance:

$$\frac{V}{RT}\frac{dp_{w,out}}{dt} = \left[p_{w,in} - p_{w,out}(t)\right]\frac{\dot{V}}{RT} + AJ(t) \tag{5.3}$$

Within the membrane, the transport of water was described by Fick's law. The water flux across the membrane-gas interface is given by:

$$J(t) = -D\left.\frac{\partial c}{\partial z}\right|_{t,L} \tag{5.4}$$

Liquid-equilibrated membranes

The LE case describes the membrane in contact, one surface, with liquid water, and the other surface exposed to the flowing gas. Since the model describes the transient transport in the gated cell, initial conditions are describes as:

$$p_{out}(0) = p_{in} \quad \text{and} \quad c(0,z) = c_0 \tag{5.5}$$

After the gate is opened the concentration at the membrane-water interface is defined by the boundary condition:

$$c(t,0) = c_{\max}^{L} \tag{5.6}$$

The boundary condition at the membrane-gas interface was described as follows:

$$-D\frac{\partial c}{\partial z}\Big|_{t,L} = \frac{k_v}{RT}\left[p_{eq}(c(t,L)) - p_{out}\right], \tag{5.7}$$

where D, refers to the Fick's diffusion coefficient for the internal transport, and k_v represents the rate of mass transfer across the interface. Equation (5.7) represents the flux across the interface. The equilibrium vapour pressure, p_{eq}, is linked to the water content $c(t,L)$ (in z=L) according to the vapour sorption isotherm.

Vaporization and condensation are represented by the last term on the right. This term refers to an activated process controlled by Gibbs free energy of water sorption, which determines $p_{eq}(c(t,L))$. Condensation is a purely kinetic process with a rate proportional to the actual vapour pressure p_{out}.

For the model, the description of p_{eq} is reduced to a simplified version of the equilibrium vapour sorption from isothermal measurements to a linear relationship:

$$p_{eq}(c(t,L)) \approx \frac{p_{sat}}{c_{\max}^{liq}} c(t,L), \tag{5.8}$$

This expression of Henry's law assumes a constant proportionality coefficient independent of the membrane water content to make governing equations easier to solve analytically. The formulation of the governing system and its solution is presented in detail in Appendix F.

Vapour-equilibrated membranes

The main differences when describing VE is the definition of the water concentration at the membrane-vapour interface (in z= 0), in this case: $c_{\max}^{vap}$, which replaces $c_{\max}^{liq}$; and the new boundary condition (at z=L) described by:

$$-D\frac{\partial c}{\partial z}\Big|_{t,0} = \frac{k_v}{RT}\left[p_{sat} - p_{eq}(c(t,L))\right] \approx \frac{k_v p_{sat}}{RT}\left[1 - \frac{c(t,0)}{c_{\max}^{vap}}\right] \tag{5.9}$$

5.2.2 Application of the VEM to steady state water transport data

Solutions to the governing equations system (See Appendix F) are summarized in Table 5.2

Table 5.2 . Steady state response from analysis with VEM

	Slope of linear: *(1-RH)/RH vs.* $\frac{\dot{V}}{A}$	
LE	$m_{LE} = \frac{1}{k_v} + \frac{p_{sat}}{RTDc_{\max}^{L}} L$	(5.10)
VE	$m_{VE} = \frac{2}{k_v} + \frac{p_{sat}}{RTDc_{\max}^{V}} L$	(5.11)

From our LE steady state water transport measurements, the vapour pressure data were plotted as: *ln (1-RH/RH) vs. gas flow velocity,* for Nafion of different thickness, as shown in Figure 5.3.

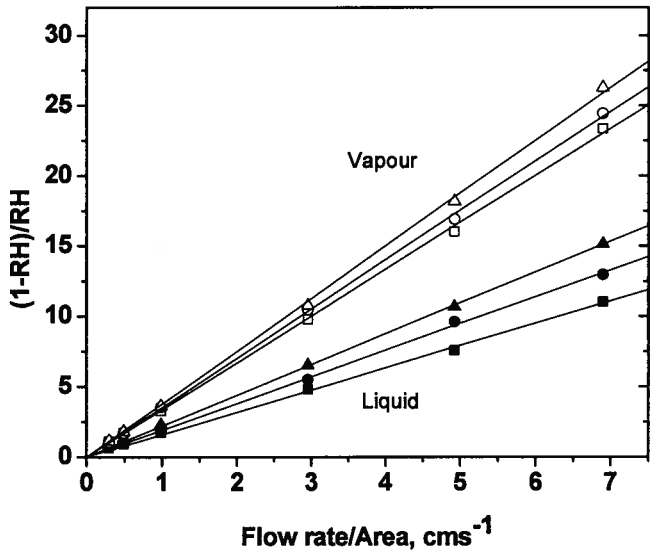

Figure 5.3. Measurements of (1-RH)/RH as a function of the gas velocity show a good fitting with the VE model.

The slopes obtained from the fitting lines in Figure 5.3 were plotted against the thickness variation of Nafion membranes, as shown in Figure 5.4.

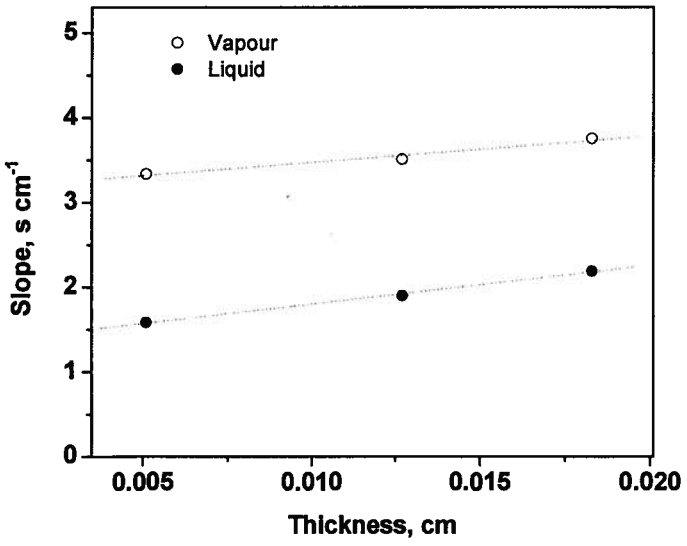

Figure 5.4. Linear fits of the slopes from Figure 5.3 *vs.* Nafion 11*x* thickness in Liquid and Vapour equilibrated membranes.

The graph, *slope vs. thickness*, in Figure 5.4 showed a good linear approximation between the three thicknesses data (R^2=0.96 for VE , and R^2=0.99 for LE). Through the intercept and slope of the LE line, values for the bulk permeability component: Dc_{max}, and the interfacial mass transfer: k_v were obtained provided that they fulfilled Equation (5.10). The same approach was followed with the slope and intercept of the VE linear fit of Figure 5.4 The values of k_v and Dc_{max} were obtained for vapour equilibrated Nafion through Equation (5.11).

The mass transfer and diffusivity coefficients values found for Nafion are summarized in Table 5.3. Results of k_v for LE and VE showed similar rates. This counters the expectation of a higher permeability for LE membranes. However, it is rational to conclude that the vaporization-exchange rate is similar for LE and VE membranes if the main sources of error along the analysis are considered: the error in the linear fit can be as high as 20%, membrane swelling can produce a thickness variation of up to 8% in thickness, and the neglect of the energy balance adds in a 25% error in k_v. Therefore, these results can be considered a qualitative verification of the vaporization-exchange model. More analysis and variation of more membrane thicknesses are needed to obtain quantitative results.

Table 5.3. Bulk permeability Dc_{max} and interfacial k_v of Nafion in LE and VE Nafion at 50°C.

Nafion	k_v* (ms^{-1}) x 10^3	Dc_{max} ($molm^{-1}s^{-1}$) x 10^5
LE	7.5	1.0
VE	6.3	1.5

* The estimated error for k_v ranges in ± 23% according to the thermal losses effects from Section 3.3.2.

Current models in the literature have not been able to identify individual values for D and c_{max} from water transport measurements [19,62,78,81]. Some authors, [78,81] used water concentration from isothermal data and Fick's law analysis for determining D. Motupally's model [19] used self diffusion coefficients from NMR measurements and isothermal data to calculate water fluxes. Similar to the VEM, Majztrik and collaborators found a range value of 18-39 $x10^{-5}$ $molm^{-1}s^{-1}$ for the permeability, Dc, component which related diffusivity and what the authors assumed an equilibrium water concentration in the membrane. The main difference with the values obtained in this work: 1-1.5 $x10^{-5}$ $molm^{-1}s^{-1}$ (Table 5.3) lies on the erroneous assumption of an equilibrium between the membrane and the surrounding of Majztrik et al. approach, they did not include the effect from the adjacent gas on the water content of the membrane, as the VEM did. In addition, their model was not able to separate the product into individual values for D and c.

In the following section, the application of the Vaporization-Exchange model to the LE transient water transport data is described. It shows a successful procedure to determine the individual values for D, and corresponding maximum water concentration, $c_{\max}^{L}$ in the membrane.

5.2.3 Fitting the vaporization-exchange model to transient water transport data

The measured transient water transport data were analyzed with the solutions proposed for the VEM. A pair of transformed Laplace equations accounted for the solution to the long- and short-time water transport measurements. Based on an iterative solution with both equations, values for D and $c_{\max}^{L}$ were individually determined.

Transient measurements from Nafion 117 in LE were used for the analysis. The initial experimental conditions described an initially dry concentration for the membrane: $\theta_m(0,\xi)=0$; and zero vapour pressure in the gas chamber: $\theta_v(0)=0$.

Boundary conditions outlined a relative humidity gradient across the membrane: on the wet side, saturation was fixed as constant. On the dry side, the dynamic vaporization-condensation regime described a flux across the interface.

Assuming an initially dry membrane, ($\psi=0$), the long- time solution expression was simplified to:

$$\lim_{\tau>>1}\frac{\theta(\tau)}{\theta^{\infty}}=1-e^{-k_1\tau}, \tag{5.12}$$

and for the short-time, the simplification led to

$$\lim_{\tau<<1}\theta(\tau)=\gamma\left[(1+2\tau)\ erfc\left(\frac{1}{\sqrt{4\tau}}\right)-\sqrt{\frac{4\tau}{\pi}}\exp\left(-\frac{1}{4\tau}\right)\right] \tag{5.13}$$

Solving Equation (5.12), the slope of the fitted line of the curve of *ln(1-RH(t)/RH(ss)) vs. time* in the long-time data generated the value for the exponential decay, k_1. See Figure 5.5.

Figure 5.5 is a representative set of data for Nafion 117 and its corresponding linear fit in the long-time range. Similarly, the lineal fit was done for the data at 30, 50 and 70°C. The line adjustment was kept conservatively below 400s, since all experiments showed steady state below 300s. Moreover, the data dispersion became significant above 400s.

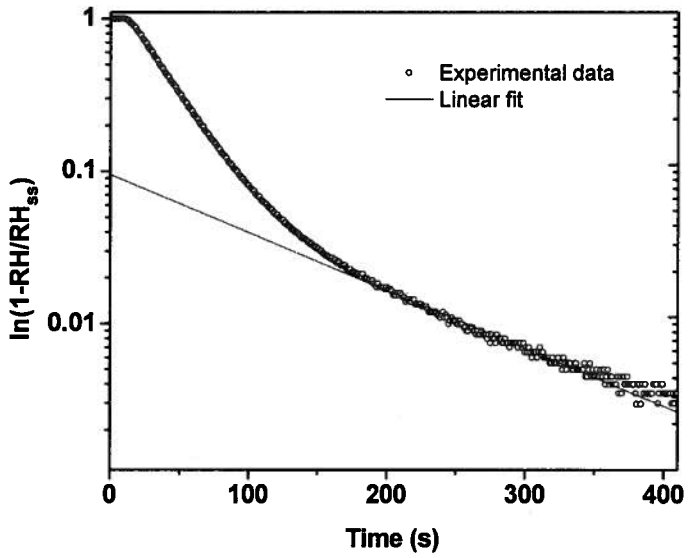

Figure 5.5. Representative linear fit of long-time response. LE Nafion 117.

From the fitted line, the slope was equivalent to k_1, which corresponds to the exponential term in Equation 5.12 and it is defined by Equation. 5.14. With k_1, the first approximation for D was calculated:

$$k_1 = \left[\frac{1}{6} + \frac{1}{3}\left(1 + \frac{V}{k_v A}\right) RH(ss) + \frac{DV}{L^2 V}\left(1 - RH(ss)\right)\right]^{-1} \quad (5.14)$$

Using Dc_{max} from steady state (Table 5.3), preliminary individual values for D and c_{max}^{L} in the long term were calculated. These were used to simulate the short-time response with Equation (5.15). Assuming an initial dry condition for the membrane ($\psi = 0$), the equation for the short-time is reduced to:

$$\lim_{\tau \ll 1} \theta(\tau) = \gamma\left[(1+2\tau)\ erfc\left(\frac{1}{\sqrt{4\tau}}\right) - \sqrt{\frac{4\tau}{\pi}} \exp\left(-\frac{1}{4\tau}\right)\right] \quad (5.15)$$

Comparison of the simulated and experimental short time data is shown in Figure 5.6.

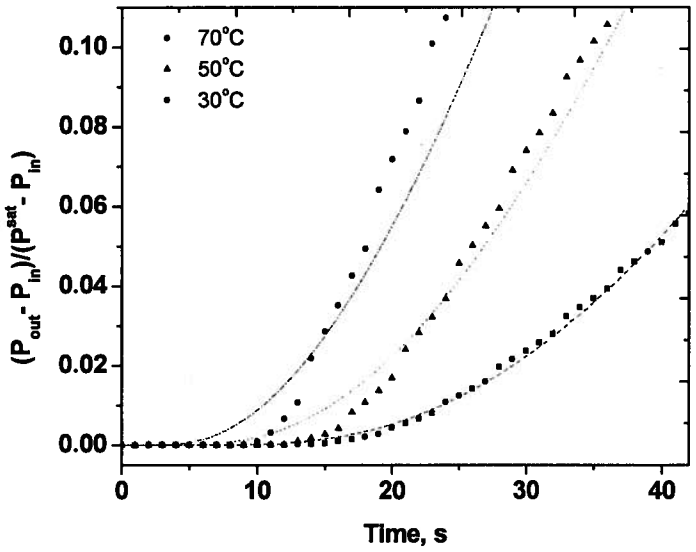

Figure 5.6. Simulation (lines) and experimental (dots) data in the short-time for LE Nafion 117 at 30, 50, and 70°C.

Final D and c_{max}^{L} were obtained from the best fit between simulation and experimental data in the short time response. The same procedure was applied for Nafion

117 data under 30, 50 and 70°C. Table 5.4 shows the results and the corresponding dimensionless vaporization rate, γ. The values for diffusion coefficient compared closely to reports from the literature for liquid equilibrated membranes. However, it is worth to mention that the dependency on water content for the diffusivity coefficient has not been addressed in this work; therefore, comparison is only applicable to the limiting case of a fully saturated membrane with water content ranging 22 mol/SO_3^-.

For the analysis of the maximum water concentration in the membrane, c^L_{max}, was reported in accordance with fully saturated membranes presenting values below 55 M, as shown in Table 5.4. This agrees with the concept of a fully saturated membrane region assumed to be close to the liquid-membrane interface. Values for γ confirmed that interfacial mass transfer rates become significant with temperature increasing.

Table 5.4. Summary of diffusivity coefficient (D), water concentration in the membrane (c^L_{max}) and the corresponding dimensionless vaporization rate (γ).

Temperature °C	Liquid Equilibrated Membrane Type	D x 10^{10} m^2s^{-1}	c^L_{max} mol L^{-1}	γ
		Nafion 117		
30	N115	2.0537	48.69	1.957
50	N115	3.7649	26.56	1.067
70	N115	6.6815	14.97	0.601
From literature at 30°C:				
Authors	Type	D x 10^{10} m^2s^{-1}	Technique	
Yeo and Eisenberg	N1155	2.1	Water Uptake	
Zawodzinski et al.	N117	7.5	NMR	
Suresh et al.	N117	1.8-2.2	Tritium Tagged Water	
Fuller	N117	1.4	Steady State Permeation	

The Arrhenius-dependency for diffusion coefficients from Table 5.4 showed activation energy of 24 $kJmol^{-1}$. This value compared similar to the activation energy (25–31 $kJmol^{-1}$) found from desorption experiments [77], but lower (ca. 50%) than the activation energy calculated from steady state measurements (see Section 4.1.1). The transient water transport data are the result of the driving force effect of a large water concentration gradient. The water concentration profile, at the moment of lifting the gate-valve, can be outlined as a steep slope between the two membrane surfaces, one of which is in contact with liquid water, and the opposite in contact with dry gas, is in severe dehydration. The influence of this extreme water concentration gradient acting as driving force, could explain the reduced energy demand for water transport in the short time.

6. A case study: Water transport dependency on membrane water content

This chapter investigates the relation between membrane water content and its transport properties by means of comparing pristine Nafion membranes with modified composite Nafion membranes. Results from Nafion115 and Nafion115/SiO_2 composite membranes were compared for water transport, vapour sorption and desorption, and differential scanning calorimetry. The hygroscopic properties of SiO_2 increased the water uptake capacity of the membrane, and with it, its water transport properties were investigated. Results presented here are preliminary for an in-process journal publication

This section of the thesis explored the effects of the water content over the transport properties of modified Nafion. We used Nafion membranes modified with SiO_2 nanoparticles to investigate how the addition of hygroscopic silica influences the water uptake and the membrane transport properties.

Nafion 115-SiO_2 membranes with 10, 16 and 33 wt% of SiO_2 , prepared at NRC-IFCI by M. Rodgers [45], were compared with unmodified Nafion 115 by measurements of:

a) steady state water transport at 80°C in liquid-gas and vapour-gas equilibrium

b) vapour water sorption and desorption at 25°C from 0 to 95% RH, and

c) differential scanning calorimetry in liquid saturated membranes at 25°C.

6.1 Water content measurements from full saturation with liquid

Membrane samples were fully immersed in liquid water at room temperature. Results from water uptake and thickness change measurements for Nafion 115 and Nafion115/SiO_2 composite membranes are included in Table 6.1. The data from this work and from [45] correspond to membranes from the same batch prepared by M. Rodgers.

Table 6.1 Properties of Nafion 115/SiO_2 composite membranes.

SiO_2 wt %	Dry Membrane Thickness, mm	Liquid equilibrated Membrane[b] Thickness Gain,%		Water Content, wt%	
	[45]	[45]	This work	[45]	This work
0[a]	0.132	14	16	23	23.7
10	0.15	12	11	25	20.5
16	0.142	8.9	15	28	26
33	0.171	8	13	28	26

[a] Unmodified Nafion 115; [b] under 25 °C

Table 6.1 includes in the first column the thickness measurements of the dry samples. The results confirm that the addition of SiO_2 increased the membrane thickness. On the second set of columns, the data shows the results from thickness gain (%) and water content (wt%) of the samples under liquid saturation. On the one hand, it was found that the thickness gain decreased with the increase of silica, which suggests that the addition of SiO_2 lowered the membrane swelling capacity. On the other hand, the water content increase stopped at 16 wt% SiO_2, which implies that the easiness to absorb water provided by the early addition of silica was counterbalanced after 16 wt% SiO_2.

In the measurements of Young's modulus with membranes from the same batch as those used here, Rodgers [45] found that the membrane became stiff with addition of SiO_2 (from 0 to 33 wt%). The explanation for a membrane switch to a rigid configuration

was explained by the theory of scaffolding formation proposed by Yang [103] and Rodgers [45] in composite membranes. Young's modulus measurements have confirmed that below 10 wt% SiO_2 the membranes maintain the same flexibility as that for unmodified Nafion [104]. It can be explained that the scaffolding occurred somewhere after 10wt % of SiO_2 and this is what caused swelling stoppage and water uptake increase at 16 wt % of SiO_2 in the present study.

6.2 Water Content from Vapour Water Sorption and Desorption

Isotherms from sorption and desorption experiments were obtained at 25°C from 0 to 0.95 activity using the DVS procedure (Section 3.4). Figure 6.1 shows the water content for the membrane series including pristine Nafion 115 and Nafion 115/SiO_2 from 10, 16, and 33 wt% SiO_2.

The water content of composite membranes increased with increasing water activity, in the same way as that for the unmodified Nafion (0%). Similar dependency was found for Nafion/SiO_2 at 90°C [105]. In terms of the amount of water uptake, at 120°C, Miyake et al. found the unmodified Nafion showed noticeable lower water uptake than silica-modified-Nafion [87]; below 90°C, the water content difference was slightly higher for the composite than the pure Nafion, agreeing with the results at 25°C presented here.

In the sorption isotherm, Figure 6.1(a), the water content of composite membranes presented higher values than unmodified Nafion 115, with the highest value for 16 wt% of silica. A similar trend was found with water content data measured in liquid equilibrated membranes (Section 4.5.4). However, Miyake et al. [87] concluded that for

composite membranes prepared with Nafion 117, with 5 to 26 wt% content of silica, the isothermal sorption presented the same water content to unmodified Nafion at 25°C. This discrepancy may be explained by the thickness difference between Nafion 115 (this work) and Nafion 117 if we consider that the thickness increase with Nafion 117 can be translated into a water transport mechanism dominated by the bulk. We described already that higher membrane thickness decreases the flux crossover (section 4.1.4).

Desorption isotherms, in Figure 6.1(b), show the membrane water content driven from a saturated condition to a dry environment. The graph is presented from low to high activities to facilitate the comparison with the sorption graph. Better water retention was observed for unmodified Nafion 115 compared to composite membranes between 0 to 0.7 water activity. The presence of silicon dioxide slightly reduced the water retention capacity compared to unmodified Nafion in the low and intermediate activity range. Desorption of water from composite membranes has been described as a temperature dependant process [104] requiring higher temperatures to desorb the bound water. Further testing is required to confirm that higher temperatures would improve desorption of water from composite membranes over unfilled Nafion.

(a)

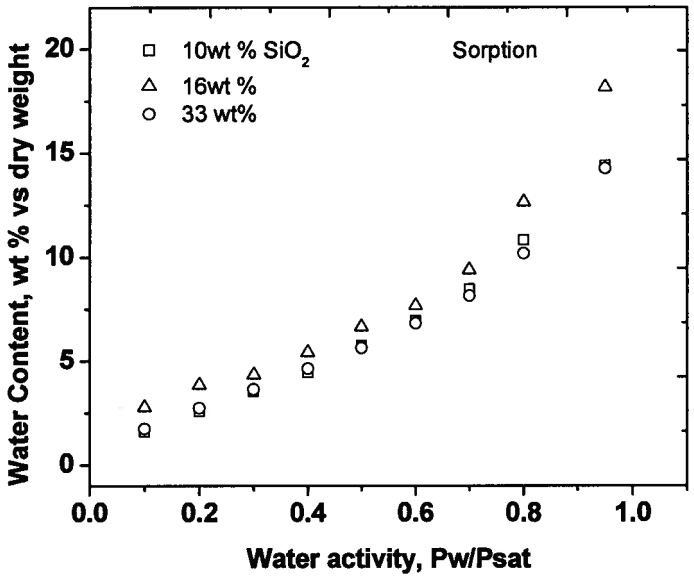

(b)

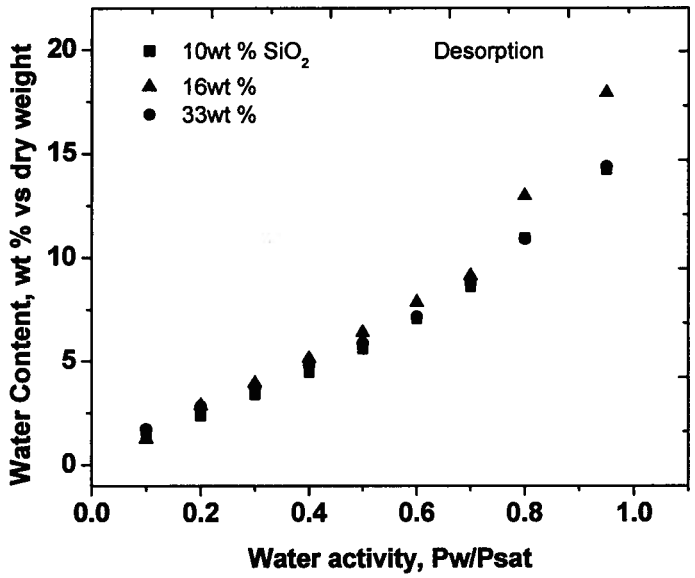

Figure 6.1. Vapour water isotherms for Nafion 115/SiO_2 composite membranes at 25°C for (a) sorption, and (b) desorption.

Transient records from isothermal measurements were used to calculate the rate of sorption and desorption for each membrane sample. Figure 6.2 compares the derivatives of the mass variation with respect to time *vs.* the water activity. In both cases, sorption and desorption, the rate of change from unmodified Nafion showed a constant rate (1.3 $x10^{-4}$ mgs^{-1}) with the increasing activity. Contrarily, composite Nafion showed an increasing rate of sorption (Figure 6.2a) with addition of silica that was exacerbated at 0.8 activity. On the desorption graph (Figure 6.2b), the rate of change for composite and unmodified Nafion presented a similar value (1 $x10^{-4}$ mgs^{-1}) in the range 0.1 to 0.7 activity, but a threshold occurred at 0.8 activity, from where the composite Nafion increased the transport rate with the addition of silica. The desorption rate for composite membranes was higher (ca. 2x) than for sorption. Contrarily, the unmodified Nafion membrane showed a constant rate for sorption and desorption along the activity variation.

(a)

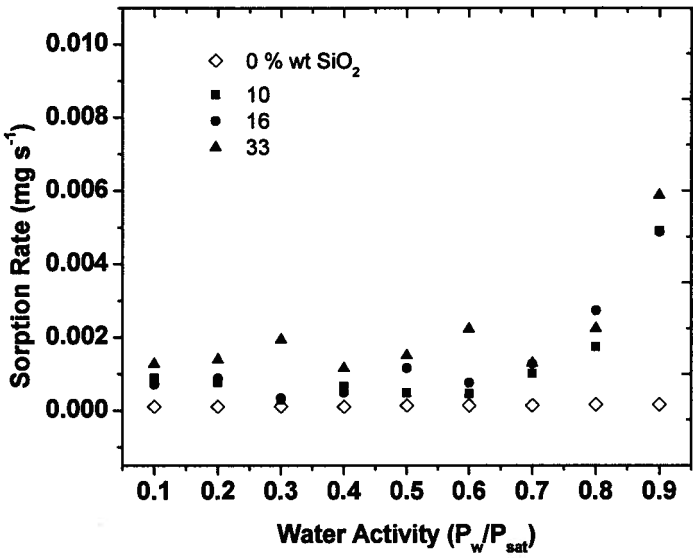

(b)

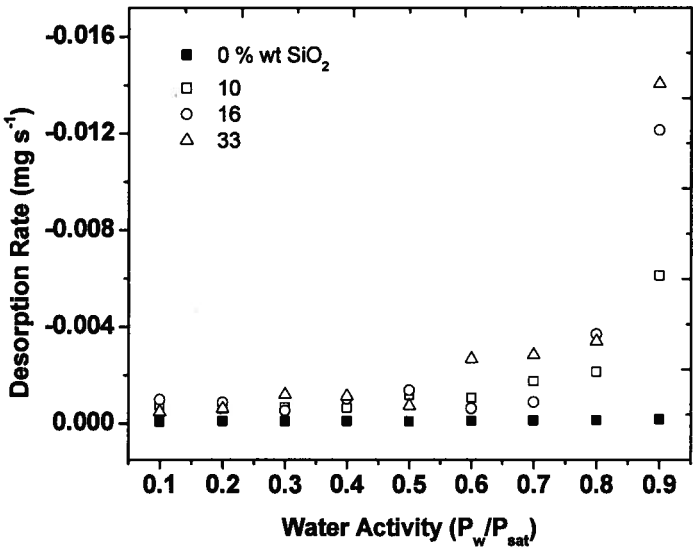

Figure 6.2. Rate of change for sorption (a) and desorption (b) of vapour water in unmodified Nafion 115 and composite N115/SiO_2 membranes.

6.3 State of Water in Liquid Saturated Membranes

The state of water in liquid saturated membranes was characterized by thermal calorimetry using the technique described in Section 3.5.2. The water content in the membrane was classified as bound and non-bound according to its endothermic and exothermic energy when it was subjected to a temperature scan.

Figure 6.3 shows the change of water with the addition of SiO_2 to Nafion membranes for total, bound, and non-bound water. Continuous lines show the data for composite membranes with SiO_2 wt% variation. The error bars have the same value for bound and non-bound water because the water content ratio is derived from their difference with respect to the total water. Independent symbols on the left correspond to unmodified Nafion 115 data.

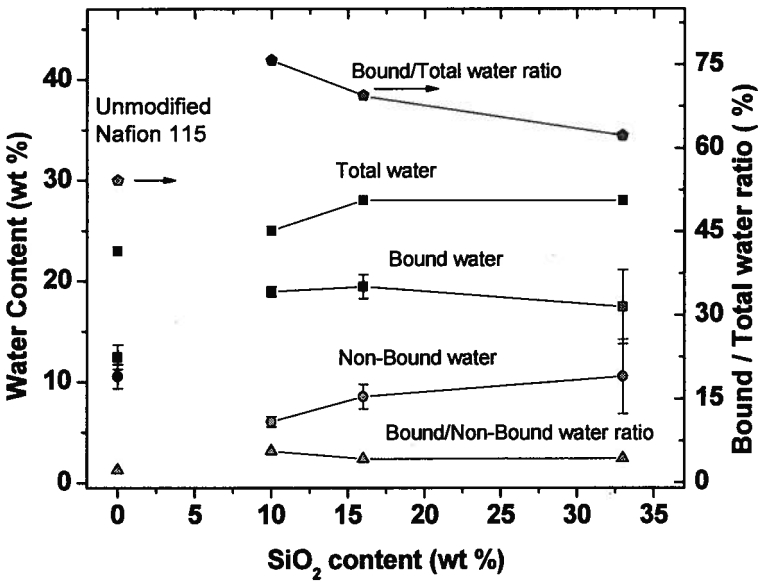

Figure 6.3. The state of water as a function of SiO_2 content in Nafion 115 membranes. Data at 0 wt% corresponds to unmodified Nafion.

The bound to total water ratio decreased with increasing silica content from 10 to 33 wt%. However, at 0 wt%, the corresponding value for unmodified Nafion membrane was low compared to the composite membranes. The bound water showed a maximum at 16 SiO_2 wt % and decreased with SiO_2 wt% increasing. Conversely, the non-bound, or free-water presented an upward trend with the addition of silica.

These results indicate, that on the one hand, the membrane total water content is enhanced by the addition of silica, but it is limited by probable scaffolding formation, and on the other hand, that the bound water switches to bulk type water with the further addition of SiO_2. This suggests a change in microstructure in the polymer morphology at 16 SiO_2 wt%.

Summarizing the previous results, it was found that the membrane increased water content with silica addition but it reduced its ability to swell, indicating that nanoparticles may occupy interstitial spaces between ionic clusters. From 0 to 16 SiO_2 wt %, the water content increased; but stayed constant with further silica content. The 16 SiO_2 wt% content marked a possible change in the material morphology. This is supported by the observations from the vapour sorption measurements, pointing to a more hydrophilic membrane at 16 SiO_2 wt%. Calorimetry results suggest that the addition of silica may cause some structural changes in the cluster domain of water liberating water molecules with the further addition of silica. Addition of silicon dioxide to Nafion was analyzed with water transport under steady state conditions. The following section describes preliminary results with the permeability cell.

6.4 Steady State Water Transport in Nafion 115/SiO_2 Composite Membranes

The water transport across membrane samples for Nafion 115-SiO_2 and unfilled Nafion 115 was examined under steady state conditions at 80°C. This selected temperature was considered to be a balance between the operational temperatures of PEMFCs and the limits of the test rig accuracy.

Figure 6.4 shows the crossover flux as a function of the gas flow rate for VE and LE membranes. Similarly to unmodified Nafion (section 4.1.1), silica composite membranes' fluxes responded with an increase regarding the driving force applied (i.e., gas flow rate) in the low range. At higher flow rates, LE membranes showed higher fluxes than VE.

Comparing the fluxes obtained from Nafion 115 at 80°C in Section 4.1.1, we found the value of the flux to be dependent upon the type of sweeping gas used. In the analysis of composite membranes, Nitrogen was used as the carrier gas instead of Helium. It was found that Nitrogen generated lower dew point temperature data than Helium. Further analysis is required in this area, but a possible explanation is that due to the heavier molecule weight, Nitrogen reduced the mixing time between gas and vapour in the dry chamber, thus affecting the dew point temperature measurements.

Figure 6.4a shows the vapour transport flux. Along the activity gradient (i.e., Nitrogen flow rate), the fluxes for the composite membranes were comparable with unfilled Nafion. The fluxes increased with the gas flow in the low regime, and decreased at higher driving forces. This flux decay is explained by a faster evaporation threshold at higher flows. The composite membranes behaved similarly to unfilled Nafion that neither prevented dehydration of the membrane surface at higher gas velocities.

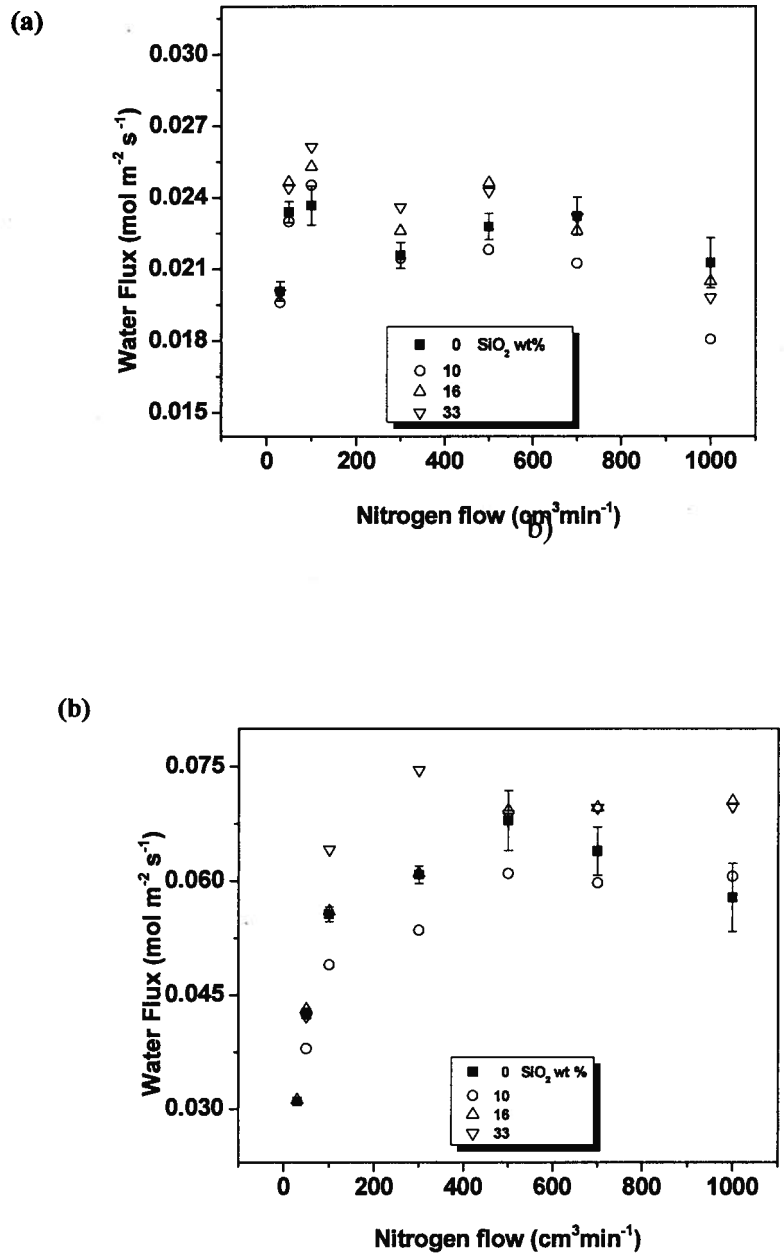

Figure 6.4. Steady state water transport fluxes in unmodified Nafion 115 (0 wt% SiO_2), and Nafion/SiO_2 composite membranes with 10, 16 and 33 wt % SiO_2, at 80°C; a) in VE, and b) LE conditions.

Composite membranes from the same batch as the one previously analyzed for vapour-vapour-transmission by M. Rodgers [45], showed no difference in performance between samples, from 0 to 33 wt% SiO_2, under a 0.6 activity gradient (the nature of those experiments did not allow the specification of the sweeping gas flow rate used). The activity gradient was calculated in a similar fashion as explained in Section 3.2.1. The activity at the wet side is considered 1, and the activity at the dry side, is calculated from the environment vapour pressure and saturation pressure ratio, as described by Equation 3.5 and 3.6. The vapour transmission rate calculated from Rodger's experiments ranged from 0.024 to 0.031 $molm^{-2}s^{-1}$. This rate agreed with our flux range found in our vapour-gas WT experiments, within 0.018 to 0.026 $molm^{-2}s^{-1}$.

The graph for LE membranes, in Figure 6.4b, shows an increased flux with the addition of silicon dioxide. The transport flux under high activity (gas flow above 500 $cm^3\ min^{-1}$) for 16 and 33 silica wt% composite membranes exceeded Nafion's transport fluxes.

Figure 6.5 compares the flux vs. membrane thickness for the two sets: composite membranes with 0, 10, 16, and 33 wt % SiO_2; and unmodified Nafion with Nafion 112, Nafion 115 and Nafion 117. The graph shows a decreasing trend for unmodified Nafion membranes with increasing thickness. On the contrary, composite membranes showed little variation with the thickness.

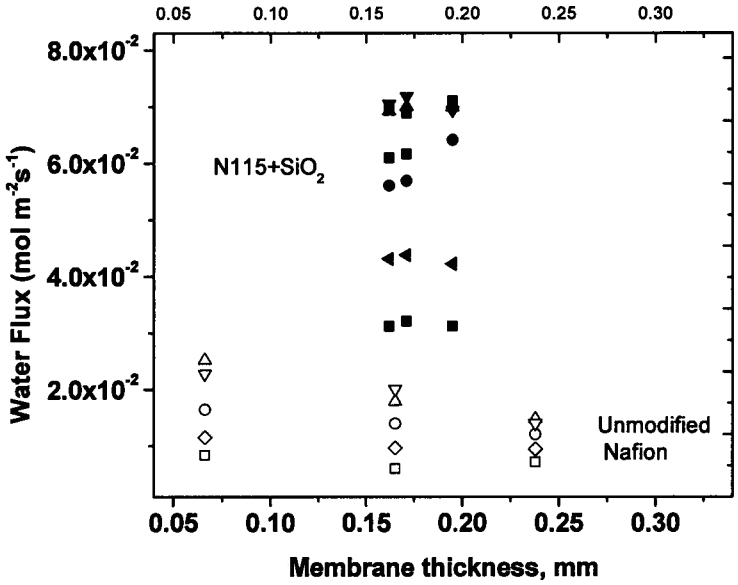

Figure 6.5. Thickness dependency for steady state water transport across Nafion/SiO_2 composite membranes (solid symbols) and unmodified Nafion 115 (hollow symbols) at 80°C and 50°C, respectively, measured in liquid equilibrated samples. The varying symbols (squares to triangles) correspond to increasing gas flow rate from 30 to 1000 cm^3min^{-1}.

The comparison between Nafion and composite membranes suggest a material transport property change caused by the addition of SiO_2. The difference in the scale between fluxes for composite and unmodified membranes in Figure 6.5 is due to the difference in testing temperature, 80 and 50°C, accordingly.

It is assumed that the addition of silicon dioxide produces structural changes in the membrane, creating and maintaining better connected pathways, facilitating the transport across the bulk. To understand how this improved performance may be related to surface or bulk phenomena we applied the Vaporization-Exchange Model to determine the values of the interfacial mass transfer coefficient and bulk permeability. The following section describes the analysis.

6.5 Analysis of Composite Nafion Membranes using the VEM.

Using the vapour pressure data from the WT measurements and thickness records from the addition of SiO_2, the Vaporization-Exchange Model was applied following a similar procedure to that explained in Section 5.2.2.

From vapour pressure data measured at 80°C, the relative humidity ratio (*(1-RH)/RH*) was calculated for unmodified Nafion 115, and composite N115/SiO_2 in LE and VE samples. Figure 6.6 shows the linear fit from the vapour and liquid water transport measurements.

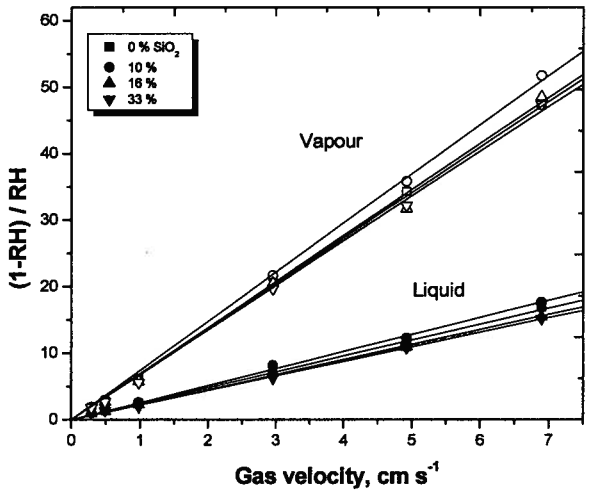

Figure 6.6. Fitting lines for measured (1-RH)/RH data *vs.* gas velocity for composite/Nafion 115 membranes with 0, 10, 16 and 33% SiO_2, and Nafion 115 (0% SiO_2).

The slopes of the straight lines obtained from Figure 6.6 were used to graph Figure 6.7 The slopes *vs.* the SiO_2 wt% content are shown for VE and LE. In VE and LE, the slopes showed little variability with the increase of silica content. The averaged slope value for VE appears higher (ca. 200%) than its counterpart in LE. This difference points to a higher resistance to water transport for VE than for LE membranes, but gives no insight about the effect on the mechanisms of water transport with the addition of silica.

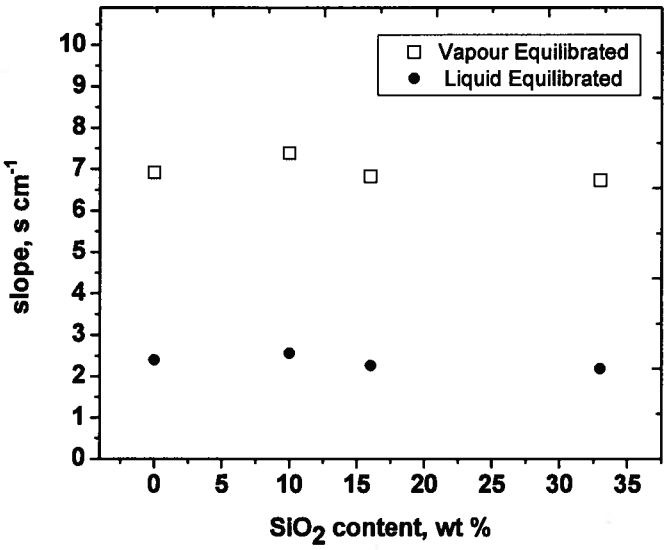

Figure 6.7. The slopes from Figure 6.6 are plotted against the content of SiO_2 wt% for LE and VE composite Nafion membranes.

Based on the resistance in series model, the slope represents the sum of the individual water transport mechanisms (i.e., resistances) across the membrane, and it is equal to the total resistance according to the analogy of resistance in series analogy. The Equation 2.11 is rewritten for LE and VE as:

$$m_{VE} = \sum \text{resistance} = \left|\frac{1}{k_v}\right|_{(1)} + \left|\frac{1}{k_v}\right|_{(2)} + \left|\frac{L}{D}\right|_{(3)}$$

$$m_{LE} = \sum \text{resistance} = \left|\frac{1}{k_v}\right|_{(1)} + |0|_{(2)} + \left|\frac{L}{D}\right|_{(3)} \qquad \textbf{(6.1)}$$

According to the proposed analogy, the individual resistances are described in Table 6.2:

Table 6.2 Descriptors of Equation 6.1 components

Individual Resistance	Description
$\left\|\frac{1}{k_v}\right\|_{(1)}$	kinetic resistance at membrane/gas interface
$\left\|\frac{1}{k_v}\right\|_{(2)}$	kinetic resistance at the membrane/stagnant fluid interface
$\left\|\frac{L}{D}\right\|_{(3)}$	bulk resistance

For composite Nafion membranes, L, and D are expected to be a function of the SiO_2 wt% content.

Any quantitative conclusion for the transport resistances would be speculation. It was expected that the slope would provide information on the effect of silica addition in the increase/reduction of resistance to water transport. However, the slopes for VE and LE in Figure 6.7, shows no visible effect on the net total resistance with the addition of silica. This contradicts the observations from water transport and water uptake characterization, where it was found that the silica content enhances both overall mechanisms.

This suggests that the VEM is not able to represent the polymer structural changes originated in the Nafion membrane by the silica addition. In order to characterize PEM membranes with the VEM, the model will need to include the change in morphology due to the increased water content promoted by the SiO_2.

6.6 Polymer Structure and Water Transport in PEM.

The water transport investigations carried out for this thesis highlighted the importance of interfacial kinetics in the water transport studies, and also revealed that membrane water content and its interaction with the polymer structure influence the mechanisms of water transport. Therefore, further experimental and modeling work are required to define the dependence of water transport on polymer structure. A proposed approach is described below.

Figure 6.8 shows the water content profile across a LE and VE membrane during steady state water transport experiments. Bear in mind that a normalized parameter that encloses physical and environmental parameters is in need to describe the effective transport driving force. In the LE case (left), the wet surface shows a higher water penetration; meanwhile, in the VE (right) membrane, the wet surface shows higher water transport resistance with a thinner water penetration layer.

Regions with varying water concentration were outlined in both cases. These regions differentiate water saturation levels within the bulk due to the water activity gradient created by the flowing gas on one surface, and the stagnant fluid in contact with the opposite surface. Within these regions, the mechanisms of water transport can be assumed to be different from each other. This assumption is valid under the basis of Weber and Newman model [55] of polymer structural variations as a function of water content (described in Figure 2.2, section 2.1). In regions of low water concentration (thickness=L-d), it is assumed that water is transported via diffusion through a structure of low porosity (corresponding to low water content $\lambda<14$). Contrarily, water transport in

highly saturated regions (thickness=*d*) is assumed to occur via hydraulic permeation through an expanded channels structure based on the continuous pore-like structure described by Weber an Newman. Quantification of diffusivity coefficients in the membrane bulk reported by Volino and Diat [106] have shown that water diffusivity in saturated membranes, of $\lambda>10$, show similar values to the bulk water diffusivity.

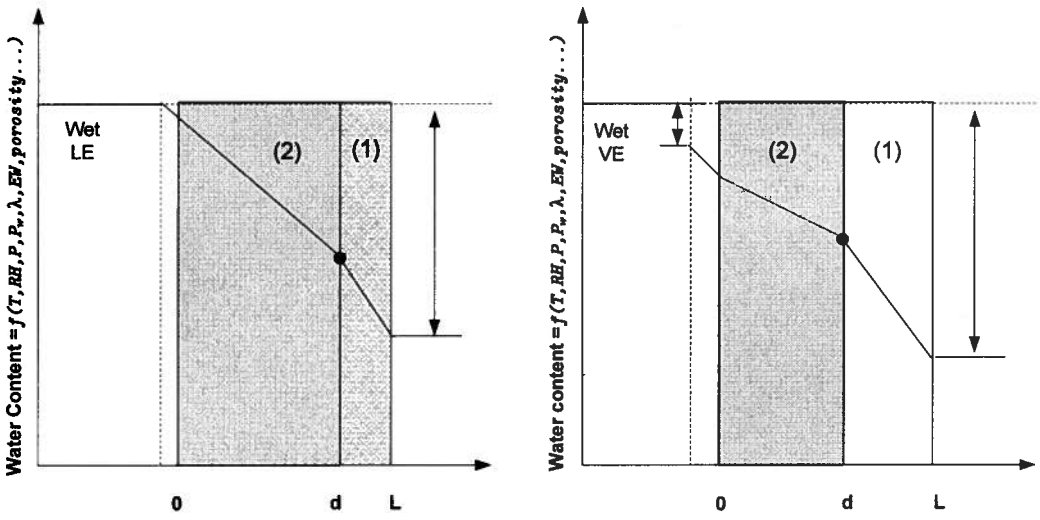

Figure 6.8. A one-dimensional, steady state approximation with continuous water concentration profiles inside the bulk and across the interface. The profile inside the bulk shows discontinuity due to dehydration of the top layer close to the membrane-gas interface. The profile across the water-membrane interface shows continuity across the LE interface (left), and discontinuity on the VE interface (right).

Figure 6.8 also describes water content profiles across the interfaces. For LE (left), the membrane-stagnant fluid interface is represented with a continuous profile. Contrarily, for VE membranes (right), the interface is considered to show discontinuity. This is based on the lower water uptake for VE membranes reported elsewhere [11,56], and from permeability measurements with VE membranes presented in this work.

According to the resistance in series analogy for water transport, it is likely that the resistances within the bulk can be represented as a function of the water content, according to:

$$\sum \text{resistance} = \frac{1}{k_v} + \frac{1}{k_v} + \frac{L-d}{D(1)} + \frac{d}{D(2)} \tag{6.2}$$

where *D(1)* and *D(2)* will depend on the lower and higher water content regions, respectively.

7. Conclusions and Recommendations

7.1 Conclusions

A comprehensive experimental study on water transport phenomena was carried out on proton exchange membranes under activity gradients in steady state and transient regimes. Experiments looked for evidence on the importance of interfacial processes in controlling the overall water transport.

Experimental conditions were kept in accordance with typical conditions of membranes in PEM fuel cells without the incorporation of electric work, i.e., passive condition.

A dual chamber cell was designed to measure water transport across membranes with independent control of temperature, pressure, relative humidity, composition, and gas flow rate. The cell's novel feature was a gated-valve to allow reproducibility of transient water transport measurements across the membrane.

Experimental results, from steady state water transport measurements, showed that vapour-membrane interfaces are more resistive than their liquid-membrane counterparts. The water fluxes observed in LE membranes were roughly 2x higher than their VE counterparts. Non-isothermal experiments supported the assumption that exacerbated membrane dehydration acts as a barrier to water transport.

Transient water transport data motivated the design of two phenomenological models, the Varying Diffusion Coefficient model (VDC) and the Vaporization Exchange Model (VEM). The VDC model considered a linear dependence of the diffusivity coefficient on water content; it was a preliminary effort to quantify interfacial water transport resistances.

The VEM incorporated the effect of the membrane adjacent gas into the water transport mechanisms across the membrane bulk and boundaries. The model successfully generated values for the interfacial mass transport coefficient, k_v: 0.75 cm s^{-1} for LE, and 0.63 cm s^{-1} for VE membranes. The model calculated that interfacial mass transport phenomena are rate limiting below a membrane critical thickness of 100 μm.

Transient water transport data were coupled with the VEM. The analysis generated values for diffusivity coefficients, D, for LE membranes in the range of 10^{-10} m^2s^{-1}, which is consistent with results from NMR measurements. A dimensionless vaporization rate showed that interfacial mass transfer rates become significant with increasing temperature.

Temperature dependence for steady state water transport data agreed with Arrhenius' temperature dependence. The activation energy for LE showed E_{act}=50 kJ mol^{-1} and 44 kJ mol^{-1} for VE membranes. The possibility that the E_{act} from VE steady state water transport approximates the enthalpy of water ($\Delta H^{vap} = 36.78$ kJ/mol) was considered. The higher E_{act} for LE was explained under the basis of stronger interactions between

liquid water and the polymer, which not only alter the natural hydrophobic surface of the membrane but also induce a higher resistive water desorption process.

From transient liquid water transport, the activation energy, E_{act}, of the diffusivity coefficient showed a value of 25 $kJmol^{-1}$. This E_{act} is 50% less than the E_{act} found from the LE steady state measurements. This suggested that the larger the activity gradient, the lower the energy demand for water transport across the membrane.

The effect of the water content on the water transport properties of the proton exchange membranes was experimentally investigated through SiO_2-Nafion composite membranes. The addition of silicon dioxide into Nafion increased the water content of the membrane and decreased the membrane capacity to swell.

SiO_2 modified membranes showed no effect on the net vapour water transport compared to unmodified Nafion, but showed improved performance in the liquid water transport at high gas flow rates.

Results from vapour sorption, and water uptake measurements indicated that the membrane with 16 SiO_2 wt % marked a change in the morphology of Nafion. Scanning calorimetry measurements showed that above 16 SiO_2 wt%, the membrane water content reached a threshold and a partial volume of water switched from bound to a free condition within the bulk.

The VEM was applied to the steady state water transport data from composite/Nafion membranes at 80°C. The analysis showed no change in the water transport total resistance with the addition of SiO_2. This analysis highlighted the need to include polymer structural parameters as a function of the water content into the analysis of water transport.

It is my hope that the experimental setup, protocols and analytical tools presented here become the basis for future more ambitious research projects.

7.2 Recommendations for future work

In order to complete the study of water transport in PEMs, considerable work still remains.

Cell Design:

- A faster humidity sensor could be used to monitor the transient water transport in thin membranes. One of the challenges of the current setup is to decrease the sample area/chamber volume ratio to improve the water signal resolution in low humidity testing.
- To complete the operational conditions of a membrane within a PEM fuel cell, the incorporation of current load will allow the identification of the electro-osmotic drag and back transport fluxes in the membrane. For this, the dual chamber cell needs to be redesigned to incorporate electrical contacts on both sides of the sample with an external connection to a current load. Also, the sample holder will need to be redesigned to be able to include the gas diffusion layers and current collectors.

Experiments:

- Measurements with different chamber volumes and variation of the sensor position within the chamber are suggested to validate the assumption of good mixing in the dry chamber with laminar flow.
- Measurements at higher pressure are needed in order to eliminate the environmental humidity noise at low testing temperature and to incorporate the pressure driving force effect on water transport.
- Variations in the relative humidity inside the gas chamber are recommended to analyze the effect of surface dehydration and allow quantification of the dehydrated layer penetration.
- A clear explanation on the transient water transport signal difference for membranes dried for different time periods has to be determined. Structural analysis is required to confirm possible changes on the membrane surface occurring by exposition to the ambient air.
- VE transient measurements are to be completed. The analysis of transients with vapour water will allow the quantification of the resistance to transport across the vapour-membrane boundary.
- More steady state water transport tests for more membrane thicknesses are required in order to complete a quantitative analysis of the Vaporization Exchange Model.
- Measures for reproducibility control of the SiO_2-Nafion membrane preparation should be taken in consideration.

- The structural characterization of SiO_2 doped Nafion membranes is required to carry out the complete interpretation of the empirical results presented in this work. Surface *vs.* bulk SiO_2 distribution is recommended.
- Temperature effect analysis is required for Dynamic Vapour Sorption and Water Transport measurements on SiO_2-Nafion membranes in order to determine Activation Energy values for water uptake and water transport, respectively.

Modeling:

- To improve the analysis of transient data, a combination of the VDC model with the boundary condition of the VEM woul allow the simulation of water transport as a function of water content in the time domain.
- To be able to characterize a wider variety of PFSA membranes, the VEM requires the incorporation of polymer structural parameters, such as molecular structure, density, crystalinity, and their dependence on water content.

References

[1] J. Larminie, A. Dicks, Fuel Cell Systems Explained, Wiley, 2003.

[2] C.Y. Chow, B.M. Wozniczka, Electrochemical fuel cell stack with humidification section located upstream from the electrochemically active section, US, 20060008695, 1995.

[3] A. Cisar, A. Gonzalez-Martin, O.J. Murphy, S.F. Simpson, and C. Salinas, Internally humidified membranes for use in fuel cells, 3 (1995) 205.

[4] E. Gulzow, M. Schulze, N. Wagner, T. Kaz, R. Reissner, G. Steinhilber. Dry layer preparation and characterization of polymer electrolyte fuel cell components, J.Power Sources, 86 (2000) 352.

[5] Z. Qi, A. Kaufmann. Improvement of water management by a microporous sublayer for PEM fuel cells. J.Power Sources, 109 (2002) 38.

[6] X. Ye, C. Wang. Measurement of water transport properties through membrane electrode assemblies: Part II. Cathode diffusion media. J.Electrochem.Soc., 154 (2007) 683.

[7] L.B. Wang, N.I. Wakayama, and T. Okada. Management of water transport in the cathode of proton exchange membrane fuel cells using permanent magnet particles deposited in the cathode-side catalyst layer. ISIJ Int. 45 (2005) 1005.

[8] Z. Qi, A. Kaufman. Improvement of water management by a microporous sublayer for PEM fuel cells. J. Power Sources, 109 (2002) 38.

[9] M. Eikerling. Water management in cathode catalyst layers of PEM fuel cells. J.Electrochem.Soc., 153 (2006) 58.

[10] T. Van Nguyen, Water management by material design and engineering for PEM fuel cells, Electrochemical Soc. conference proceedings, 3, 1 (2006) 1171. Cancun, Mexico

[11] T. A. Zawodzinski, C.Derouin, S. Radzinski, R. J. Sherman, V. T. Smith, T. E. Springer. Water uptake by and transport through Nafion 117 membranes. J.Electrochem.Soc., 140 (1993) 1041.

[12] M. Eikerling, Y.I.K., A. A. Kornyshev,Yu M.Volkovich. Phenomenological theory of Electro-osmotic effect and water management in polymer electrolyte proton-conducting membranes. J.Electrochemical Society, 145 (1998) 2684.

[13] T. Okada, G. Xie, O. Gorseth, S. Kjelstrup, N. Nakamura, and T. Arimura. Ion and water transport characteristics of Nafion membranes as electrolytes. Electrochimica Acta, 43 (1998) 3741.

[14] X. Ye, C. Wang. Measurement of water transport properties through membrane-electrode assemblies: I. Membranes. J.Electrochem. Soc., 154 (2007) 676.

[15] X. Li, Principles of Fuel Cells, Taylor & Francis, NY, 2006.

[16] T.A. Zawodzinski, J. Davey, J. Valerio, and S. Gottesfeld. Water content dependence of electro-osmotic drag in proton-conducting polymer electrolytes. Electrochim.Acta, 40 (1995) 297.

[17] S. Ge, B. Yi, and P. Ming. Experimental determination of electro-osmotic drag coefficient in Nafion membrane for fuel cells. J.Electrochem.Soc., 153 (2006) 1443.

[18] Y. Hirata, S. Suizu, H.J. Sotoh, and Van Zee, John W., Electro-osmotic transport of water through Nafion-112 membrane, (2005) 2189.

[19] S. Motupally, A.J. Becker, and and J. W.Weidner. Diffusion of water in Nafion 115 membranes. J. Electrochemical Society, 147 (2000) 3171.

[20] V. Gurau, M.J. Bluemle, De Castro, Emory S., Y. Tsou, Mann Jr., J. Adin, and Zawodzinski Jr., Thomas A. Characterization of transport properties in gas diffusion layers for proton exchange membrane fuel cells. 1. Wettability (internal contact angle to water and surface energy of GDL fibers). J.Power Sources, 160 (2006) 1156.

[21] A. A. Shah, G.-. Kim, W. Gervais, A. Young, K. Promislow, J. Li. The effects of water and microstructure on the performance of polymer electrolyte fuel cells. J.Power Sources, 160 (2006) 1251.

[22] S. Ahmed, J. Kopasz, R. Kumar, and M. Krumpelt. Water balance in a polymer electrolyte fuel cell system. J. Power Sources, 112 (2002) 519.

[23] M.G. Izenson, R.W. Hill. Water balance in PEM and direct methanol fuel cells. Journal of Fuel Cell Science and Technology, 2 (2005) 1.

[24] Q. Yan, H. Toghiani, and J. Wu. Investigation of water transport through membrane in a PEM fuel cell by water balance experiments. J. Power Sources, 158 (2006) 316.

[25] O. Savadogo, Emerging membranes for electrochemical systems: Part II. High temperature composite membranes for polymer electrolyte fuel cell (PEFC) applications, 127 (2004) 135.

[26] Q. Li, R. He, J.O. Jensen, and N. J. Bjerrum. Approaches and recent development of polymer electrolyte membranes for fuel cells operating above 100 °C. Chem. Mater., 15 (2003) 4896.

[27] M. Wakizoe, O.A. Velev, and S. Srinivasan. Analysis of proton exchange membrane fuel cell performance with alternate membranes. Electrochim. Acta, 40 (1995) 335.

[28] Su, Yu-Huei. Personal Communication (unpublished results), IFCI-NRC, (2008).

[29] Zawodzinski ,T. A. Jr., Neeman M., Sillerud L.O., and Gottesfeld S. Determination of water diffusion coefficients in perfluorosulfonate ionomeric membranes. J.Phys.Chem., 95 (1991) 6040.

[30] S.J. Paddison, R. Paul, and B.S. Pivovar, The nature of proton transport in fully hydrated Nafion®; [direct methanol fuel cells], Proceedings, Int. Symposium, Electrochemical Soc., Washington, D.C.(2001) 8.

[31] A. Siu, J. Schmeisser, and S. Holdcroft. Effect of water on the low temperature conductivity of polymer electrolytes. J Phys. Chem. B, 110 (2006) 6072.

[32] H. Xu, H.R. Kunz, L. Bonville, and J.M. Fenton, Improvement of PEM fuel cell performance using low equivalent weight PFSA ionomers, 3 (2006) 361.

[33] H. Haubold, T. Vad, H. Jungbluth, and P. Hiller. Nano structure of NAFION: A SAXS study. Electrochim. Acta, 46 (2001) 1559.

[34] G. Gebel. Structural evolution of water swollen perfluorosulfonated ionomers from dry membrane to solution. Polymer, 41 (2000) 5829.

[35] S. Goswami, S. Klaus, and J. Benziger. Wetting and absorption of water drops on Nafion films. Langmuir, 24, 16 (2008) 8627.

[36] J. Zhang, S. Holdcroft, J. Zhang, Z. Xie, Y. Tang, C. Song. High temperature PEM fuel cells. J. Power Sources, 160 (2006) 872.

[37] Y. Song, H. Xu, Y. Wei, H.R. Kunz, L.J. Bonville, and J.M. Fenton. Dependence of high-temperature PEM fuel cell performance on Nafion® content. J. Power Sources, 154 (2006) 138.

[38] C. Song, Y. Tang, J.L. Zhang, J. Zhang, H. Wang, J. Shen. PEM fuel cell reaction kinetics in the temperature range of 23-120°C. Electrochim. Acta, 52 (2007) 2552.

[39] F.N.a.S. Büchi Supramaniam. Operating proton exchange membrane fuel cells without external humidification of the reactant gases. Fundamental aspects. J. Electrochem. Society, 144 (1997) 2767.

[40] A.M. Pivovar, B.S. Pivovar. Dynamic behavior of water within a polymer electrolyte fuel cell membrane at low hydration levels. J. Phys. Chem. B, 109 (2005) 785.

[41] M. Watanabe, H. Uchida, Y. Seki, M. Emori, and P. Stonehart. Self-humidifying polymer electrolyte membranes for fuel cells. J. Electrochem.Soc., 143 (1996) 3847.

[42] H. Hagihara, H. Uchida, and M. Watanabe. Preparation of highly dispersed SiO_2 and Pt particles in Nafion [registered trademark] 112 for self-humidifying electrolyte membranes in fuel cells. Electrochim. Acta, 51 (2006) 3979.

[43] L. Wang, D.M. Xing, Y.H. Liu, Y.H. Cai, Z.-. Shao, Y.F. Zhai. Pt/SiO_2 catalyst as an addition to Nafion/PTFE self-humidifying composite membrane. J.Power Sources, 161 (2006) 61.

[44] B. Smitha, S. Sridhar, and A.A. Khan. Solid polymer electrolyte membranes for fuel cell applications—a review. Journal of Membrane Science, 259 (2005) 10.

[45] M.P. Rodgers, An investigation of structure-property relationships in several categories of proton exchange membranes. Ph.D. Thesis, Simon Fraser University, Canada (2007).

[46] Y. Tominaga, I. Hong, S. Asai, and M. Sumita. Proton conduction in Nafion composite membranes filled with mesoporous silica. J. Power Sources, 171 (2007) 530.

[47] H. Tang, Z. Wan, M. Pan, and S.P. Jiang. Self-assembled Nafion-silica nanoparticles for elevated-high temperature polymer electrolyte membrane fuel cells. Electrochemistry Communications, 9 (2007) 2003.

[48] F. Pereira, K. Valle, P. Belleville, A. Morin, S. Lamberts, and C. Sanchez. Advanced mesostructured hybrid silica-nafion membranes for high-performance PEM fuel cell. Chemistry of Materials, 20 (2008) 1710.

[49] Q. Deng, R.B. Moore, and K.A. Mauritz. Nafion (R) (SiO2, ORMOSIL, and dimethylsiloxane) hybrids via in situ sol-gel reactions: Characterization of fundamental properties. J Appl Polym Sci, 68 (1998) 747.

[50] T.D. Gierke, G.E. Munn, and F.C. Wilson. Morphology in Nafion perfluorinated membrane products, as determined by wide- and small-angle X-ray studies. Journal of Polymer Science, Polymer Physics Edition, 19 (1981) 1687.

[51] G. Gebel, O. Diat. Neutron and X-ray scattering: Suitable tools for studying ionomer membranes. Fuel Cells, 5 (2005) 261.

[52] K. Schmidt-Rohr, Q. Chen. Parallel cylindrical water nanochannels in Nafion fuel-cell membranes. 7 (2008) 83.

[53] T.D. Gierke, G.E. Munn, and F.C. Wilson. Morphology in Nafion perfluorinated membrane products, as determined by wide- and small-angle x-ray studies. Journal of Polymer Science, Polymer Physics Edition, 19 (1981) 1687.

[54] H.L. Yeager, A. Steck. Cation and water diffusion in Nnafion ion exchange membranes: influence of polymer structure. J. Electrochem.Soc., 128 (1981) 1880.

[55] A.Z. Weber, and J. Newman. Transport in Polymer-Electrolyte Membranes I. Physical Model. J. Electrochem.Soc., 150 (2003) A1008.

[56] J. Hinatsu, M. Mizuhata, and H. Takenaka. Water uptake of perfluorosulfonic acid membranes from liquid water and vapor water. J. Electrocehm.Soc., 141 (1994).

[57] T.A. Zawodzinski, S. Gottesfeld Jr, S. Shoichet, and T.J. McCarthy. Contact angle between water and the surface of perfluorosulphonic acid membranes. J. Appl. Electrochem., 23 (1993) 86.

[58] P.C. Rieke, N.E. Vanderborgh. Temperature dependence of water content and proton conductivity in polyperfluorosulfonic acid membranes. Journal of Membrane Science, 32 (1987) 313.

[59] S. Gottesfeld, T.A. Zawodzinski, in R.C. Alkire, H. Gerischer, D.M. Kolb and C.W. Tobias (Ed.), Advances in Electrochemical Science and Engineering, Weinheim, Wiley-VCH, 1997, pp. 249-261.

[60] P. Futerko, I. Hsing. Thermodynamics of water vapor uptake in perfluorosulfonic acid membranes. J.Electrochem.Soc., 146 (1999) 2049.

[61] R.S. McLean, M. Doyle, and B.B. Sauer. High-resolution imaging of ionic domains and crystal morphology in ionomers using AFM techniques. Macromolecules, 33 (2000) 6541.

[62] P.W. Majsztrik, B.M. Satterfield, A.B. Bocarsly, and J.B. Benziger. Water sorption, desorption and transport in Nafion membranes. Journal of Membrane Science, 301 (2007) 93.

[63] P. Choi, R. Datta. Sorption in proton-exchange membranes. An explanation of Schroeder's Paradox. J. Electrochem.Soc., 150 (2003) 601.

[64] L.M. Onishi, J.M. Prausnitz, and J. Newman. Water-Nafion Equilibria. Absence of Schroeder's Paradox. J. Phys. Chem. B, 111 (2007) 10166.

[65] G.J.M. Janssen. A phenomenological model of water Transport in a proton exchange membrane fuel cell. J. Electrochemical Society, 148 (2001) A1313.

[66] J.N. Adam Z. Weber. Transport in Polymer-Electrolyte Membranes II. Mathematical Model. J.Electrochemical Society, 151 (2004) A311.

[67] J. Fimrite, B.Carnes, H. Struchtrup, and N.Dijilali. Transport Phenomena in Polymer Electrolyte Membranes II. Binary Friction Membrane Model. J.Electrochem.Soc., 152 (2005) A1815.

[68] T.E. Springer, T.A. Zawodzinski , and S. Gottesfeld. Polymer electrolyte fuel cell model. J. Electrochem.Soc., 138 (1991).

[69] M.W. Verbrugge, R.F. Hill. Transport Phenomena in perfluorosulfonic acid membranes during the passage of current. J. Electrochem.Soc., 137 (1990) 1131.

[70] D.M. Bernardi, M.W. Verbrugge. A mathematical model of the solid-polymer-electrolyte fuel cell. J. Electrochem.Soc., 139 (1992) 2477.

[71] M. Eikerling, Y.I. Kharkats, and A.A. Kornyshev. J. Electrochem. Soc., 145 (1998) 2684.

[72] D. Morris, X. Sun. Water-Sorption and Transport Properties of Nafion 117H. J of Applied Polymer Science, 50 (1993) 1445.

[73] C.M. Gates, J. Newman. Equilibrium and diffusion of ethanol and water in a Nafion 117 membrane. AICHE J., 46 (2000).

[74] D. Rivin, C.E. Kendrick, P.W. Gibson, and N.S. Schneider. Solubility and transport behavior of water and alcohols in Nafion™. Polymer, 42 (2001) 623.

[75] P. Krtil, A. Trojanek, and Z. Samec. Kinetics of water sorption in Nafion thin films - Quartz crystal microbalance study. J Phys Chem B, 105 (2001) 7979.

[76] P. Choi, N. Jalani H., and R. Datta. Thermodynamics and proton in Nafion I. Membrane swelling, sorption and ion-exchange equilibrium. J. Electrochemical Society, 152 (2005) E84.

[77] M.B. Satterfield, J.B. Benziger. Non-Fickian water vapor sorption dynamics by Nafion membranes. J. Phys. Chem. B, 112 (2008) 3693.

[78] S. Ge, X. Li, B. Yi, and I. Hsing. Absorption, desorption and transport of Water in Polymer Electrolyte Membranes for Fuel Cells. J. Electrochem. Soc., 152 (2005) A1149.

[79] S.C. Yeo, A. Eisenberg. Physical properties and supermolecular structure of perfluorinated ion-containing (Nafion) polymers. J Appl. Polym. Sci., 21 (1977) 875.

[80] R. Zelsmann, M.P., M. Thomas,M.Escoubes. Water self-diffusion coefficient determination in an ion exchange membrane by optical measurement. J. App. Polymer Sci., 41 (1990) 1673.

[81] T. Fuller, Solid Polymer Electrolyte Fuel Cells. Ph. D. Dissertation, (1992).

[82] T. Van Nguyen, N. Vanderborgh. Rate of isothermal hydration of polyperfluorosulfonic acid membranes. J. Membrane Sci., 143 (1998) 235.

[83] G. Suresh, A.K. Pandey, and A. Goswami. Self-diffusion coefficients of water in Nafion- 117 membrane with multivalent counterions. J. Membrane Sci., 284 (2006) 193.

[84] P. Futerko, I. Hsing. Two-dimensional finite-element method study of the resistance of membranes in polymer electrolyte fuel cells. Electrochim. Acta, 45 (2000) 1741.

[85] T. Okada, G. Xie, and M. Meeg. Simulation for water management in membranes for polymer electrolyte fuel cells. Electrochim. Acta, 43 (1998) 2141.

[86] P. Berg, K. Promislow, J.S. Pierre, J. Stumper, and B. Wetton. Water management in PEM fuel cells. J.Electrochem. Soc., 151 (2004) 341.

[87] N. Miyake, J.S. Wainright, and R.F. Savinell. Evaluation of a sol-gel derived Nafion. J. Electrochem. Soc., 148 (2001) A898.

[88] E.L. Cussler, Diffusion. Mass transfer in fluid systems, Cambridge, UK, Cambridge University Press, 1997.

[89] Vaisala Report M210566EN-C, 2005.

[90] D.R. Lide, CRC Handbook of Chemistry and Physics, (2004-2005).

[91] M. Khandelwal, M.M. Mench. Direct measurement of through-plane thermal conductivity and contact resistance in fuel cell materials. J. Power Sources, 161 (2006) 1106.

[92] E.G. Cerella, H.A. Massaldi. Water transport mechanisms through asymmetric membranes. J. Appl. Polym. Sci., 26 (1981) 1243.

[93] D.M. Bernardi, M.W. Verbrugge. Mathematical Model of a Gas Diffusion Electrode Bonded to a Polymer Electrolyte. AICHE J., 37 (1991) 1151.

[94] Y. Yang, P.N. Pintauro. Multicomponent Space-Charge Transport Model for Ion-Exchange Membranes with Variable Pore Properties. Ind. Eng. Chem. Res., 43 (2004) 2957.

[95] S.J. Paddison. Proton Conduction Mechanisms at Low Degrees of Hydration in Sulfonic Acid--Based Polymer Electrolyte Membranes. Annual Review of Materials Research, 33 (2003) 289.

[96] T. Soboleva and S. Holdcroft, Personal Communication (unpublished results), Simon Fraser University, Canada (2007).

[97] R. Huizing, M. Fowler, W. Merida, and J. Dean. Design methodology for membrane-based plate-and- frame fuel cell humidifiers. J. Power Sources, (2008, In press).

[98] C.W. Monroe, T. Romero, W. Mérida, and M. Eikerling. A vaporization-exchange model for water sorption and flux in Nafion. J. Membrane Sci., 324 (2008) 1.

[99] F.N. Buchi, G.G. Sherer. Investigation of the Transversal Water Profile in Nafion Membranes in Polymer Electrolyte Fuel cells. J.Electrochem.Soc., 148 (2001) A183.

[100] P. Cave, Membrane Moisture Transfer in Fuel Cell Humidifiers. Masters Thesis, University of British Columbia, (2007).

[101] M. Courel, M. Dornier, G.M. Rios, and M. Reynes. Modelling of water transport in osmotic distillation using asymmetric membrane. J.Membrane Sci., 173 (2000) 107.

[102] J. Metz, W. J. C. van de Ven, J. Potreck, M. H. V. Mulder, and M.Wessling. Transport of water vapor and inert gas mixtures through highly selective and highly permeable polymer membranes. J. Membrane Sci., 251 (2005) 29.

[103] C. Yang, S. Srinivasan, A.B. Bocarsly, S. Tulyani, and J.B. Benziger. A comparison of physical properties and fuel cell performance of Nafion and zirconium phosphate/Nafion composite membranes. J. Membr. Sci., 237 (2004) 145.

[104] K.A. Mauritz, R.M. Warren. Microstructural Evolution of a Silicon-Oxide phase in a perfluorosulfonic acid ionomer by an in situ sol-gel reaction .1. Infrared spectroscopic studies. Macromolecules, 22 (1989) 1730.

[105] N.H. Jalani, R. Datta. The effect of equivalent weight, temperature, cationic forms, sorbates, and nanoinorganic additives on the sorption behavior of Nafion [registered trademark]. J.Membr.Sci., 264 (2005) 167.

[106] F. Volino, M. Pineri, A.J. Dianoux, and A. De Geyer. Water mobility in a water-soaked Nafion membrane: a high-resolution neutron quasielastic study. J. Polymer Sci., Polymer Physics Edition, 20 (1982) 481.

[107] P.J. Flatau, R.L. Walko, and W.R. Cotton. Polynomial fits to saturation vapor pressure. J. Appl.Meteorol., 31 (1992) 1507.

[108] P. Scharfer, W. Schabel, and M. Kind. Mass transport measurements in membranes by means of in situ Raman spectroscopy-first results of methanol and water profiles in fuel cell membranes. J. Membrane Sci., 303 (2007) 37.

[109] G. Ye, N. Janzen, and G.R. Goward. Solid-state NMR study of two classic proton conducting polymers: Nafion and sulfonated poly(ether ether ketone)s. Macromolecules, 39 (2006) 3283.

[110] Z. Ziheng, M. Jonathan, W. Jinfeng, W. Haijang, P. Keith, B. Bruce. Magnetic resonance imaging of water content across the Nafion membrane in an operational PEM fuel cell. Resonance, 193, 2, (2008), 259.

[111] J. Bedet, G. Maranzana, S. Leclerc, O. Lottin, C. Moyne, D. Stemmelen, D., P. Mutzenhardt, D. Canet. Magnetic resonance imaging of water distribution and production in a 6 cm^2 PEMFC under operation. Int. J. Hydrogen Energy, 33, 12, (2008), 3146.

Appendices

Appendix A. Analysis of Fluxes in Dry Chamber of Permeability Cell

The experimental cell is divided in two main chambers: the dry and the wet chamber. Inside the dry chamber, dew point measurements are taken, and inlet and outlet gases are fed. The control volume of the cell's dry chamber is shown in Figure A.1.

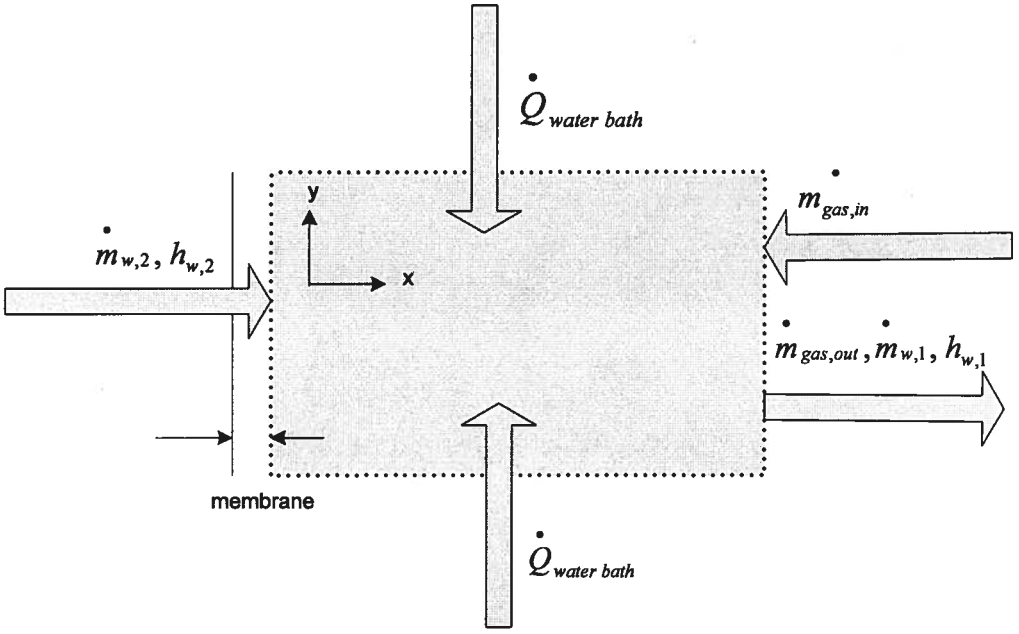

Figure A.1: Control volume in the dry chamber of the permeability cell

Based on a mass balance, the exhaust flux in the control volume is composed by the gas flux and the water flux across the membrane:

$$\dot{m}_{T,out} = \dot{m}_{gas,out} + \dot{m}_{w,2} \qquad \textbf{(A.1)}$$

where,

$$\dot{m}_{w,1} = \dot{m}_{w,2} \tag{A.2}$$

and

$$\dot{m}_{w,2} = \frac{X_{w,2}}{1 - X_{w,2}} \dot{m}_{gas} \tag{A.3}$$

where

$$X_{w,2} = \frac{P_{w,2}}{P_{Total}} \tag{A.4}$$

assuming $P_{total} = P_{atm}$, the flux of water across the membrane is calculated according to:

$$J = \frac{m_{w,2}}{A} = \left[\frac{mol}{s \cdot m^2}\right] \tag{A.5}$$

Gas Flow Regime

The Reynolds number was calculated based on the cell dimensions, helium density and dynamic viscosity at 25°C using the gas flow rate used in the dry chamber: 30 to 1000 cm^3/min (STP):

Table A. 2. Reynolds Number for the gas flow rate calculated for the dry cell configuration

Cell component	Diameter, ϕ x 10^{-3} m	$\mathrm{Re} = \frac{\rho v \phi}{\mu}$	
		30 cm^3 min^{-1}	1000 $cm^3 min^{-1}$
Inlet Tubing	3.17	1.8	60
Exposed Membrane	15.95	0.36	12

The results from Table A.2 suggest a low Reynolds number along the gas flow rate range applied during experiments. Thus, it was considered that neglecting forced convective effects of the sweeping on the dry membrane surface was a good approximation. Similarly, the boundary layer resistance was neglected due to the fast mixing of the gas creating a non-parallel flow with respect to the membrane surface.

Appendix B. Technical drawings. Design of the permeability cell

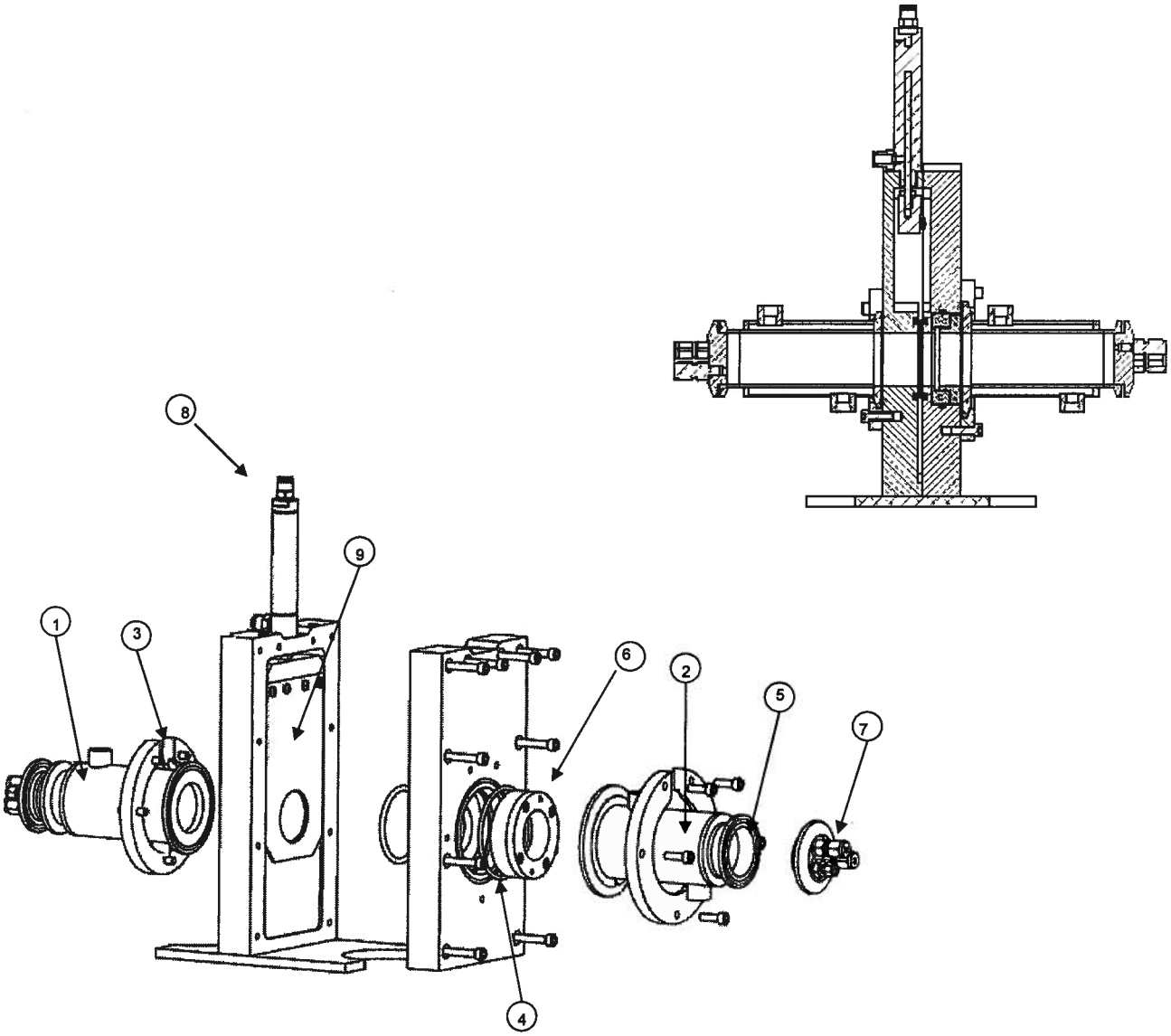

Qty.	Description	Material	# Drawing
2	Chamber	S.S.	1,2
2	External sealing flange	S.S.	3
2	O-Ring	FPR encap.silicon	4
2	Gasket	Silicon	5
1	Sample Holder	Polycarbonate	6
2	Gas, Water and Sensors manifold	S.S	7
1	Gated Valve Piston	S.S.	8
9	Gated Valve	Polycarbonate	9

This figure has been removed due to Copyright reasons. The drawing shows the cell gate subassembly.

This figure has been removed due to Copyright reasons. The drawing shows the sample chamber-sample side.

This figure has been removed due to Copyright reasons. The drawing shows the gate valve cover.

This figure has been removed due to Copyright reasons. The drawing shows the cell's gate.

This figure has been removed due to Copyright reasons. The drawing shows the gate valve-gate carrier.

This figure has been removed due to Copyright reasons. The drawing shows the gated cell-stand.

This figure has been removed due to Copyright reasons. The drawing shows the sample carrier-1.

This figure has been removed due to Copyright reasons. The drawing shows the sample carrier subassembly.

This figure has been removed due to Copyright reasons. The drawing shows ported end cap.

This figure has been removed due to Copyright reasons. The drawing shows the retaining ring.

Appendix C. Dew Point Temperature sensor: cross-reference with Mass Spectrometer

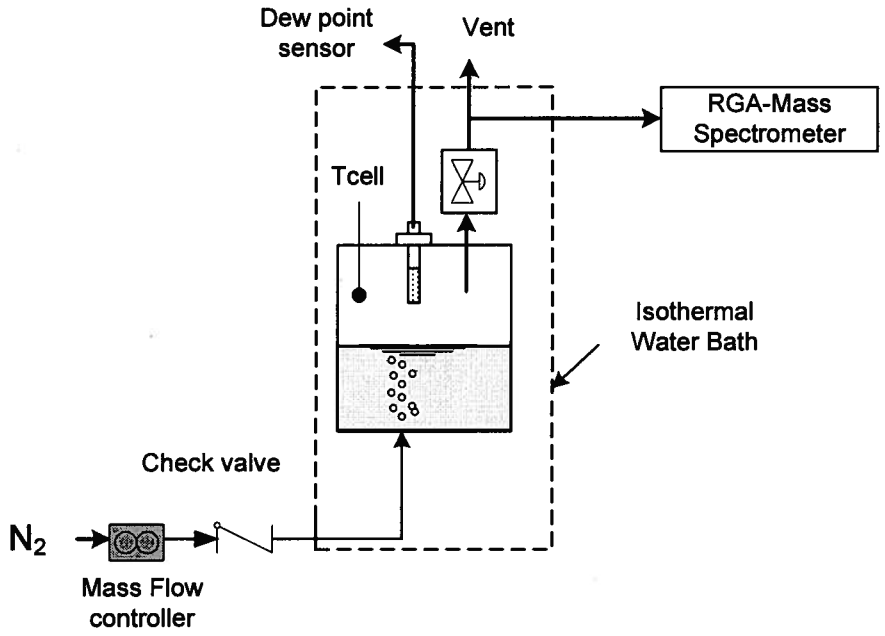

Figure C1: Setup for dew point temperature sensor cross-reference. A saturated atmosphere was kept during measurements.

Results from both techniques are shown in Table C.1, and compared with theoretical saturation pressure calculated from Hyland and Wexler expression [107] at each saturation temperature.

Table C.1. Vapour Pressure (mbar) data. Results from cross-reference analysis: dew point temperature (Vaisala™), RGA-MS(Hiden™), and Hyland and Wexler Equation.

Techniques	30 °C	40 °C	50 °C	60 °C	70 °C	80 °C
	Pw (mbar)					
Hyland & Wexler Equation (Our Reference)	**0.042**	**0.073**	**0.122**	**0.198**	**0.310**	**0.471**
RGA-Mass Spectrometer (Hiden™)	0.044	0.073	0.124	0.198	0.331	0.485
Dew Point T. Sensor (Vaisala™)	0.043	0.075	0.124	0.202	0.313	0.464

The dew point temperature sensor (Vaisala™) showed smaller error (max. 2.7%) than the Mass Spectrometer (max. 6.7%) with respect to the reference in the whole temperature testing. The Mass Spectrometer showed larger deviation from the reference at temperatures $\geq 60^{o}C$, while the dew point temperature sensor showed less variability in the whole temperature range.

Appendix D. Effective Diffusivity from steady state coefficients

Most of the reported analyses for Nafion membranes are based on an effective diffusion coefficient, which embodies the lack of information on the microscopic topology. This coefficient is a function of the chemical species, their environment, and the local geometry. Most of the reported work simplifies the analysis by considering only its dependence on water content, and by incorporating material properties like the density of dry Nafion, ρ_d, and the equivalent weight. With these simplifications, the molar flux of water in a membrane can be calculated according to first Fick's law of diffusion:

$$J = -D(\lambda)\nabla c_{H_2O} \tag{D.1}$$

Following expressions based on first Fick's law, Motupally et al. derived diffusion coefficients for Nafion membranes by assuming one dimensional Fickian transport at steady state [19]:

$$D(\lambda) = -J\frac{EW(1+\gamma)}{\rho_d\left(\frac{\partial\lambda}{\partial x}\right)} \tag{D.2}$$

We assumed a linear water concentration as illustrated in Figure 4.5 with possible discontinuities across the interfaces. Although similar diagrams have been used to describe water transport in Nafion [62], we emphasize that the exact variation of water activity or concentration across the membrane is not known.

In general, the variation of water content with distance across the membrane (i.e., the exact form of $\lambda(x)$ in the range $0 < x < L$ is unknown. Considering the very simplified case of a linear profile:

$$\left(\frac{\partial \lambda}{\partial x}\right) = \left(\frac{\left(\lambda(L+\Delta L) - \lambda(0)\right)}{L+\Delta L}\right) = C_{\lambda} \qquad \textbf{(D.3)}$$

C_{λ} is constant, and ΔL is the change in membrane thickness upon hydration (at steady state). We calculated the approximate values for $\lambda(0)$ and $\lambda(L+\Delta L)$ based on our experimental values for vapour pressure, the measured membrane thickness, and the empirical absorption isotherms.

The membrane surface water content, ($\lambda(0)$), was calculated from isothermal data and the linear profiles supported by the works of Scharfer and Ge et al. [78,108]. We used the empirical absorption isotherms (Figure D.1) reported by Zawodsinski [11], and Hinatsu [56], and recent data from Soboleva and Holdcroft (for Nafion 115)[96], to calculate the values of water content on the membrane surface ($\lambda(L)$)based on our calculated activity values generated by the gas flow rate.

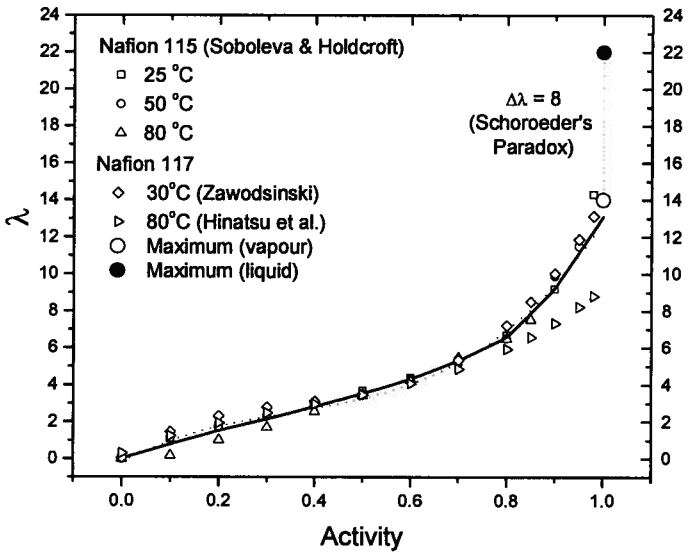

Figure D.1. Membrane water content *vs.* water activity for Nafion 115 and Nafion 117 at different temperatures, from different sources

We used the conventional definition of water activity to describe the relative humidity in the gas phase next to the membrane surface. From the isotherm in Figure D.1, for each water activity on the dry surface, the water content, $\lambda(L+\Delta L)$, was calculated from correlating our experimental vapour pressure data with the isothermal sorption data. The measured change in membrane thickness, $(L+\Delta L)$, for the liquid-gas and vapor-gas equilibrated membranes in our experimental series was approximately 30% and 21% of the original membrane thickness, respectively. The water content at the wet surface, $\lambda(0)$, was given a value of 22 and 14 $molH_2O/molSO_3^-$ for liquid and vapour equilibration, respectively.

The effective diffusivity coefficient for Nafion 115 was calculated under the assumptions of one-dimensional transport are included in Table D.1, for 30, 50 and 70°C, with helium flow rate maintained at 100 cm^3/min (STP) in all cases.

Table D.1. Effective diffusivities for water in Nafion 115 membrane equilibrated with liquid-gas and vapour-gas at different temperatures

$D_{effective}$		
Temperature	**Vapour**	**Liquid**
°C	**x 10^{10} m^2 s^{-1}**	
30	**0.25**	**0.26**
40	**0.56**	**0.47**
50	**0.79**	**0.85**
60	**1.25**	**1.50**
70	**2.21**	**2.83**
80	**3.55**	**4.30**
$E_{activation}$ (kJmol^{-1})	**45**	**51**

The increasing diffusivity with the temperature rise compared well with published data [78,81]. The activation energy calculated from liquid diffusivity showed 51 kJmol^{-1}; followed closely by 45 kJmol^{-1}, from vapour diffusivity.

The diffusivity showed low dependency on the water phase (liquid or vapour) in contact with the membrane. We emphasize that the transition from the experimental measurements to the calculated diffusivities depends on several assumptions whose validity can be questioned. Assuming a linear concentration profile within the membrane is the first weakness in this type of analysis. Different methodologies and assumptions in this process amongst different authors contribute to the variability in reported diffusion coefficients.

Figure D.2 is a representation of the diffusivity coefficient dependency on the activity gradient acting as the driving force. The maximum and decay of D_{eff} shows the limited effect of the driving force when it is overcome by interfacial resistance. This

evidences the need of more information on the kinetics of the interfacial phenomena in order to decouple bulk from surface transport.

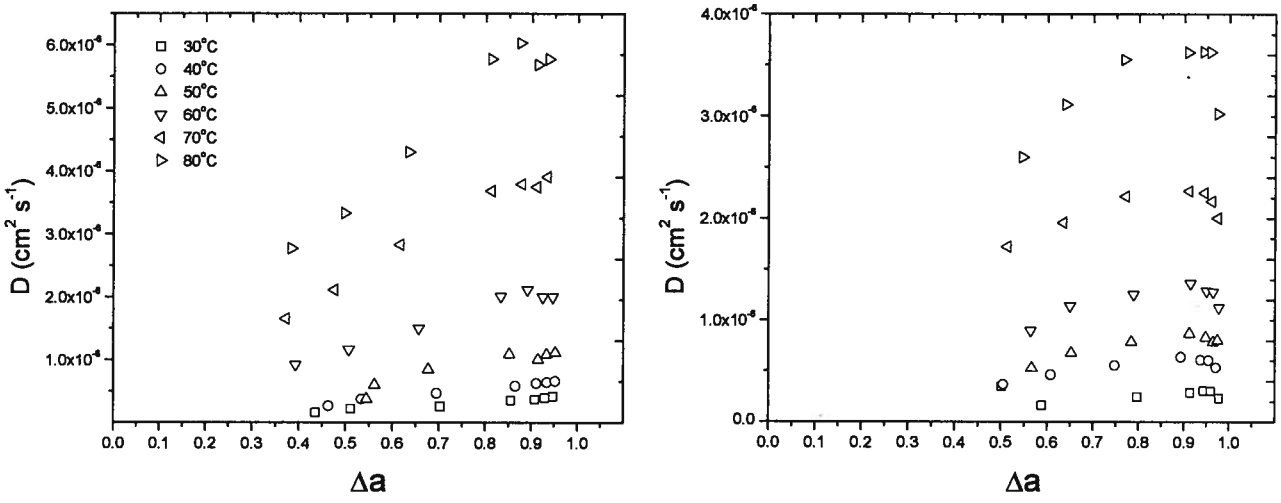

Figure D.2 The effective water diffusivity for LE (left) and vapor-gas equilibrated membranes (right) from permeation measurements.

Appendix E. Varying Coefficient Diffusion Model

Using the form proposed in [109], the following relationships at the boundary are assumed:

$$J = -QD(\lambda)\frac{d\lambda}{dx}\bigg|_{x=L} = Q\,k_d\left(\lambda|_{x=L} - \lambda_2^e\right) \tag{E1}$$

where Q is the concentration of sulfonate sites in the membrane and k_d is the desorption coefficient. Given an initial water content profile $\lambda(x,0)$ and inlet flow parameters that determine λ_1^e and λ_2^e, and $J(t)$ can be predicted numerically. By comparing the transient model prediction to experimental data, estimates of δ and k_d can be determined.

We consider briefly the case of constant diffusivity, D, at the beginning of this paragraph for illustrative purposes. At steady state, the following result comes from the model after a straightforward calculation:

$$J = QF\left(\lambda_1^e - \lambda_2^e\right) \tag{E2}$$

where F defines the resistance in series neglecting k_a:

$$F = \frac{1}{1/\gamma_d + L/D} \tag{E3}$$

With a fully hydrated membrane surface we assumed fast sorption rates and resistance across this surface is neglected.

From the steady state computations, the relative size of D and k_d cannot be determined. The parameter k_d has a minimum possible value:

$$k_{d\min} = \frac{J_s}{Q\left(\lambda_1 - \lambda_2^e\right)} \tag{E4}$$

The values of D and k_d that lead to a given steady state flux J_s can be written in terms of a basis parameter θ in (0,1). Two equations can be established:

$$k_d = \frac{k_{d\min}}{\theta} \tag{E5}$$

$$D = \frac{Lk_{d\min}}{1-\theta} \tag{E6}$$

This basis parameter is nothing more than a modified form of the Biot dimensionless number for mass transfer, relating the ratio of diffusion resistance to convection resistance. For our case of interest, where D is not constant but has a linear

dependency on water content with parameter δ, the same general procedure can be used. However, the analogue of Eqn. (E6) is mathematically more complex.

At steady state,

$$J_s = -Q\delta\lambda(x)\frac{d\lambda(x)}{dx} \tag{E7}$$

Rearranging this equation gives,

$$2\lambda\frac{d\lambda}{dx} = -\frac{2J_s}{Q\delta} \tag{E8}$$

Noting that $2\lambda\frac{d\lambda}{dx} = \frac{d(\lambda^2)}{dx}$ and that $J_s = Qk_d(\lambda_2 - \lambda_2^e)$,

$$\frac{d(\lambda^2)}{dx} = -\frac{2}{\delta}k_d(\lambda_2 - \lambda_2^e) \tag{E9}$$

Integrating both sides with respect to x from 0 to L, with boundary conditions $\lambda(0)=\lambda_{liq}$ and $\lambda(L)=\lambda_2$,

$$\lambda_{liq}^2 - \lambda_2^2 = 2B(\lambda_2 - \lambda_2^e) \tag{E10}$$

Where by definition

$$B = \frac{Lk_d}{\delta} \tag{E11}$$

Rewrite Eqn.(E10),

$$\lambda_2^2 + 2B\lambda_2 - (\lambda_{liq}^2 + 2B\lambda_2^e) = 0 \tag{E12}$$

And finding the positive root,

$$\lambda_2 = -B + \sqrt{B^2 + (\lambda_{liq}^2 + 2B\lambda_2^e)} \tag{E13}$$

Then

$$J_{ss} = a\gamma_d\left(B + \sqrt{B^2 + (\lambda_{liq}^2 + 2B\lambda_2^e)} - \lambda_2^e\right) \tag{E14}$$

Now with k_d given via Equation (E3) and J_{ss} known from the experimental data, Equation (E14) becomes an implicit equation for B, which was solved with a root finding technique. With B and k_d known, δ can be found from the definition of B (Equation (E11)).

Appendix F. Dimensionless solution to the governing equation system of the Vaporization-Exchange Model.

The following dimensionless variables were defined:

$$\xi = \frac{Z}{L}, \qquad \tau = \frac{Dt}{L^2}, \qquad \theta_m(\tau,\xi) = \frac{c - c_0}{c_{\max}^{liq} - c_0}, \quad \text{and} \quad \theta_v(\tau) = \frac{p_{out} - p_{in}}{p_{sat} - p_{in}}, \tag{F.1}$$

where ξ represents position in the membrane, τ time, θ_m water concentration in the membrane, and θ_v vapour pressure of water in the dry chamber. If the inlet gas is dry, then $p_{in} = 0$. Thus, θ_v becomes the relative humidity of the outlet gas, RH.

The ratio of interface to bulk rate processes is defined by the parameter α, which can be described as equivalent to a Biot number:

$$\alpha = \frac{Lk_v p_{sat}(a - RH_{in})}{D(c_{\max} - c_0)RT}, \tag{F.2}$$

where $RH_{in}=p_{in}/p_{sat}$ defines relative humidity in the inlet stream, and c_0 stands for the initial water concentration in the membrane. Instead of expressing the typical convection by the flowing gas, as a Biot or Sherwood number would, α represents the scale of diffusional resistance over the scale of the kinetic resistance to vaporization exchange: α is small when vaporization exchange limits the flux and large when mass transfer through the membrane is rate limiting.

Three dimensionless parameters may be controlled experimentally:

$$\psi = \frac{c_0 p_{sat} - c_{\max}^{liq} p_{in}}{c_{\max}^{liq}(p_{sat} - p_{in})} = \frac{(c_0 / c_{\max}^{liq}) - RH_{in}}{1 - RH_{in}}, \quad \gamma = \frac{k_v A L^2}{DV}, \text{ and } \phi = \frac{L^2 \dot{V}}{DV} \tag{F.3}$$

The governing equations become

$$\frac{d\theta_v}{d\tau} = -\phi\theta_v - \frac{\gamma}{\alpha}\frac{\partial\theta_m}{\partial\xi}\bigg|_{\tau,1} \qquad \text{and} \qquad \frac{\partial\theta_m}{\partial\tau} = \frac{\partial^2\theta_m}{\partial\xi^2}, \tag{F.4}$$

the initial conditions simplify to

$$\theta_v(0) = 0 \qquad \text{and} \qquad \theta_m(0,\xi) = 0, \tag{F.5}$$

And the boundary conditions on the membrane are

$$\theta_m(\tau,0) = 1 \quad \text{and} \quad \frac{\partial\theta_m}{\partial\xi}\bigg|_{\tau,\,1} = \alpha[\theta_v(\tau) - \theta_m(\tau,1) + \psi(1-\theta_m(\tau,1))]. \tag{F.6}$$

Steady State Response.- The governing system is solved by the method of Laplace transformation with respect to time. This employs the initial conditions immediately, reduces gas continuity to an algebraic relation, and simplifies water continuity in the membrane to an ordinary differential equation (ODE) in ξ. The ODE can be solved directly, after which one can isolate the dependent variables. In terms of the Laplace variable s,

$$\mathcal{L}\{\theta_v(\tau)\} = \bar{\theta}_v = \frac{\gamma\left[(1-\psi)+\psi\cosh\left(\sqrt{s}\right)\right]}{s\left[(\phi+\gamma+s)\cosh\left(\sqrt{s}\right)+\alpha(1-\psi)(\phi+s)\sinh\left(\sqrt{s}/\sqrt{s}\right)\right]} \tag{F.7}$$

The steady state vapour pressure,

$$\theta_v^{\infty} = \lim_{\tau\to\infty}\theta_v(\tau) = \lim_{s\to 0} s\bar{\theta}_v = \frac{\gamma}{\gamma+\phi[1+\alpha(1-\psi)]} \tag{F.8}$$

Upon a return to the original, dimensional experimental parameters, this rearranges to:

$$\frac{1-\theta_v^{\infty}}{\theta_v^{\infty}} = \left(\frac{1}{k_v} + \frac{Lp_{sat}}{RTDc_{\max}}\right)\frac{\dot{V}}{A} = m \cdot \frac{\dot{V}}{A} \qquad \textbf{(F.9)}$$

Transient Response.- Solving Equation (F.7) for s=0, $\bar{\theta}_v$ was converted in a sum of two terms and the denominator was replaced by their second-order Maclaurin series, inversion yields

$$\lim_{\tau>>1} \frac{\theta_v(\tau)}{\theta_v^{\infty}} = 1-(1-\psi)e^{-k_1\tau} - \psi e^{-k_2\tau} \quad , \qquad \textbf{(F.10)}$$

with constants

$$k_1 = \left[\frac{1}{6} + \frac{1}{3}\left(1 + \frac{\dot{V}}{k_v A}\right)\theta_v^{\infty} + \frac{DV}{L^2\dot{V}}\left(1-\theta_v^{\infty}\right)\right]^{-1} \quad \text{and} \quad k_2 = (k_1 - 2)^{-1} \qquad \textbf{(F.11)}$$

An expansion of Equation (F.7) for large s yields an expression valid for small τ. By inversion, the following equation is derived

$$\lim_{\tau<<1} \theta(\tau) = \gamma\left[(1+2\tau)\ erfc\left(\frac{1}{\sqrt{4\tau}}\right) - \sqrt{\frac{4\tau}{\pi}}\exp\left(-\frac{1}{4\tau}\right)\right] + \gamma\psi\tau \qquad \textbf{(F.12)}$$

Appendix G. Collaborative work terms

Many challenges needed to be overcome to ensure the success of this project. The main challenges were a lack of lab facilities, testing instruments, and project setup. Once these constraints were overcome, however, the design of the testing rig, its corresponding thermodynamic analysis, as well as control and instrumentation proceeded successfully.

I carried these out under the supervision of Professor Walter Mérida. Furthermore, I am also the primary contributor to the experimental protocols, measurements, data analysis and results interpretation presented in this thesis. A version of Sections 4.1 and 4.2 will be submitted for publication. Romero, T. and Mérida, W. "Liquid and vapour water transport in Nafion membranes".

The significant results this thesis produced could not have been achieved without the collaborative efforts of the following people. Professor Bryan Wetton[3] generated an analytical solution (Section 5.1) to my proposed resistance in series water transport configuration. Professor Michael Eikerling[4,5] and Dr. Charles Monroe[2] proposed the vaporization-exchange model (included in Section 5.2) to fit my experimental data. The application of this model combined with my data analysis resulted in acceptance for journal publication. Monroe, Ch. ; Romero, T.; Mérida, W. and Eikerling, M. (2008) A vaporization-exchange model for water sorption and flux in Nafion, Journal of Membrane Science, 324 (2008) 1.

Professor Steve Holcroft[2,3] and the Membrane Electrode Assembly (MEA) team[3] provided equipment, training, and membrane samples which I used for analysis of

---

[3] Department of Mathematics, University of British Columbia, Vancouver, Canada, V6T 1Z4
[4] Department of Chemistry, Simon Fraser University, Vancouver, Canada, V5A 1S6
[5] National Research Council (NRC) - Institute for Fuel Cell Innovation (IFCI), Vancouver, Canada, V6T 1W5

composite membranes. Chapter 6 includes the results of this analysis. On these terms, the following journal publication is in preparation: Romero, T.; Adachi, M.; Titichai, N., Mérida, W., and Hodlcroft, S. The nature of water transport in composite SiO_2- Nafion membranes.